

PREDICTING BLENDING EFFICIENCY USING ONLY KEY FLOW PROPERTIES-THE
NEXT STEP IN BLENDER DESIGN

By

MILORAD DJOMLIJA

A DISSERTATION PRESENTED TO THE GRADUATE SCHOOL
OF THE UNIVERSITY OF FLORIDA IN PARTIAL FULFILLMENT
OF THE REQUIREMENTS FOR THE DEGREE OF
DOCTOR OF PHILOSOPHY

UNIVERSITY OF FLORIDA

2009

© 2009 Milorad Djomlija

To My Mother

ACKNOWLEDGEMENTS

I would like to thank all the members of my committee for their support and encouragement. I especially would like to thank Dr. Kerry Johanson for his input over the years and to all my friends and family for their moral support.

TABLE OF CONTENTS

	<u>page</u>
ACKNOWLEDGEMENTS	4
LIST OF TABLES.....	6
LIST OF FIGURES	7
NOMENCLATURE	10
ABSTRACT	13
CHAPTER	
1 INTRODUCTION.....	14
2 MODEL DEVELOPMENT FOR ROTARY SHELL BLENDERS.....	31
Determination of Plastic Region for Parabolic Model.....	32
Velocity Within Plastic Region for Parabolic Model	34
Determination of Plastic Region Method of Characteristics	39
Velocity Within Plastic Region for Method of Characteristic Model	54
Slope Stability	65
Placement of Tracers.....	67
Transfer Function for a Single Blending Increment	70
3 EXPERIMENTAL	75
Experimental Procedure.....	75
Analyzing Procedure.....	77
Schulze Measurements.....	80
Results.....	82
4 MODEL VALIDATION	86
Placement of Markers on Top Surface.....	90
Placement of Markers via Scanning.....	92
Placement of Markers in Single Vertical Strip.....	98
5 CONCLUSION	110
LIST OF REFERENCES	117
BIOGRAPHICAL SKETCH	120

LIST OF TABLES

<u>Table</u>		<u>page</u>
1-1	Velocity within plastic region as a function of depth at various k_1 values	35
3-1	Cohesion & Unconfined Yield Strength for Mixtures used in Experiments.....	82
4-1	Reference Points & Coordinate Transformation Equation From x' to x_c	95
4-2	Reference Points & Coordinate Transformation Equation From y' to y_c	95

LIST OF FIGURES

<u>Figure</u>	<u>page</u>
2-1 Schematic view of flow geometry with corresponding coordinate system	32
2-2 Series of Mohr circle for a particular consolidation stress	33
2-3 Height of material used for determining consolidation load	34
2-4 Velocity profile within plastic region	36
2-5 Velocity along free surface vs. thickness of plastic region	37
2-6 Scaling factor for particles at tips of avalanche	38
2-7 Stresses acting on a unit of volume in Cartesian coordinate	42
2-8 Stresses acting on a unit volume in principal coordinate.....	42
2-9 Mohr circle diagram.....	43
2-10 Yield locus	45
2-11 Characteristic direction	46
2.12 Characteristic lines	48
2-13 Active and passive Mohr circle	50
2-14 Wall angles	52
2-15 Wall angles	53
2-16 Wall angles	54
2-17 Non-associative Case	56
2-18 Associative case	57
2-19 Characteristic direction for velocity.....	59
2-20 Stress and velocity mesh.....	61
2-21 Ordinary method of slices.....	66
2-22 Horizontal placement of markers	68
2-23 Vertical tracer placement.....	69

2.24	Continuous blender schematic.....	70
2-25	Unit impulse	72
2-26	Recycle.....	72
2-27	Recycle peaks	73
2-28	Finish line placement	73
3-1	Placement of markers.....	76
3-2	Threshold peaks of black & white particles	78
3-3	Analyzing window	79
3-4	Cross-sectional schematic of the Schulze shear cell.....	80
3-5	Yield locus.....	81
3-6	Concentration peaks of markers.....	83
3-7	Variance of markers	84
4-1	Schematic of concentration peaks.....	87
4-2	Horizontal placement of markers.....	91
4-3	Image from camcorder immediately following initial sluff of material	93
4-4	Mapping of markers.....	94
4-5	Imported scanner markers.....	97
4-6	Variance of simulations of the parabolic model vs. experimental variance	98
4-7	Vertical placement of tracers.....	99
4-8	Concentration peaks of markers for parabolic model	101
4-9	Thickness of avalanches from simulations of parabolic model	102
4-10	Variance of simulations of the parabolic model at various cohesion values.....	102
4-11	Variance of simulations of the parabolic model vs. experimental variance	105
4-12	Concentration peaks of markers for method of characteristic model	107
4-13	Thickness of avalanches from simulations of moc model.....	107

4-14	Variance of simulations of the moc model vs. experimental variance	108
4-15	Variance of simulations of the moc model at various cohesion values	109

NOMENCLATURE

$F(t)$	Fraction of tracers in outflow which has been in system for a time less than t
$E(t)$	Distribution function for residence time
VRR	Variance reduction ratio
an	Half the length of the free surface
σ^*	Mean stress
fc	Unconfined yield strength
c	Cohesion
ϕ	Angle of internal friction
ε	Angle measured from x-axis to inclined free surface
γ	Material weight density
δ	Thickness of plastic region
δ_o	Thickness of plastic zone at center
σ_1	Consolidation stress
ρ	Bulk density
h	Height of bed
F	Ratio of material strength to applied forces for individual slices used in ordinary method of slices
Δl	Length of base of slices used in ordinary method of slices
α_1	Angle base of slices used in ordinary method of slices make with horizontal
W	Weight of slice used in ordinary method of slices
s	Available shear strength of material used in ordinary method of slices
τ	Equilibrium shear stress used in ordinary method of slices

σ	Normal stress on shear plane
LOD	Length of drum
ω	Angular velocity
$a(\delta)$	Velocity along the free surface
h_1	Distance from the center of the drum to the center of the free surface.
σ_{xx}	Normal stress along x-plane
σ_{yy}	Normal stress along y-plane
τ_{yx}	Shear stress in x-direction along y-plane
μ	Coefficient of friction
σ_1	Major principle stress
σ_3	Minor principal stress
$\dot{\epsilon}_1$	Major principle strain rate
$\dot{\epsilon}_3$	Minor principle strain rate
ζ	Angle measured from x-axis to characteristics
ψ	Angle measured counter clockwise from the x-axis to the major principle stress direction
θ	Angle measured counter clockwise from the x-axis to the major principle strain rate direction
τ_w	Shear stress along wall
μ_w	Coefficient of wall friction
σ_w	Normal stress along wall
c_w	Adhesion
ϕ_{wall}	Angle of wall friction

Θ	Angle x-axis makes with boundary
$\dot{\gamma}$	Strain rate
$\dot{\epsilon}$	Normal strain rate
r	Radius of drum
β_0	Angle the center of drum makes with corner of the material
Y	Yield surface
R	Radius of stress Mohr's circle
R'	Radius of strain rate Mohr's circle
e^*	Mean strain rate

Abstract of Dissertation Presented to the Graduate School
of the University of Florida in Partial Fulfillment of the
Requirements for the Degree of Doctor of Philosophy

ANALYSIS OF CRITICAL STATE OF MATERIAL IN A UNCONFINED SLOPE WHEN
ANGLE OF INCLINATION IS LARGER THEN THE INTERNAL ANGLE OF FRICTION

By

Milorad Djomlija

December 2009

Chair: Kerry Johanson
Co-chair: Anuj Chauhan
Major: Chemical Engineering

Blending is a fundamental and crucial process used in industry. Despite the numerous years spent studying blending it is still a poorly understood phenomenon. The difficulty arises due to the fact that blending is a convoluted process involving material properties, blender geometry and operational parameters. We devised a method of uncoupling them from one another to see the impact that material properties has on the blending process. Two continuous models are proposed that predicts blending for a rotary shell blender for a mixture consisting of components of the same physical properties. The first model assumes a parabolic shape for the plastic region where the thickness at the center is based on material properties and assumes the velocity profile within the plastic region is an exponential one. The second model utilizes the method of characteristics to determine the morphology and velocity profile of the plastic region based on material properties. Simulations were performed at various cohesion values to ascertain its effect on blending. The simulations were compared with experiments where a binary mixture of sand of the same physical properties was blended in a rotary shell blender at various cohesion values.

CHAPTER 1 INTRODUCTION

Mixing is an indispensable unit operation in many industries such as pharmaceuticals, food, and agriculture. The quality and price of products are often dependent on the efficiency of the mixing process. Mixing is often a precursor for other process stages, therefore affecting the efficiency not only of itself, but of a whole series of processes further down the line. Currently, assessing a blender's efficiency is accomplished by extracting a sample, often by means which are detrimental to the mixture, and measuring its uniformity. This is done for a specific blender operating at a prescribed speed and with a specific mixture. Blending is a convoluted process involving blender geometry, operational parameters and material flow properties. In order to advance the science surrounding blending it is necessary to separate or de-convolute the effect of these three effects. Currently, changing either the blender, the operational speed, or the mixture requires a new evaluation of blending quality. These experimental blending evaluations are time consuming and arduous tasks. The inability to separate a blender's geometry and operational parameters responsible for blending from those of the material parameters makes scaling up to pilot scale studies virtually impossible. For industries such as pharmaceuticals where a small batch of only a few kg costs several million dollars, it becomes cost prohibitive to optimize blending operations using pilot scale studies.

Random sampling of individual mixtures is an accurate and reliable method of ascertaining the quality of a mix. However, it does have its drawn backs.

- Invasive tools, such as a sample thief, are harmful to the blending process and often promote localized segregation, thereby varying and biasing the measurements
- Frequent sampling requires the blending procedure to be shut down to probe the mixture, a time consuming and laborious task resulting in costly downtime.
- Often thousands of samples are required to quantify, with good statistical accuracy, the blending in a particular blender.

The advent of inline optical measurement methods are helping to reduce these sampling frequencies. Ideally we would like to skip the manual blending evaluation step altogether and predict blender performance by measuring particle scale properties and using these properties to model particular blender geometries and predict blending efficiencies for any operational parameters. This methodology allows one to change blender operation based on changes in flow properties. Currently such ability does not exist. Extensive manual pilot scale blender tests must be performed to quantify blender performance under all operational and raw material changes. Material properties, blender geometry and operational parameters all influence blending. To fully break away from invasive sampling techniques, the influence of each must be uncoupled from the others. One must be able to predict the velocities through blending equipment and relate these velocities to easily measured material flow properties and operational parameters. These velocities can then be used to compute the residence time distributions and, finally, the blender performance. This methodology will set a framework that will allow predictive blender models based on sound scientific principles not statistical studies of past blender performance with old materials.

Variation in material properties such as cohesion, particle size distribution and internal angle of friction affect the flow property of a mixture, therefore changing the velocity profile within the blender. Understanding the influence of these properties on the flow patterns that develop in mixtures within blenders will help industry design optimal blenders to work with the finer nano-particles being produced today. It is theoretically possible to ascertain the velocity profile of a mixture in a blender from material properties. In fluids, velocity is directly linked to stress through its viscosity, its resistance to shear when in motion [10]. Unlike fluids, bulk solids do not have to be in motion in order to resist shear and therefore do not possess what would be

considered simple viscosity. For granular material there is no simple law relating the stresses to velocity. Plasticity theory, however, does provide the constitutive equations necessary to predict velocity distribution within the granular material in terms of material properties. This theory provides the connection between stress and deformation, or velocity gradient, by utilizing the concepts of *yield function*, *plastic potential* and *flow rule*.

When under normal stress, a well-compacted granular material will flow only when the shear stress attains a critical magnitude, or yield stress. The yield function describes the limiting stress required to initiate yielding and permanent, plastic deformation [11]. When a granular material is exposed to stresses lower than those specified by the yield function, it is said to experience elastic deformation (i.e. the strain imposed during deformation is completely recoverable upon restoring the stresses to its initial state.) This is precisely the reason why strain rate, as opposed to plastic strain, is used in the constitutive equations. There is no clear cut one-to-one relationship between plastic strain and stress; the material from the very start may possess an unknown amount of plastic deformation already locked within it from a previous loading [14]. A number of yield functions have been proposed to describe the onset of yield. The Mohr-Coulomb yield function assumes a rigid, perfectly plastic yield surface in which the granular material does not deform until it reaches the yield criteria, and then yields plastically.

Upon reaching the yield surface, perfectly plastic materials may continue to deform without any change in stress [13]. The magnitude of the plastic flow is unlimited, another reason why plastic strain rate is used over plastic strain. The yield function says nothing about how the granular material deforms or flows, it only describes the onset of yielding. A flow rule must be associated with the yield function in order to relate the stresses that occur during failure to velocity. A plastic potential G is defined where the derivative of G with respect to stress is equal

to the strain rate. For a particular flow rule known as the *associated flow rule* the plastic potential G can be equated to the yield function by the principle of normality, which applies to cases where the rate of displacement is normal to the yield surface. There is considerable debate regarding the validity of the principle of normality during steady flow. During steady flow, stresses are given by the endpoint of the yield locus, in which the normal is undefined [15]. With the associated flow rule losing its validity during steady flow, a new flow rule is sought. Neddermann (advocated by Jenike) [15] proposed using the principle of coaxiality. The principle of coaxiality states that the axes of principal strain rate coincide with the axes of principal stress. Since the principle axes of stress coincide with the principle axes of strain rate, the angle the x-axis makes with the principle directions are equivalent – allowing the constitutive relationship needed between the stress and strain rate. For isotropic materials, materials which have the same mechanical properties in all directions, we expect the principle of coaxiality to apply.

The flow rule provides the final piece of the puzzle. From the material properties, the yield function is defined and then used in collaboration with the flow rule to determine the velocity profile within the mixture. Once the velocity profile of the mixture within the blender is known, the blender's residence time distribution can be determined. Blenders work because there exist differences in residence time within the blender. Knowing the residence time distribution of a particular blender allows one to assess how well it will perform. As mentioned earlier, material properties are not the only criteria affecting the velocity profile. Blender geometry and operational parameters come into play as well. Frictional forces exist between particles of the bed in particle-to-particle contact. Additionally, particles of the mixture come into contact with the inner wall of the blender and other blending components that are specific to

that particular blender such as ribbons and paddles. The criteria used to determine whether shear will occur along the particles of the mixture and the blender inner wall and/or blending components is similar to that used for determining shear plane formation within the bulk. For Coulomb materials, a linear relationship is assumed where the shear stress is related to the normal force through means of the coefficient of wall friction. The absence of stress due to free surface formation has just as much influence, if not more, on the velocity profile within a blender.

If the blending process is not designed in an appropriate manner, the product quality will be compromised and significant financial losses will ensue. Since theoretically forecasting the appropriate blending time for particulate solids is not yet feasible, the amount of energy and time used for blending may exceed the amount necessary – causing an adverse effect on the blending process. An accurate robust blending model is required to predict blending in real systems. The difficulty with obtaining a model is the lack of understanding of the fundamentals of granular mixing.

Despite this shortcoming, several attempts have been made to accurately predict blending. Khakhar and Ottino [1] used a continuum approach to describe blending for a binary mixture in a rotary shell blender. Two different models were proposed. The first model (the static interface model) the plastic-elastic interface is assumed to not vary with time and the free surface to be flat and at a constant incline. The second model (the moving interface model) the plastic-elastic interface along with the free surface are no longer fixed. The thickness of the plastic zone was determined by assuming the particles were abundant enough to be considered a continuum in order to apply a mass and momentum balance, despite the fact that they are orders of magnitude below sufficient numbers for the effects of random fluctuations to be dissipated. By assuming

instantaneous segregation of the binary mixture upon entry into the plastic zone, an assumption that is justifiable if the ratio of the two particle sizes is large enough, it is safe to suppose a uniform constant density across the two layers of particles in the plastic zone. Using observation of pure components, a linear velocity profile was applied to the plastic zone with no slip at the plastic-elastic interface. Noticing that the free surface does not remain fixed and does, in fact, vary with time, Khakhar and Ottino [1] improved on their first model by allowing the plastic-elastic interface and free surface to vary with time. The plastic zone was divided into three sections: a central section of a given length with a fixed angle of inclination, and adjacent sections to the left and right of the central section that are hinged to the end of the central section and allowed to rotate. If the average composition of the adjacent sections is greater than a critical value (f_c), the equilibrium free surface angle (β_{eq}) is set to the angle of repose of either the larger or smaller particle.

A complete understanding of the flow dynamics is not always required. Metchalfe and Ottino [2] were able to accurately predict mixing for monodisperse, weakly cohesion particles when under slow rotation speeds by using simple geometric iterations. Using dyed table salt grains, cubic in shape with a mean side length of 0.6mm, as their particles, they observed that mixing occurs through a series of successive avalanches at the free surface. For slow rotational speeds, the entire duration of the avalanche is uninterrupted as it comes to a complete stop before another avalanche is initiated. The criteria for consecutive flow of avalanches are $\Omega\sqrt{D/g} \ll 1$ where D is the diameter of the drum, g is the acceleration of gravity and Ω is the rate of rotation. Due to the similarity of the avalanches, mixing was represented by a series of successive avalanches where the avalanche morphology was approximated using identical wedges. Mixing was divided into two parts: transport of the wedges, and transport within the wedges. In their

model, as the drum rotated, material formed a surface that was steeper than the static repose angle. This created an unstable condition on the free surface. To overcome this instability they assumed a wedge shaped quantity of material would cascade down the pile and moved in such a way so as to restore the static angle of repose. Transport between wedges was determined by defining quadrilaterals between wedges where successive wedges intersect. Various fill heights were examined. Their assumption, that the duration of the avalanche from formation to end is uninterrupted by other avalanche formation, breaks down when the rotation speed is increased and a second avalanche appears, before the preceding avalanche has expired.

Despite the lack of understanding of granular flow on the macroscopic level, Nase and McCarthy [3, 4] overcame this dilemma by approaching it from an alternative point of view. Unlike the current state of knowledge of granular flow on the macroscopic level the interactions of individual particles amongst one another is quite well understood. Nase and McCarthy [3, 4] used *particle dynamics simulation* to classify the characteristics of bulk flow by simultaneous integration of the interaction forces between individual particles. By applying individual forces to a particle, its trajectory can be obtained by solving Newton's equations of motions. Due to lack of research being done on cohesive materials in addition to contact forces, gravity, normal (Hertzian) repulsion and tangential (Mindlin) friction, Nase and McCarthy [3, 4] added additional particle interaction forces to account for the affect of cohesion. In a mixture, no single component is responsible for cohesion. The attraction particles have for one another is the result of a variety of factors. The most prevalent are Van der Waals forces, electrostatic forces, liquid bridging (capillary forces) and mechanical inter-locking of particle as a result of particle morphology, and surface roughness. Van der Waals and electrostatic forces are only critical for particles 30 microns or less. The predominant factors are surface roughness and capillary forces.

Nase and McCarthy [3, 4] worked with spherical glass beads ranging in size from 0.5 to 10 mm, so the cohesion came entirely from capillary forces in the form of liquid bridges which they varied by using different interstitial fluids of varying surface tension. In their simulations, a liquid bridge is assumed to be formed between particles upon contact, remaining intact until a critical separation distance is reached and the liquid bridge is ruptured. A maximum of two particles can be joined together by a single liquid bridge. Contrary to their initial hypothesis, Nase and McCarthy observed a slight increase in the mixing rate with added cohesion up to a certain value. No explanation was given for this observed phenomenon; it was simply reported. Although Nase and McCarthy had agreement between experiments and simulation, there are still areas requiring further development. Simulations were done for large perfectly spherical particles of uniform size to correspond with their experiments with glass beads. In reality, no particle is perfectly spherical and uniform in size. Neglecting the effect of particle inter-locking is valid for perfectly spherical particles, but breaks down for real particles. Particles vary in both shape and size. Some have broad size distribution and others have narrow size distribution, but none are uniform in size. The likelihood of two particles of equivalent size forming a liquid bridge is slim. The equation utilized in their stimulation for capillary forces between particles is for two particles of equal size. Agglomerates in real systems are composed of two or more particles of various sizes. In industries such as pharmaceuticals, active components are well below 30 microns and, therefore, susceptible to the influence of Van der Waals and electrostatic forces. Currently, there is insufficient computational power available to run simulation with adequate number of particles to model mixtures with particles of that small of a size range in an industrial or lab-scale blender.

Blenders work because there exists a difference in residence time between particles within a blender. Particles that enter the blender at the same time are not confined to exit at the same time, since each particle takes its own stochastic path. In an ideal blender, a uniform residence time distributions exists, allowing a particle that just entered the blender to exit at the same time as a particle that has been in the blender for the maximum residence time. Danckwerts [5] devised a method to assess blender performance through means of its residence time distribution. By injecting a stream of tracer particles into the blender and monitoring its duration in the blender, the residence time distribution is easily obtained. Variations in material properties such as cohesion, particle size distribution, and internal angle of friction affect the flow properties of a mixture – changing the velocity profile within the blender, and having a direct impact on the residence time distribution. If one can acquire the velocity profile from material properties, the necessary separation of the material properties influence from operation parameter influence on blender can be achieved. Once the residence time distribution is known, the blender efficiency is evaluated through what Danckwerts termed the variance reduction ratio. The variance reduction ratio is defined as the ratio of the blender's inlet variance to that of its outlet variance. Due to the random nature of the particles, flow fluctuation in the inlet and outlet streams will always persist. The variance reduction ratio measures how well the blender removes inconsistency in the input stream. The variance reduction ratio is composed of residence time distribution and the autocorrelation function that measures the relationship between neighboring samples at set spatial or temporal intervals τ that are related.

At first glance, it appears that Danckwerts' method of assessing blender efficiency is restricted entirely to continuous blenders, blenders that have a well defined input and output streams. How else would one be capable of obtaining a residence time distribution for a batch

blender if the particles are never able to exit the system? The truth is, the same methodology that Danckwerts applied to continuous blender can be applied to batch blenders.

The purpose of a blender is to remove inconsistency and produce a mixture as homogeneous as possible. Blenders do this in a variety of ways. Some use moving pieces like ribbons and paddles to physically throw material from one location to another, while others use natural physical tendencies of the mixtures to form shear zones within the bulk that exhibit a distribution of velocities allowing particles to travel past one another at various speeds, thereby initiating separation. Regardless of the type of blender, whether it be a ribbon, v-blender or rotary shell, blending can be broken into small increments where one increment describes the full assortment of blending events that occur. Ribbon and paddle blenders typically consist of a series of ribbons and paddles, some that propel, aligned such that material is propelled alternately forward and backwards. For these types of blenders, one increment would constitute one set of forward and backward projecting ribbons or paddles. In a rotary shell blender there are no moving extremities; blending is accomplished solely through the avalanching process. One increment for the rotary shell blender would be one avalanche since it describes in its entirety the whole span of blending events that transpire.

Once these blending increments are defined for a particular batch blender they can be placed in a repeating series or loop. A batch blender can be described as a continuous blender with a recycle stream where one blending increment constitutes one cycle. If a transfer function can be obtained for these elementary blending increments relating the concentration of the mixture before and after completing one blending increment, the concentration of the blender as a whole can be calculated by a simple algebraic equation which will enable one to predict the concentration after completion of n increments. If a unit impulse is applied to a system,

representing one blending increment, then the transfer function would be identically equivalent to the residence time distribution function. By placing a thin layer of markers that characterize a unit impulse at the start of a blending increment and monitoring when they exit, the transfer function for the blender is readily obtained.

Experiments were performed using a rotary shell blender with sand as the medium, approximately 600 microns in size, at various cohesion levels. The data was compared with simulations created using an in-house written code. The rotary shell blender was 1/3 fill with white sand with a small strip of black sand in the upper right hand corner constituting 5% of the total mixture by weight. The black and white sand are identical in every way except in color. Noticing that axial segregation only occurs after prolonged periods of time, well after uniform mixing is achieved, it is assumed that blending anywhere axially is representative of the whole. The blender's performance was calculated with the residence time distribution which was determined through optical means using threshold analysis.

Two models are proposed to account for the formation of the plastic flow regime and its velocity distribution. One model assumes the shape and velocity of the plastic regime while the other uses lines of characteristics. In the first model the plastic regime is described in geometric terms. During experimentation it was noted that the shape of the flowing plastic regime, particularly at lower cohesion values, could be approximated by a parabola with a nearly flat free surface. The flowing layer thickness $\delta(x)$ varies along the length of the free surface with its thickest point located in the center. The thickness at the center, δ_0 , was chosen based on material properties. Sokolovskii [6] in his work on slope stability provides an analytical solution for the thickness of avalanches formed in material when the pile inclines at angles larger than those of

the angle of repose. δ_0 was then based on Sokolovskii's equation using the material strength at the stress state imposed in the blender

The velocity profile within the plastic regime is expressed using an exponential relation with the maximum velocity, $a(\delta)$, occurring at the free surface. Values of $a(\delta)$ are not constant but vary along the free surface. The coefficient, k_1 , of the exponential decay of velocity within the plastic regime from the top of the free surface to the bottom of the plastic-elastic interface was arbitrarily chosen. Particles outside the plastic regime travel as a rigid body in a circular path with a velocity of ωr . Particles continually enter and exit the plastic regime through the rigid body rotation of the elastic region. Applying a volumetric mass balance between the inlet flow from the elastic region that of the plastic region, $a(\delta)$ can be solved for by integrating the flow rate normal to delta lines, drawn perpendicular from the top of free surface to the bottom of the plastic-elastic interface, with respect to its length

The second model proposed has considerable advantages over the first. Unlike the first model described, the second model does not assume any form of plastic region nor does it assume a velocity profile within it. From known stresses acting along the free surface and along the inner wall of the blender, lines of characteristic are drawn. These lines extend into the bulk of the material, intersecting one another along the way, until they merge with the plastic-elastic interface where the characteristic lines cease to exist. This method is known as the method of characteristics. Material properties are incorporated through the stresses acting along the free surface and particle wall interaction which were non-existent in the preceding model. The stresses that occur at the intersection of the characteristics are acquired by solving the characteristic equations simultaneously with the equilibrium equations in conjunction with the yield criteria. Stresses elsewhere in the plastic regime were obtained by linear extrapolation of

the stresses at the intersection of the characteristics. Being cognizant of the stresses throughout the plastic regime enables one to determine the velocities in terms of material properties, as opposed to relying on a geometric formula to describe the velocity tendency of the mixture. Analogous to the manner in which characteristic lines were constructed in determining the stresses within the plastic regime, characteristic lines were initiated along the free surface that extend to the plastic-elastic interface allowing for the calculation of velocity at the intersections. Applying the principle of coaxiality, the velocity at the intersections of the velocity characteristics can be related to the stresses obtained earlier from the intersection of the stress characteristics.

In both models, the free surface starts off flat and parallel with the horizontal. Slowly the drum and its contents are allowed to rotate to the point of static equilibrium. Methods and procedures to determine the stability of a slope were borrowed from soil mechanics. Civil engineers are aware of the dangers caused by slope failure. Improper designs have led to the collapse of a number of bridges and roads. In October 1961, the strength of soil samples was drastically underestimated due to the anisotropic nature of the soil resulting in sliding along a 1500 ft section of the Waco Dam. As a result of these failures, in recent decades a great deal of new understanding of slope stability has emerged and measuring techniques and methods have been significantly improved. Through the experience and lessons learned from others' failures we gain a better understanding of the complex nature of granular material. Stability calculations must be performed to ensure that the material's strength, its ability to resist flow, is greater than that of the applied forces. The safety factor is a term employed by civil engineers to show a sample's likelihood to fail. It is the ratio of the available shear strength of the material to that of the equilibrium shear stresses. Mohr-Coulomb equations are used to express the shear strength of

the material in terms of its cohesion and internal angle of friction. Provided the safety factor is larger than 1, failure should not be a concern. In order to perform a stability calculation a slip surface must first be assumed. Typically a number of slip surfaces are assumed in order to find the slip surface that produces the minimum factor of safety. The slip surface with the minimum factor of safety is called the critical slip surface and represents the most likely surface to fail.

A single value for the factor of safety is representative of the entire slip surface. In reality materials are not exposed to a uniform stress throughout and, therefore, possess different factor of safety values along the slip surface. Hence, the factor of safety is an average or overall value. The only time that the factor of safety would in fact be a constant would be if failure is actually initiated, in which case the shear stress would be equal to the shear strength at all points along the failure surface.

Once the slip surface is assumed, two different approaches are available to ascertain whether failure will ensue. Either the static equilibrium equations are employed for the entire body of the material, or the body of the mass is divided into slices, the static equilibrium equations are applied to each slice individually, and failure is determined from the summation of the individual slices. The *infinite slope* and the *logarithmic spiral* procedures are two that consider the body as a whole and the *ordinary method of slices* along with the *simplified Bishop* method divide the body into slices. Regardless if the equilibrium equations are applied to a single body or to a series of individual slices, it is necessary to employ a number of assumptions because the number of unknowns (forces, locations of forces, factor of safety, etc) exceeds the number of equilibrium equations. The problem is indeterminate. Depending on which method is employed, different assumptions are made. Some methods use all the equilibrium equations while others do not. Which method to employ should be decided on a case-to-case basis. The

infinite slope procedure considers the body of the material as a whole. It is called the *infinite slope* procedure because the slope is assumed to extend infinitely in all directions. As a direct consequence of this assumption the stresses on any plane perpendicular to the slip surface, which runs parallel with the free surface, will be equivalent.

An equilibrium balance is applied to a rectangular element within the slope from the assumed slip surface to the top of the free surface. The stresses on the ends of the rectangular element are equal and opposite to one another, an effect of the assumption of an infinite slope. The weight of the material gives rise to the normal and shear forces along the base of the rectangular element. Since the normal and shear forces along the base of the rectangular element come solely from the weight of the material, the rectangular shape of the element produces a uniform and constant force. The infinite slope procedure is not a good choice for our model of the slip surface in a rotary shell blender. The length of the slip surface is not infinite but is confined to the dimension of the blender. There is a clear and obvious deviation in the thickness of the plastic region. The plastic region starts with a thickness of zero at the perimeter of the drum and steadily increases to a maximum at the center. The normal and shear force at the slip surface vary along with the weight of the material directly above it. The assumption of a rectangular element with uniform and constant stress at the slip surface is invalid.

Another method that considers the body of the material as a whole is the *logarithmic spiral* procedure. The *logarithmic spiral* and *infinite slope* procedures are the only two methods that fully satisfy all equilibrium equations by assuming a finite, definite shape for the slope. The shape of the slope is defined by placing a center point and an initial radius above the slope surface. This maps out a logarithmic spiral for the slope. The shear stress along the slip surface is expressed as a total stress in terms, of the normal stress, assuming that the logarithmic nature

of the slip surface and the complete solution to all the equilibrium equations the *logarithmic spiral* procedure is relatively accurate. For homogeneous slopes the *logarithmic spiral* procedure seems to agree well with actual slopes. During the blending process particles of various properties are continually redistributed. In the initial stages of blending, the slopes will be anything but homogeneous in nature. Whether the *logarithmic spiral* procedure will be accurate in these cases is unclear. However, the principal reason this method was not used is because we know the location of the plastic-elastic interface. Since we simply need to know at what point the slope becomes unstable, there is no need to assume slip surfaces at various locations.

We used one of the methods of slices to calculate the stability of the slopes in our models. The method of slices divides the body of material into slices as opposed to evaluating the body as a whole as with the *infinite slope* and the *logarithmic spiral* procedures. The width of each slice is arbitrarily selected; the slices do not have to be of the same width. The width is, however, limited in size so that the base of each slice can be approximated by a straight line. The normal and shear forces acting on the base are determined by resolving the force imposed by the weight of the material in each individual slice. The equilibrium balance equations are applied to slices individually. The principal difference between the *ordinary method of slices* and the *simplified Bishop* procedure is with regard to how they deal with the forces on the side of the slices. The *simplified Bishop* procedure assumes that there are no shear forces acting on the sides of the slices, that all acting forces are normal. In the case of *ordinary method of slices*, the forces on the side of the slices are neglected altogether. The assumption is that the width of the slices is small enough that the forces on the sides of the slices are equal and opposite and cancel

one another. Sufficient slices were used in our models that the *ordinary method of slices* was applied.

Upon defining the plastic and elastic regions and establishing the slope in which equilibrium is achieved, tracers are introduced into the system. Two sets of simulations were performed with the tracers placed in drastically different manners. The first set of simulations was designed to mimic the experiments performed in the lab. A number of tracers were placed adjacent to one another in multiple rows and columns. Discovering that this wasn't the ideal location for the placement of the tracers, a second set of simulations was performed. The second set of simulations was performed with a single strip of tracers positioned at the center of the bed of the material starting a short distance below the elastic-plastic interface and extending to the periphery of the inner wall of the drum.

CHAPTER 2 MODEL DEVELOPMENT FOR ROTARY SHELL BLENDERS

In a rotary shell blender there exist two distinct regions: a plastic region along the top of the free surface in which particles follow different trajectories with velocities of various speeds and an elastic region where the particles move as a rigid body. Particles in the elastic region travel in a circular path always remaining parallel with one another, never to cross trajectories. Blending takes place solely in the plastic region where the velocity profile allows particles to travel past one another, resulting in particle separation. The shape and size of the plastic region, along with the velocity distribution, govern how well the blender performs. Blenders that contain mixtures with the propensity to exhibit thinner plastic regions generally produce products of poorer quality if not mixed sufficiently and are, therefore, inclined to require longer periods for blending to achieve the same quality as that of a mixture with a larger plastic region. Since blending occurs entirely in the plastic region, mixtures with larger plastic regions allow for greater blending as they can accommodate a greater number of particles. Too large of a plastic region has an adverse effect, in which we see a decline in blending. The plastic region increases in size as a direct result of an increase in strength. With greater strength the plastic region is temporarily capable of withstanding inclination angles larger than those of the angle of repose, resulting in a cascading mechanism in which we no longer have a smooth continuous region, but a series of chaotic avalanches. The blending that occurs in these cascades is not as pronounced as the blending that occurred at lower cohesion values. Optimal blending occurs when the plastic region size allows for the maximum number of particles without affecting the velocity gradient across the region. The attractive forces of the particles caused by Van der Waals and electrostatic forces – along with surface roughness, particle morphology, liquid bridges, etc. which vary with particle size, shape and other material properties – affects the particles overall

cohesion. This directly affects the shape, size and flow properties of the plastic region. Due to the complexities and difficulties that arise with cohesion, most published works have dealt with non-cohesive materials [16, 17, 18, 19 and 20]. Due to the strong influence of cohesion on the blending process, and the abundant numbers of naturally cohesive materials, cohesion can no longer be ignored. Cohesion plays a vital role in both proposed models. In the parabolic model, a parabola describes the shape of the plastic region while the method of characteristics model relies on the material properties to dictate its morphology.

Determination of Plastic Region for Parabolic Model

Through experimental observation it was noted that a parabola could be used to accurately describe the plastic region through geometric means, particularly for material with low cohesion values. The thickness of the plastic region varies along the x-axis as follows:

$$\delta(x) = \delta_o \left[1 - \left(\frac{x + an}{an} \right)^2 \right] \quad (2-1)$$

where an is half the length of the free surface and δ_o is the thickness at the center. The thickest point of the plastic region occurs at the center value δ_o and tapers to zero on both sides. The

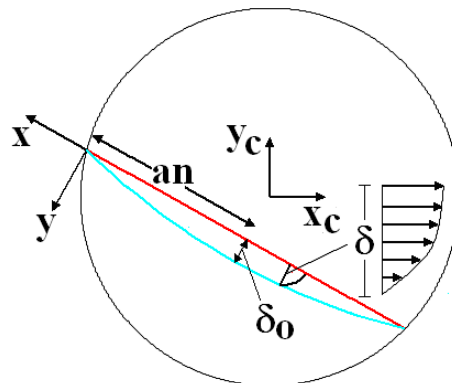


Figure 2-1. Schematic view of flow geometry with corresponding coordinate system

thickness at the center, δ_o , is attained using the Sokolovskii [6] equation 2-2 below to determining the thickness of the failure region of material inclined at angles larger than those of the angle of repose.

$$\delta_o = \frac{\sigma^* \sin(\phi)}{\gamma \sin(\varepsilon)} \tag{2-2}$$

σ^* is the mean stress, defined as the distance from the center of the Mohr circle to the point where the internal yield locus cuts the sigma-axis. σ^* is expressed in terms of f_c , the unconfined yield stress.

$$\sigma^* = \frac{f_c}{2} + c \cot(\phi) \tag{2-3}$$

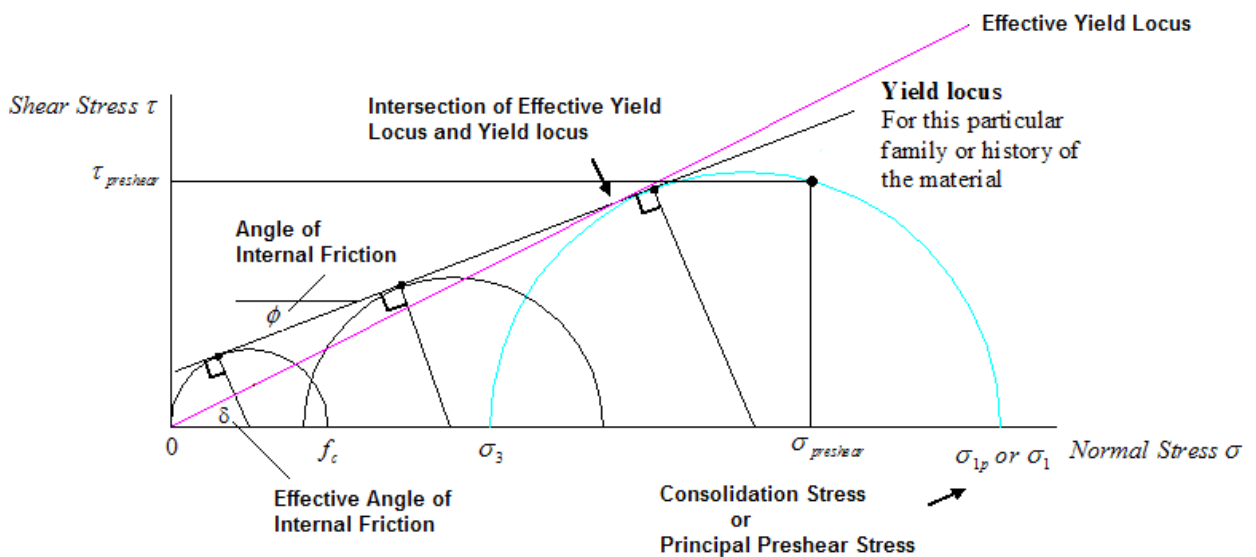


Figure 2-2. Series of Mohr circle for a particular consolidation stress

Unconfined yield strength is the largest major principle stress that would cause an unconfined section of bulk material to fail or yield in shear. It is described by the major principle stress of the failure Mohr circle as the minimum principle stress passing through zero.

When in an unconfined state, the unconfined yield stress is representative of the strength of the material. The unconfined yield stress is dependent upon the consolidation pressure acting on the bulk material. As the bulk material is exposed to larger and larger loads, particles within the bulk are rearranged and become more closely compacted, increasing the strength of the material. Associated with every unconfined yield strength is a corresponding consolidation stress, σ_1 . The consolidation stress for a particular unconfined yield strength is given by the major principle stress of the consolidation Mohr circle furthest to the right in cyan in figure 2-2. Bulk material in a rotary shell blender is not exposed to any loads other than the self weight of the bed. The consolidation stress is taken simply as

$$\sigma_1 = \rho g h \tag{2-4}$$

where h is the maximum height of the bed. Refer to figure 2-3

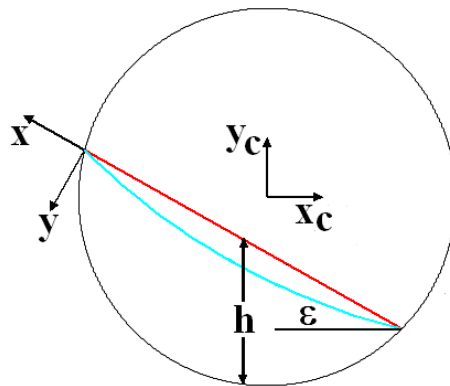


Figure 2-3. Height of material used for determining consolidation load

Velocity Within Plastic Region for Parabolic Model

Once the thickness of the plastic region is established, we can proceed in calculating the velocity profile. Due to its simplicity, other researchers such as Khakhar [1] have assumed a linear velocity profile. Allowing for a more flexibility, the velocity within the plastic region is assumed to vary exponentially in accordance with equation 2-5 with the maximum velocity, $a(\delta)$, occurring at the free surface.

$$v_{plastic}(y) = a(\delta) \left[1 - \exp \left\{ -k_1 \left(1 - \frac{y}{\delta} \right) \right\} \right] + k_2 \quad (2-5)$$

As y approaches δ , descending deeper into the plastic region, the term to the left in equation 2-5 exponentially decays until inevitably reaching zero. Being that a zero velocity along the elastic-plastic interface is not plausible the parameter k_2 was supplemented to the equation.

Analogous to $a(\delta)$ k_2 was allowed to vary with avalanche thickness by setting its value to a fraction of that of $a(\delta)$. The coefficient, k_1 , the exponential decay of the velocity within the plastic region from the top of the free surface to the bottom of the plastic-elastic interface was arbitrarily chosen. Table 1-1 provides the velocity profile within the plastic region as a function of depth at various k_1 values, in terms of the maximum velocity at the free surface $a(\delta)$ and the maximum depth at the center δ_o . Note the sensitivity of $v_{plastic}(y)$ with respect to k_1 . k_1 values larger than 9 for all practical purposes constitute plug flow.

Table 1-1. Velocity within plastic region as a function of depth at various k_1 values

y	<u>$k_1=1$</u> Vplastic(y)	<u>$k_1=3$</u> Vplastic(y)	<u>$k_1=5$</u> Vplastic(y)	<u>$k_1=7$</u> Vplastic(y)	<u>$k_1=9$</u> Vplastic(y)
0.00 δ_o	0.6321 a(δ)	0.9502 a(δ)	0.9933 a(δ)	0.9991 a(δ)	0.9999 a(δ)
0.25 δ_o	0.5276 a(δ)	0.8946 a(δ)	0.9765 a(δ)	0.9948 a(δ)	0.9988 a(δ)
0.50 δ_o	0.3934 a(δ)	0.7769 a(δ)	0.9179 a(δ)	0.9698 a(δ)	0.9889 a(δ)
0.75 δ_o	0.2212 a(δ)	0.5276 a(δ)	0.7134 a(δ)	0.8262 a(δ)	0.8946 a(δ)
1.00 δ_o	0.0000 a(δ)				

Values of $a(\delta)$ are not constant along the free surface, but vary with δ , the thickness of the plastic region as it changes with x . Values of $a(\delta)$ are obtained using a volumetric mass balance, equation 2-6, for the flow rate of material passing through the δ lines that run perpendicular from the top of the free surface to the bottom of the elastic-plastic interface.

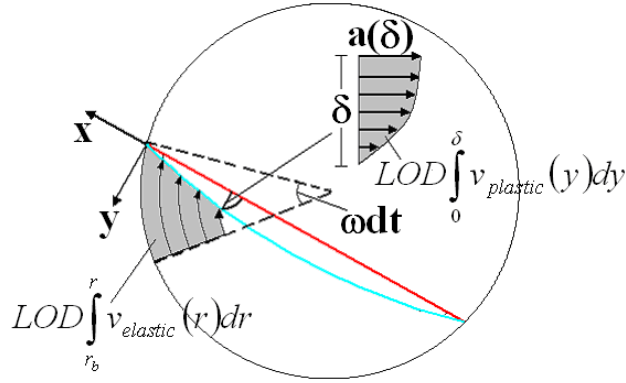


Figure 2-4. Velocity profile within plastic region

$$LOD \int_{r_b}^r v_{elastic}(r) dr = LOD \int_0^{\delta} v_{plastic}(y) dy \quad (2-6)$$

Particles constantly enter and exit the plastic region from the elastic region that continuously supplies and absorbs particles. The integral of $v_{plastic}(y)$ from 0 to δ for a particular delta line is equal to the flow rate of particles entering from the elastic region (see figure 2-4). Figure 2-4 is a schematic of the volumetric mass flow of material that passes through a particular delta line, and must balance with the volumetric mass flow of material supplied from the elastic region – constituting a volume depicted by the shaded region after rotating an increment ωr . The inlet of particles from the elastic region is obtained by integrating, $v_{elastic}(r)$ the velocity in the elastic region, from r_b (distance from bottom of delta line to center of drum) to r (drum radius). Particles in the elastic region move as a rigid body with a velocity of

$$v_{elastic}(r) = \omega r \quad (2-7)$$

where ω is the angular velocity and r is the radial distance the particle is from the center of the drum.

Plugging equations 2-5 and 2-7 into equation 2-6 yields the following equation for $a(\delta)$ as a function of δ , the thickness of the plastic region

$$a(\delta) = \frac{\frac{\omega r^2}{2} - \frac{\omega r_b^2}{2}}{\delta \left[1 + \frac{1}{k_1} - \frac{1}{k_1} \exp(-k_1) \right]} \quad (2-8)$$

Figure 2-5 is a graph of the maximum velocity for the delta lines along the free surface versus the thickness of the delta lines. Note that $a(\delta)$ decreases as $\delta(x)$ increases, with the highest velocity occurring at the tips of the plastic region and the lowest velocity occurring at the center, corresponding with the thickest point along the free surface with a $\delta(x)$ value of δ_o .

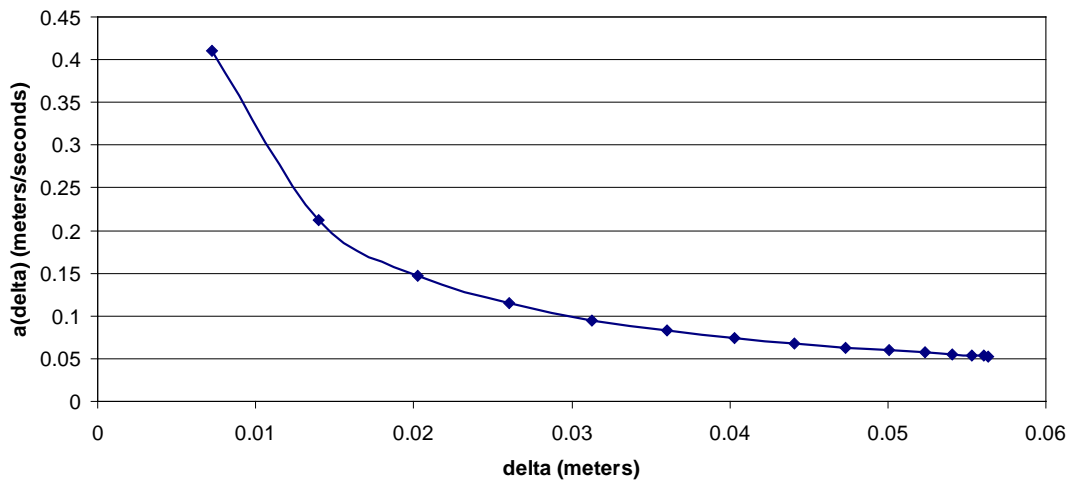


Figure 2-5. Velocity along free surface vs. thickness of plastic region

According to equation 2-8 as $\delta(x)$ approaches zero $a(\delta)$ approaches infinity. Since we are dealing with real particles they must be confined to some finite velocity. Being unable to accurately capture the essence at low delta values, an obvious fault in the equation, modifications were augmented to the program in which the simulations would be run, which compensated for this shortcoming. A scaling factor was applied to the velocity profiles that happen to lie within a given area from the upper and lower tips of the plastic region. Refer to figure 2-6.

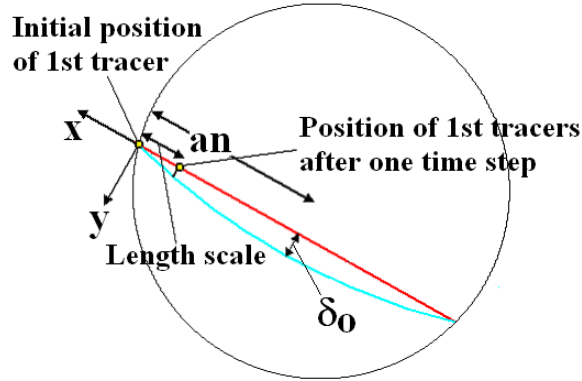


Figure 2-6. Scaling factor for particles at tips of avalanche

The area in which the scaling factor would be applied was established by positioning a tracer particle, shown as a yellow dot in figure 2-6, at the very edge of the free surface. The distance the tracer particle would travel if it had a velocity specified by equation 2-8 was calculated and termed as the “length scale”. The plastic region a distance “length scale” from the top of the plastic region as well as the plastic region a distance “length scale” from the bottom was deemed as possessing unrealistic velocities and were multiplied by a scaling factor. Since the velocity scales with $\delta(x)$ the thickness of the plastic region and $\delta(x)$ varies with distance along the free surface according to equation 2-1, with the slowest velocity occurring at the center a distance an from the top of the free surface, the scaling factor is defined as

$$sf = \frac{\text{length scale}}{an} \quad (2-9)$$

The majority of the tracer particles that travel through the plastic region will never reach the lower portion of the plastic region as they are engulfed into the elastic region prior to entry, but for the limited numbers that do they are susceptible to the possibility that their current trajectory while in the plastic region may propel them a distance outside the periphery of the drum. In actuality upon impact with the inner wall of the drum the particle would simply come to a halt where they would then enter the elastic region rotating as a rigid body. For the scarce

number of tracer particles that do happen to depart from the inner wall of the drum the particles are then repositioned inside the wall a tiny fraction from the periphery where they then begin to rotate as if they were already in the elastic region.

Determination of Plastic Region Method of Characteristics

A second method is proposed to predict the blending behavior in a rotary shell blender. This method requires no assumption of the form that the plastic region takes, nor any specific velocity profile. The form of the plastic region, along with the velocity profile, is based on the material properties of the mixture and the operation parameter of the blender. There are no restrictions, no requirement of symmetry, and the plastic region allows the physics of the problem to dictate its morphology. This method that is used to describe the blending behavior with such profound advantaged over all previous methods is the method of characteristics. The method of characteristics is not a new method, it has be around for quite some time. Due to its amazing ability to accurately describe blending, the method of characteristics it is being used for the first time in this application.

Defining the rectangular coordinate x,y in such a way that the x-axis is inclined from the horizontal at an angle of $180^\circ - \varepsilon$, where ε is the angle of inclination of the free surface, the x-axis is aligned with the free surface pointing away from the blender with its origin at the uppermost left corner of the bed. The y-axis points downward toward the material (see figure 2-3). The reason for choosing the coordinate system in such a way will become clear as we proceed. Writing the differential equations of plane equilibrium in Cartesian coordinates for granular material in terms of the above described coordinate systems we obtain the following partial differential equations.

$$\frac{\partial \sigma_{xx}}{\partial x} + \frac{\partial \tau_{yx}}{\partial y} = -\gamma \sin \varepsilon \tag{2-10}$$

$$\frac{\partial \sigma_{yy}}{\partial y} + \frac{\partial \tau_{yx}}{\partial x} = \gamma \cos \varepsilon \quad (2-11)$$

where compression stresses (σ_{xx}, σ_{yy}) are taken as positive since granular material can rarely withstand tension. Following this convention, the Mohr circle dictates the shear stresses (τ_{xy}, τ_{yx}) should be positive when acting on an element in the counterclockwise direction. In order to ensure stability

$$\tau_{xy} = -\tau_{yx} \quad (2-12)$$

The unknowns $\sigma_{xx}, \sigma_{yy}, \tau_{yx}$ in equation 2-10 & 2-11, which fully specify the stress state of a material under plane stress conditions, must satisfy some form of yield criteria when in a state of incipient or actual yield. A number of yield criteria exist, but the most commonly used and known is the Coulomb's criteria. The shear stress for a Coulomb material is independent of either the extent or rate of deformation, but depends on the normal force applied to it. The *Coulomb yield criterion* takes the form

$$\tau = \mu\sigma + c \quad (2-13)$$

where μ and c are the coefficient of friction and the cohesion of the material.

Although powders are neither solids, liquids or gases, they have traits associated with all three states of matter. Powder can withstand deformation like solids. Under certain circumstances, they exhibit flow ability like liquids. Powder can also be compressed to a certain degree like gases. Powders are in a class of their own. Powder may flow due to stress that is mechanically applied or under the influence of its own weight. However, the principal of that flow is distinctly different from that of a liquid. If the stresses are not sufficiently large enough, flow will not commence at all. Due to individual particle interlocking frictional forces arise, giving powders shear strength which enables them to form piles – a trait not associated with

liquids. If a powder undergoes consolidation, cohesion forces develop. Cohesion is the mutual attraction of the solid particle for one another, and is measured on the bulk scale as the amount of shear stress necessary to cause yielding at conditions of zero normal pressure. A number of factors contribute to cohesion. The predominant factors in normal dry conditions are Van der Waals forces along with electrostatic forces, and friction forces induced by the orientation and roughness of the particles. Under humid conditions, the adsorption of water leads to formation of liquid bridges and, in some instances, caking. When sufficient stress is applied, flow is initiated. This flow does not depend on the strain rate, as is the case of fluids, but rather depends on the normal stress acting on the powder as shown by equation 2.13.

The Coulomb yield criteria is an idealize criteria in the sense that it assumes a linear relationship between normal and shear stresses. There are many materials, *ideal Coulomb materials*, that conform to this ideology. There is, however, a slight curvature when plotting the shear stress versus normal stress. For all practical purposes this curvature is neglected and approximated by a straight line. The linear relationship μ between the normal and shear stress is the coefficient of friction. The coefficient of friction is experimentally measured and ranges from 0.3 for smooth spherical particles to 1.5 for angular particles. Generally, if the shear stress, τ , along any plane of an *ideal Coulomb material* is less then $\mu\sigma + c$ failure will not be initiated. Failure results only when stresses equal $\mu\sigma + c$. Stresses lager then $\mu\sigma + c$ are not feasible, except transiently. Once failure occurs, particles are in motion and no longer in static equilibrium with one another.

The Coulomb's failure criteria defines a upper limit for the maximum shear stress a granular material can withstand, before failure is initiated, in terms of the normal stresses imposed upon it. Using the Coulomb's failure criteria in conjunction with the Mohr circle we

infer that a granular material will fail based upon its state of stress at various locations within the bulk. Stress being a continuum concept is considered along planes within the bulk as opposed to individual particle interactions. Local stresses exist within the bulk which transmit an average stress across these planes. Consider an element of volume within a continuum with all forces acting on it. If its volume is reduced to zero so that only a point remains, the body forces would go to zero and only surface forces would remain. At this point the surface forces are in equilibrium with one another. This is the material's state of stress for the point considered. The total state of stress at a point in the bulk is represented by nine components, three normal stresses and three shear stresses.

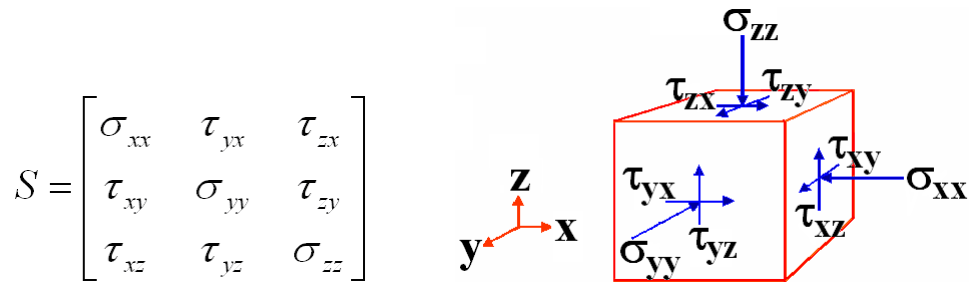


Figure 2-7. Stresses acting on a unit of volume in Cartesian coordinate

The state of stress can also be represented by three invariants known as the principal stresses. This state of stress is identical to those of the stresses above only the orientation of the axes have changed. Along the principal axes only normal stresses reside, shear stresses are zero.

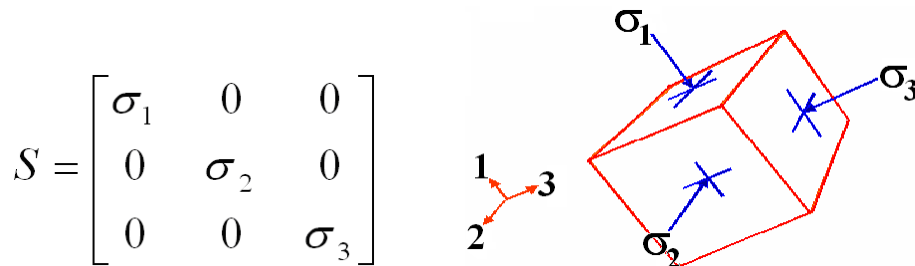


Figure 2-8. Stresses acting on a unit volume in principal coordinate

A convenient way of representing the state of stress of a material along certain points within the bulk is Mohr circles. The Mohr circle is a two-dimensional representation of the state of stress. Three values are required to describe a Mohr circle, two normal stresses and one shear stress. In the special case when the shear stresses are equal to zero and the normal stresses are principal stresses only the minor and major principal stress are considered, neglecting the intermediate principal stress altogether. The minor and major principal stress dictate the formation of the shear plane. Therefore, the intermediate principal stress is not used in the two-dimensional depiction of the state of stress in the Mohr circle diagram. The Mohr circle is plotted in normal and shear stress space with the normal stress plotted along the abscissa and the shear stress plotted along the y-axis. Every point on the Mohr circle is equivalent. The Mohr circle represents all the valid, feasible combinations of normal and shear stresses that would produce the same behavior of the bulk. The stress state defined by (σ_{xx}, τ_{xy}) , (σ_{yy}, τ_{yx}) would elicit the same response as a stress state defined by $(\sigma_1, 0)$ $(\sigma_3, 0)$.

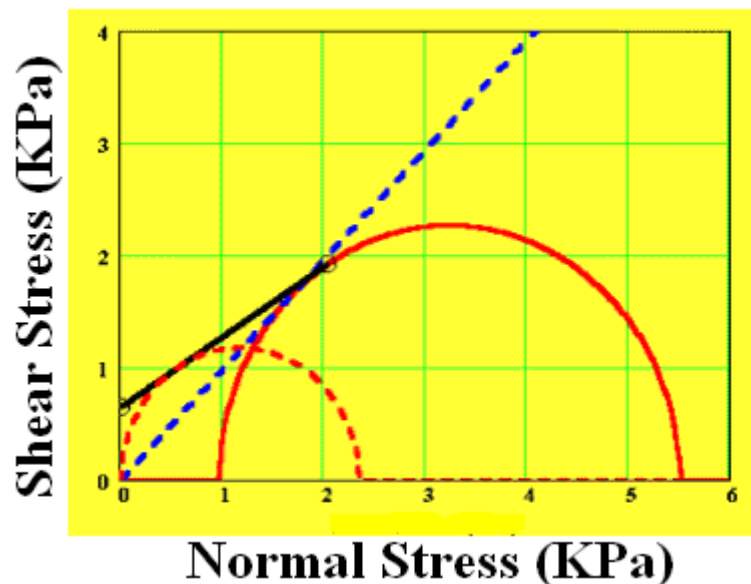


Figure 2-9. Mohr circle diagram

Plotting the Coulomb yield criteria alongside the Mohr circle presents two possible scenarios. Either the Mohr circle is entirely below the Coulomb yield line, also referred to as the *internal yield locus*, in which case $\tau < \mu\sigma + c$ along all planes through point of interest, or the Mohr circle makes contact with the internal yield locus. If the latter ensues, there exists a plane that passes through the point of interest in which $\tau = \mu\sigma + c$ and the material is said to be in a state of incipient yield.

There are a number of Mohr circles associated with every yield locus. Two Mohr circles of particular interest are the failure and consolidation Mohr circles. When granular materials are consolidated they undergo a change in strength as particles within the bulk start to rearrange themselves, filling interstitial voids and interlocking with one another. The stress the material experiences during consolidation is the consolidation stress. The consolidation stress describes the strength of the powder when compacted. The largest Mohr circle, the consolidation circle, represents the consolidation state of the powder with all subsequent circles to the left representing the material's state of stress at lower normal loads. The circle that has its minor principal stress intersecting the origin is referred to as the failure Mohr circle. The major principal stress of this Mohr circle is the unconfined yield stress, f_c . The unconfined yield stress is the strength of the material; it is the stress required to initiate shear when confined to a load of zero.

The combined use of the ideal Coulomb criteria with the Mohr circle is the *Mohr-Coulomb failure analysis*. It is used to derive the equation necessary to describe bulk material yield.

$$\begin{aligned} & \sin \phi \sin 2\psi \left(\frac{\partial \sigma^*}{\partial x} \right) + 2\sigma^* \sin \phi \cos 2\psi \left(\frac{\partial \psi}{\partial x} \right) \\ & + (1 - \sin \phi \cos 2\psi) \left(\frac{\partial \sigma^*}{\partial y} \right) + 2\sigma^* \sin \phi \sin 2\psi \left(\frac{\partial \psi}{\partial y} \right) = \gamma \cos \varepsilon \end{aligned} \quad (2-18)$$

with the unknowns σ^* and ψ with respect to coordinates x and y . Cohesion does not appear explicitly in the above partial differential equations, but does become relevant upon introduction of the boundary conditions.

The method of characteristics is a convenient and fast way of solving certain types of first and second order partial differential equations by utilizing the fact that along certain curves called characteristics, these equations reduce to ordinary differential equations which are considerably easier to solve than the original partial differential equations. In general, any curve, u , in the xy -plane can be expressed in parametric form; where the parameter s gives the measure of the distance along that curve.

$$u(x, y) = u\{x(s), y(s)\} \quad (2-19)$$

Through the law of vector resolution we evaluate the gradient of σ^* and ψ along a curve, its distance along this curve denoted by s , at an arbitrary angle ζ measured counter clockwise from the x -axis.

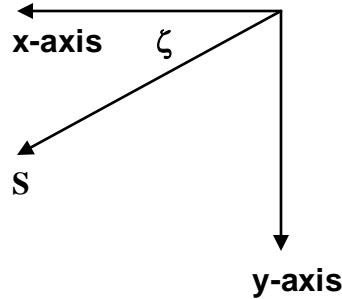


Figure 2-11. Characteristic direction

$$\frac{d\sigma^*}{ds} = \left(\frac{\partial \sigma^*}{\partial x} \right) \frac{\partial x}{\partial s} + \left(\frac{\partial \sigma^*}{\partial y} \right) \frac{\partial y}{\partial s} = \frac{\partial \sigma^*}{\partial x} \cos \zeta + \frac{\partial \sigma^*}{\partial y} \sin \zeta \quad (2-20)$$

$$\frac{d\psi}{ds} = \left(\frac{\partial\psi}{\partial x}\right)\frac{\partial x}{\partial s} + \left(\frac{\partial\psi}{\partial y}\right)\frac{\partial y}{\partial s} = \left(\frac{\partial\psi}{\partial x}\right)\cos\zeta + \left(\frac{\partial\psi}{\partial y}\right)\sin\zeta \quad (2-21)$$

Subtracting equations 2-17 and 2-18 from one another and utilizing the gradient of σ^* and ψ with respect to s , it is found that along two directions the partial differential equation reduces to an ordinary differential equation. These directions are the alpha and beta directions. Alpha, when $\zeta = \psi - \mu$, and beta, when $\zeta = \psi + \mu$. The curves at which these angles occur are the alpha and beta characteristics, and are expressed by the following equations.

$$\frac{dy}{dx} = \tan(\psi - \mu) \quad (2-22)$$

$$\frac{dy}{dx} = \tan(\psi + \mu) \quad (2-23)$$

It should be noted that μ is not an arbitrary, random angle arrived at through the mathematics, but carries physical significance. The characteristic directions alpha and beta are inclined at an angle of $\pm \mu$ from the major principal stress direction, which is inclined counter clockwise from the x-axis at an angle of ψ . Referring to figure 2-11, in a similar fashion the slip lines also incline from the minor principal stress plane at an angle of $\pm \mu$. The characteristics lines align themselves with the slip lines. The ordinary differential equations that result along these curves are

$$d\sigma^* - 2\sigma^* \tan\phi d\psi = -\gamma[(\cos\epsilon \tan\phi + \sin\epsilon)dx + (\sin\epsilon \tan\phi - \cos\epsilon)dy] \quad (2-24)$$

$$d\sigma^* + 2\sigma^* \tan\phi d\psi = \gamma[(\tan\phi \sin\epsilon + \cos\epsilon)dy + (\tan\phi \cos\epsilon - \sin\epsilon)dx] \quad (2-25)$$

The method of characteristics works by defining a boundary in which the unknowns of the ordinary differential equations (x, y, σ^*, ψ) are fully specified and dividing it into a predetermined number of nodes. Through these nodes, alpha and beta lines are constructed

which intersect with one another at a third point whose coordinates are given by the simultaneous solution of the characteristic equations 2-22 & 2-23.

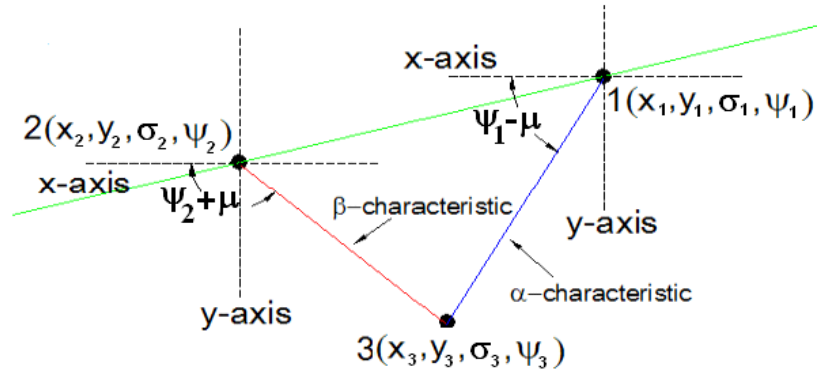


Figure 2.12. Characteristic lines

Rewriting equations 2-22 and 2-23 yields:

$$y = x \tan(\psi_1 - \mu) - x_1 \tan(\psi_1 - \mu) + y_1 \quad (2-26)$$

$$y = x \tan(\psi_2 + \mu) - x_2 \tan(\psi_2 + \mu) + y_2 \quad (2-27)$$

where x_1, y_1, ψ_1 are the values at the first node and x_2, y_2, ψ_2 are the value at the second node.

We see that the equations are linear with respect to the unknown, x, y the coordinate of the intersections, and can therefore be solved by linear techniques. Since there are only two equations, Cramer's rule was employed. The unknowns are given by

$$x = \frac{y_2 - \tan(\psi_2 + \mu) x_2 - y_1 + \tan(\psi_1 - \mu) x_1}{\det} \quad (2-28)$$

$$y = \frac{-\tan(\psi_2 + \mu) y_1 + \tan(\psi_1 - \mu) y_2}{\det} + \frac{-\tan(\psi_2 + \mu) \tan(\psi_1 - \mu) x_2 + \tan(\psi_2 + \mu) \tan(\psi_1 - \mu) x_1}{\det} \quad (2-29)$$

$$\det = \tan(\psi_1 - \mu) - \tan(\psi_2 + \mu) \quad (2-30)$$

In a similar fashion equation 2-24 and 2-25 can be rewritten as

$$\sigma^* = -(2\sigma_2^* \tan \phi) \psi + \sigma_2^* + (2\sigma_2^* \tan \phi) \psi_2 + \gamma(\tan \phi \sin \varepsilon + \cos \varepsilon)(y - y_2) + \gamma(\tan \phi \cos \varepsilon - \sin \varepsilon)(x - x_2) \quad (2-31)$$

$$\sigma^* = (2\sigma_1^* \tan \phi) \psi + \sigma_1^* - (2\sigma_1^* \tan \phi) \psi_1 - \gamma(\cos \varepsilon \tan \phi + \sin \varepsilon)(x - x_1) - \gamma(\sin \varepsilon \tan \phi - \cos \varepsilon)(y - y_1) \quad (2-32)$$

where σ_1^*, ψ_1 are the values at the first node and σ_2^*, ψ_2 are the values at the second node.

Substituting the solution x, y from equations 2-28 and 2-29 into the above expressions, yields for unknown σ^* and ψ by using Cramer's rule

$$\sigma^* = 2\sigma_2^* \tan \phi \frac{\begin{bmatrix} \sigma_1^* - (2\sigma_1^* \tan \phi) \psi_1 - \gamma(\cos \varepsilon \tan \phi + \sin \varepsilon)(x - x_1) \\ -\gamma(\sin \varepsilon \tan \phi - \cos \varepsilon)(y - y_1) \end{bmatrix}}{\det} + 2\sigma_1^* \tan \phi \frac{\begin{bmatrix} \sigma_2^* + (2\sigma_2^* \tan \phi) \psi_2 + \gamma(\tan \phi \sin \varepsilon + \cos \varepsilon)(y - y_2) \\ +\gamma(\tan \phi \cos \varepsilon - \sin \varepsilon)(x - x_2) \end{bmatrix}}{\det} \quad (2-33)$$

$$\psi = \frac{\begin{bmatrix} \sigma_2^* + (2\sigma_2^* \tan \phi) \psi_2 + \gamma(\tan \phi \sin \varepsilon + \cos \varepsilon)(y - y_2) \\ +\gamma(\tan \phi \cos \varepsilon - \sin \varepsilon)(x - x_2) \end{bmatrix}}{\det} + \frac{\begin{bmatrix} \sigma_1^* - (2\sigma_1^* \tan \phi) \psi_1 - \gamma(\cos \varepsilon \tan \phi + \sin \varepsilon)(x - x_1) \\ -\gamma(\sin \varepsilon \tan \phi - \cos \varepsilon)(y - y_1) \end{bmatrix}}{\det} \quad (2-34)$$

$$\det = 2\sigma_2^* \tan \phi + 2\sigma_1^* \tan \phi \quad (2-35)$$

Values of σ^* and ψ along the characteristics are not constant and therefore should be averaged out from node to node. Once the first iteration of equations 2-28, 2-29, 2-33 and 2-34 are complete, the following replacements are made for subsequent iterations.

$$\psi_1 = \frac{1}{2}(\psi + \psi_1) \quad (2-36)$$

$$\psi_2 = \frac{1}{2}(\psi + \psi_2) \quad (2-37)$$

$$\sigma_1^* = \frac{1}{2}(\sigma^* + \sigma_1^*) \quad (2-38)$$

$$\sigma_2^* = \frac{1}{2}(\sigma^* + \sigma_2^*) \quad (2-39)$$

Iterations persist until the difference between subsequent values of x, y, ψ, σ^* reach an acceptable percent relative error, determined from the following

$$\varepsilon_a = \frac{\text{current approximation} - \text{previous approximation}}{\text{current approximation}} * 100\% \quad (2-40)$$

For the case of a rotary shell blender the method of characteristics is initiated along the free surface since the stress state is known and fully specified. The free surface bears no loads and therefore contains no normal or shear stresses along its surface.

$$\sigma_{yy} = 0 \quad \tau_{yx} = 0 \quad (2-41)$$

Since shear does not occur along the free surface, it is a principal axis. Whether it is a major principal axis or a minor principal axis is dependent upon the lateral pressures that reside.

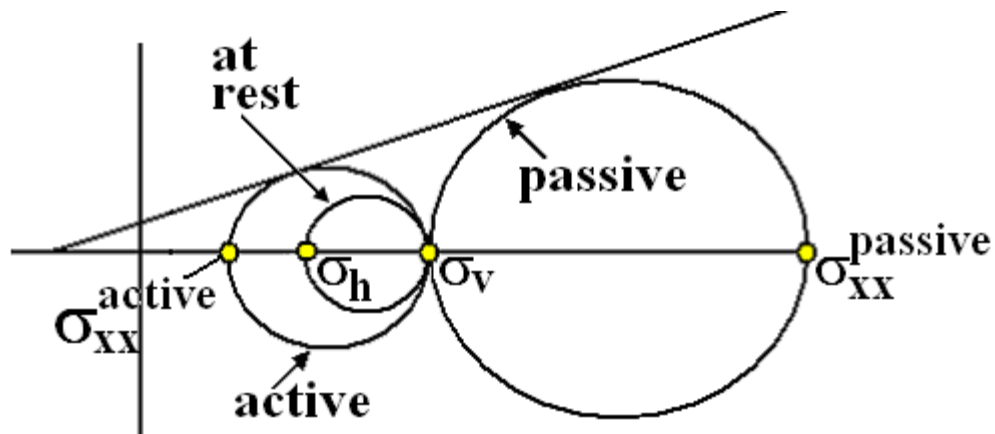


Figure 2-13. Active and passive Mohr circle

Take, for example, a case where the stresses are known along the vertical axis, represented by the point σ_v in the Mohr circle diagram in figure 2-13, and the shear stresses are zero so that the

point resides along the normal axis of the Mohr circle. The stresses along the adjacent axis, σ_k , must lie either to the left or the right of σ_v .

If point σ_h lies to the left of point σ_v a Mohr circle may be constructed that passes through both points and touches the internal yield locus. This is referred to as the active state and represents a permissible state of stress of the material. Likewise, a Mohr circle may be constructed that represents the passive state of stress of the material, when the point σ_h lies to the right of σ_v . In fluids there is a one-to-one ratio between vertical and horizontal stresses. As a stress is applied, particles that are in continuous motion within the fluid, are distributing the stresses equally in all directions. On the other hand, granular materials, which are orders of magnitude less abundant in numbers than are fluids, are not in constant motion and can therefore support a portion of the load above and distribute a fraction of the load horizontally. As a result, the horizontal stress of a granular material is less than that of its vertical stress when confined and exposed to no stresses other than those induced from the material itself. The constant K , the coefficient of earth pressure, is the ratio of the horizontal and vertical stresses for a granular material.

$$k = \frac{\sigma_h}{\sigma_v} \quad (2-42)$$

With no shear stress along the free surface and the material in the drum being in the active state, with larger vertical stresses than horizontal stresses, choosing a coordinate system with the y-axis perpendicular to the free surface, σ_{yy} , is equivalent to the major principal stress.

$$\sigma_{yy} = \sigma^* (1 - \sin \phi \cos 2\psi) - c \cot \phi = 0 \quad (2-43)$$

By choosing the coordinate system in such a way that the x-axis is aligned with the free surface and the major principal stress direction points perpendicularly downward from the free surface

ψ , the angle measured from the x-axis to the major principal stress direction is equal to ninety degrees. Substituting ψ into equation 2-43 with a value of ninety degrees yields the mean stress along the free surface. Recall that cohesion did not come into play with the differential equations earlier, but is introduced to the system now in equation 2-44.

$$\sigma^* = \frac{c \cot \phi}{1 - \sin \phi} \quad (2-44)$$

Any location within the mesh of nodes that comes into contacts with the perimeter of the drum will not be assessed in the same manner as the other nodes. Granular material can slip along boundaries just as readily as it forms and slips along internal slip planes. The criteria for the formation of slip planes along boundary are similar to those formed within the bulk. The wall yield locus is linear and is expressed as follows:

$$\tau_w = \mu_w \sigma_w + c_w \quad (2-45)$$

where μ_w is the coefficient of wall friction and c_w is the adhesion between the material in the drum and the inner lining of the drum. Unlike the internal yield locus that runs tangential to the Mohr circle making contact with it in only one location, the wall yield locus runs straight

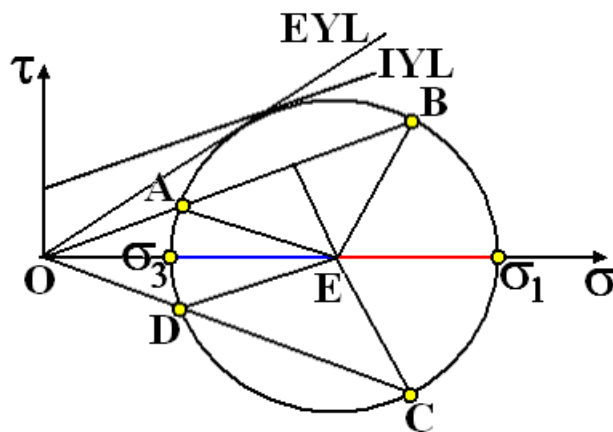


Figure 2-14. Wall angles

through the Mohr circle contacting it in two locations (see figure 2-14), four if you count the wall yield locus incline at a negative angle from the normal stress plane.

The four locations A, B, C and D in which the wall yield locus intersects the Mohr circle are the four possible stress states that exist at the wall. Points A and D correspond to active states in which the vertical stresses are greater than the horizontal stresses. Point A, above the normal stress axis, corresponds to an active state with positive shear along the wall, while point D corresponds to an active state with negative shear along the wall. Points B and C fall further to the right of the Mohr circle, and correspond to the passive state in which the vertical stresses are less than the horizontal stresses. Point B corresponds to points on the wall that are in a passive state with positive shear along the wall, while point C corresponds to a passive state with negative shear along the wall. The angle for the active state with negative shear at the wall is depicted in both Mohr and real space in figure 2.15.

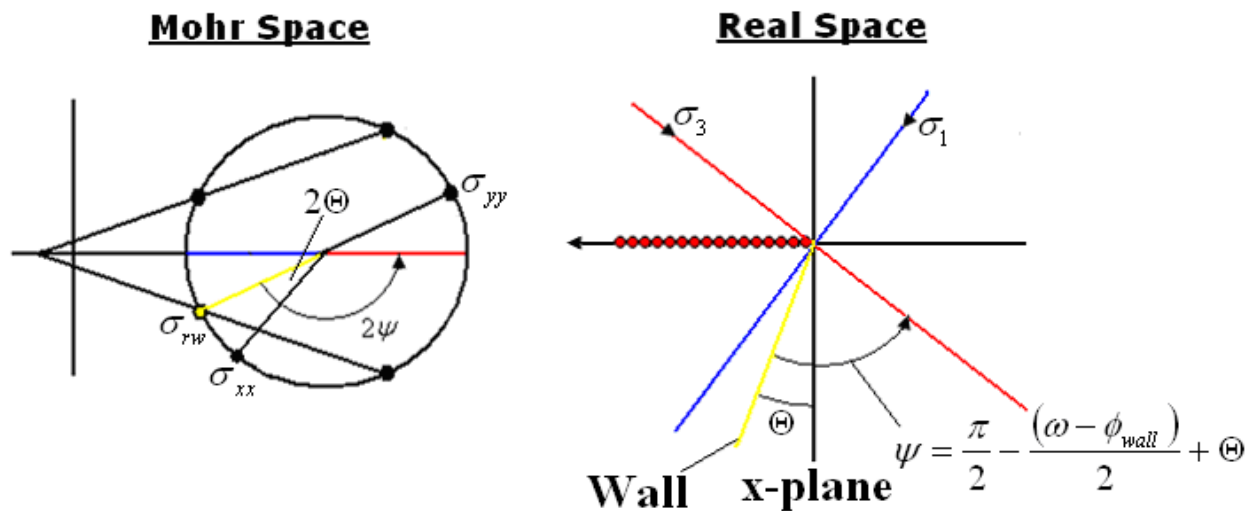


Figure 2-15. Wall angles

Values of ψ for the active states A and D are given by

$$\psi = \frac{\pi}{2} + \frac{(\omega - \phi_{wall})}{2} + \Theta \quad (2-46)$$

$$\psi = \frac{\pi}{2} - \frac{(\omega - \phi_{wall})}{2} + \Theta \quad (2-47)$$

while values of ψ for the passive states B and C are given by

$$\psi = \pi - \frac{(\omega + \phi_{wall})}{2} + \Theta \quad (2-48)$$

$$\psi = \frac{(\omega + \phi_{wall})}{2} + \Theta \quad (2-49)$$

Θ is the inclination that the boundary makes from the x-axis, ϕ_{wall} is the incline of the wall yield locus, and ω is the angle formed in Mohr circle from wall yield locus (see figure 2-15 & 2-16).

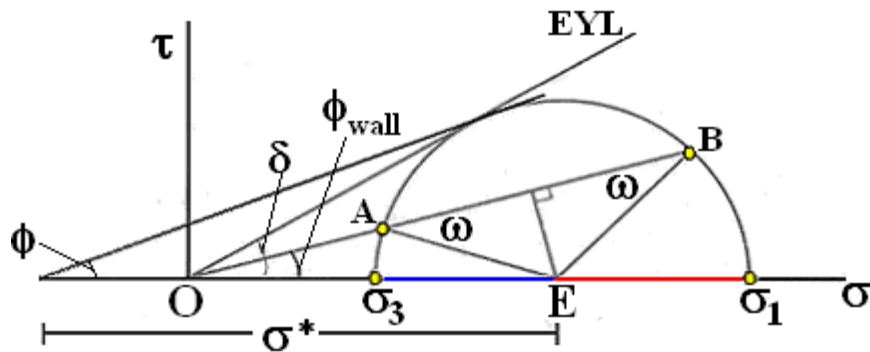


Figure 2-16. Wall angles

Velocity Within Plastic Region for Method of Characteristic Model

Just as the shape and size of the plastic region plays an important role in the blending process, accurate prediction of the velocity profile is vital. Knowledge of the velocity profile within the plastic region enables us to determine the resident time distribution of the blender which is the foundation of which our model is based. Ascertaining the velocity profile however is no trivial task. The main difficulty lies in the formulation of a flow rule. The flow rule

provides the relationship necessary to acquire a constitutive equation that enables us to predict the velocity distribution within the granular material as a function of material properties. Unlike fluids which have a direct relationship linking its velocity to stress through its viscosity, its ability to resist shear while in motion, no such link exist for bulk solids which are able to resist shear well before motion is even initiated.

A number of flow rules have been proposed, but the two primary flow rules used most frequently are an associated flow rule which applies the *Principal of Normality* and a non-associated flow rule that uses the *Principal of Coaxiality*. The term associated simply infers to the fact that the plastic strains are associated directly with the yield surface. The associated flow rule is shown in equation 2-50 where the strain rates $\dot{\epsilon}_{ij}$ in any arbitrary direction are proportional to the derivatives of the yield function with respect to the corresponding stress.

$$\dot{\epsilon}_{ij} = \lambda \frac{\partial Y}{\partial \sigma_{ij}} \quad (2-50)$$

The principle requirement of the above associated flow rule is the satisfaction of the normality condition which states that the strain rate vector is normal to the yield locus. During steady state however the stresses imposed on a bulk solid are described by the end of the yield locus which many believe does not conform to the normality conditions. With genuine uncertainty lingering we were hesitant to employ the associated flow rule and opted for the non-associated flow rule that is not so dubious.

Being that we are dealing with granular material, material that when poured into a vessel would not likely configure themselves in an organized crystalline structure and therefore would possess isotropic tendencies, that is the tendency of having the same mechanical properties in all

directions a viable option would be to employ a non-associated flow rule that uses the *principle of coaxiality*. The *principle of coaxiality* states that the axes of principle strain rate coincides with the axes of principle stress. If the material is in fact isotropic and if the plastic strain rate depends only on the stress then the *principle of coaxiality* is no longer an assumption but is in fact required by the rules of linear algebra [31].

The *principle of coaxiality* can be best conveyed through the illustrations in figure 2-17 and 2-18. The diagram on the left is a depiction of the stresses imposed on a two-dimensional infinitesimal element while under shear. The diagram on the right is of the Mohr's circles for stress and strain rate superimpose on one another. Figure 2-17 is for non-associated flow rules while figure 2-18 is for associated flow rules. The angles ψ and θ are the angles that x-axis makes with the major principle stress and major principle strain rate direction. Recall that all angles represented in Mohr space are twice as large as those in real space. For cases where the principle of coaxiality apply we expect the infinitesimal element to deform in such a way that the angle of deformation, θ is equivalent to ψ .

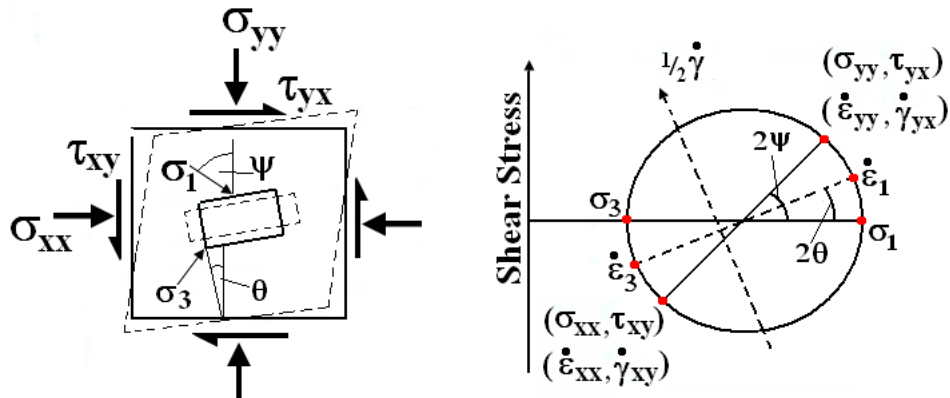


Figure 2-17. Non-associative Case

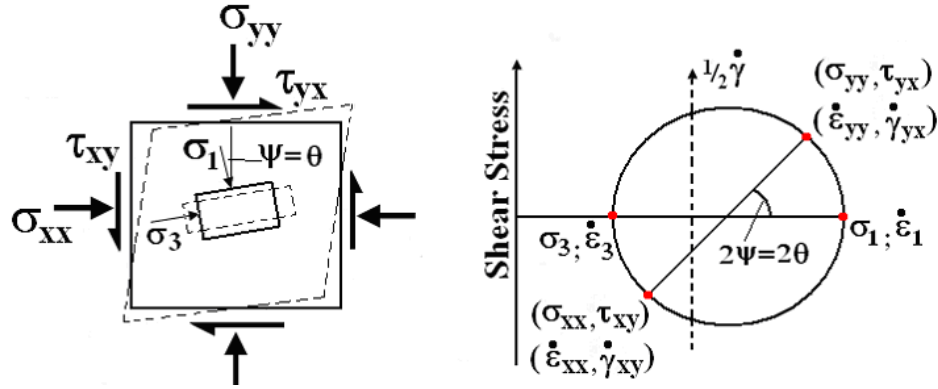


Figure 2-18. Associative case

In figure 2-17 the axes of principle strain rate clearly does not coincide with the axes of principle stress thereby possessing ψ and θ angles that differ. In figure 2-18 the axes coincide resulting in equivalent ψ and θ angles. From the stress Mohr's circle one is able to derive the following stress components shown in equation 2-51, 2-52 and 2-53 where σ^* is the mean stress measured from the center of the Mohr's circle to the intercept of the internal yield locus with the abscissa and R is the radius of the Mohr's circle.

$$\sigma_{xx} = \sigma^* - R \cos 2\psi \quad (2-51)$$

$$\sigma_{yy} = \sigma^* + R \cos 2\psi \quad (2-52)$$

$$\tau_{yx} = -\tau_{xy} = R \sin 2\psi \quad (2-53)$$

In a similar fashion the strain rates shown in equation 2-54, 2-55 and 2-56 are derived from the strain rate Mohr's circle where e^* is the mean strain rate measured from the center of the Mohr's circle to its origin and R' is the radius of the Mohr's circle.

$$\dot{\epsilon}_{xx} = e^* - R' \cos 2\theta \quad (2-54)$$

$$\dot{\epsilon}_{yy} = e^* + R' \cos 2\theta \quad (2-55)$$

$$\frac{1}{2} \dot{\gamma}_{yx} = R' \sin 2\theta \quad (2-56)$$

For the case of coaxiality 2θ in equations 2-54 through 2-56 can be replaced with 2ψ . From physical inspection of the stress and strain rate Mohr's circles $\tan(2\psi)$ can then be solved for in terms of both stress and strain rate enabling the *principle of coaxiality* to be expressed in algebraic form as follows.

$$\frac{\tau_{xy}}{\frac{1}{2}(\sigma_{xx} - \sigma_{yy})} = \tan(2\psi) = \frac{\frac{1}{2}\dot{\gamma}_{xy}}{\frac{1}{2}(\dot{\epsilon}_{xx} - \dot{\epsilon}_{yy})} \quad (2-57)$$

The strain rates in equation 2-57 can be readily substituted with their velocity gradient equivalents to give the following partial differential equation with the unknown velocities u and v with respect to the coordinates x and y

$$\left(\frac{\partial u}{\partial x} - \frac{\partial v}{\partial y} \right) \tan 2\psi = \frac{\partial u}{\partial y} + \frac{\partial v}{\partial x} \quad (2-58)$$

With the assumption of incompressibility $\frac{\partial u}{\partial x}$ can be eliminated from the above equation to give

$$\frac{\partial u}{\partial y} = -\frac{\partial v}{\partial x} - 2\frac{\partial v}{\partial y} \tan 2\psi \quad (2-59)$$

Similar to the way the stress equations were solved in the previous section to determine the shape and size of the plastic region, the velocities of equation 2-59 can likewise be solved by the method of characteristics. Recall that the method of characteristics works by utilizing the fact that along certain curves, called characteristics, first and second order partial differential equations reduce to ordinary differential equations.

By defining an arbitrary angle ζ which is measured counter clockwise from the x -axis to the characteristic direction (see figure 2-19), the total derivative of the unknowns u and v can be expressed with respect to s , the distance along the characteristics.

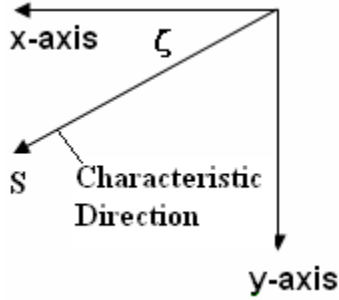


Figure 2-19. Characteristic direction for velocity

$$\frac{du}{ds} = \left(\frac{\partial u}{\partial x}\right)\left(\frac{\partial x}{\partial s}\right) + \left(\frac{\partial u}{\partial y}\right)\left(\frac{\partial y}{\partial s}\right) = \frac{\partial u}{\partial x} \cos \zeta + \frac{\partial u}{\partial y} \sin \zeta \quad (2-60)$$

$$\frac{dv}{ds} = \left(\frac{\partial v}{\partial x}\right)\left(\frac{\partial x}{\partial s}\right) + \left(\frac{\partial v}{\partial y}\right)\left(\frac{\partial y}{\partial s}\right) = \frac{\partial v}{\partial x} \cos \zeta + \frac{\partial v}{\partial y} \sin \zeta \quad (2-61)$$

By combining equation 2-59 with the total derivatives of equation 2-60 and 2-61 we obtain a partial differential equation that reduces to an ordinary differential equation along two directions referred to as the alpha and beta directions. The first direction, the alpha direction, occurs at an angle of $\zeta = \psi - 45^\circ$ while the beta direction occurs at $\zeta = \psi + 45^\circ$. The curves that align themselves at these angles are referred to as the alpha and beta characteristics and are described by equations 2-62 and 2-63.

$$\frac{dy}{dx} = \tan(\psi - 45^\circ) \quad (2-62)$$

$$\frac{dy}{dx} = \tan(\psi + 45^\circ) \quad (2-63)$$

Equations 2-64 and 2-65 are the ordinary differential equations that results along these directions.

$$\frac{du}{ds} + \frac{dv}{ds} \tan(\psi - 45^\circ) = 0 \quad (2-64)$$

$$\frac{du}{ds} + \frac{dv}{ds} \tan(\psi + 45^\circ) = 0 \quad (2-65)$$

Analogous to the formation of the stress mesh from the solution of the stress equations of the previous section, a velocity mesh can be generated in a similar fashion within the plastic region. The mesh is composed of intercrossing alpha and beta characteristic lines, described by equations 2-62 and 2-63 that form nodes at the intersections of these lines in which physical properties of the bulk can be gathered to determine its velocity at that particular node. Similar to the stress mesh, indicated by green lines in figure 2-20, the velocity mesh, designated by red lines, originates at the free surface and slowly extend down into the bulk until merging with the plastic-elastic interface. The angles at which these lines emerge from the nodes do not coincide. The stress characteristics are inclined at angles of $\psi \pm \varepsilon$ from the x-axis while the velocity characteristics are inclined at angles of $\psi \pm 45^\circ$ from the x-axis. The difference in the angles between the two sets of characteristic directions has to do with their position on the Mohr circle. The Mohr circle is a representation of the state of stress of granular material. Its intersection with the yield locus describes the stress state upon incipient failure along the slip plane. The angle this point makes with the minor principal plane is 2ε (see figure 2-10). Once flow is initiated the state of stress of the material is altered. During flow particles are constantly reconfigured, forming and breaking bonds continually. The stress state of the material can no longer be described by its intersection with the yield locus. During steady flow the stress state lies at the top of the Mohr circle. A stress state at the top of the Mohr circle forms an angle of 90 degrees with the minor principal plane. In real space the angles are half of those in Mohr space, hence how we arrive at angles of $\pm \varepsilon$ for the stress characteristics and angles of $\pm 45^\circ$ for the velocity characteristics. Being that epsilon, given by equation 2-66, is always less than 45° the characteristic lines of the velocity mesh will always be steeper than those of the stresses.

$$\varepsilon = 45^\circ - \frac{\phi}{2} \tag{2-66}$$

While the stress mesh is shown in its entirety in figure 2-20 only the first row of nodes from the velocity mesh are shown in the figure to avoid confusion.

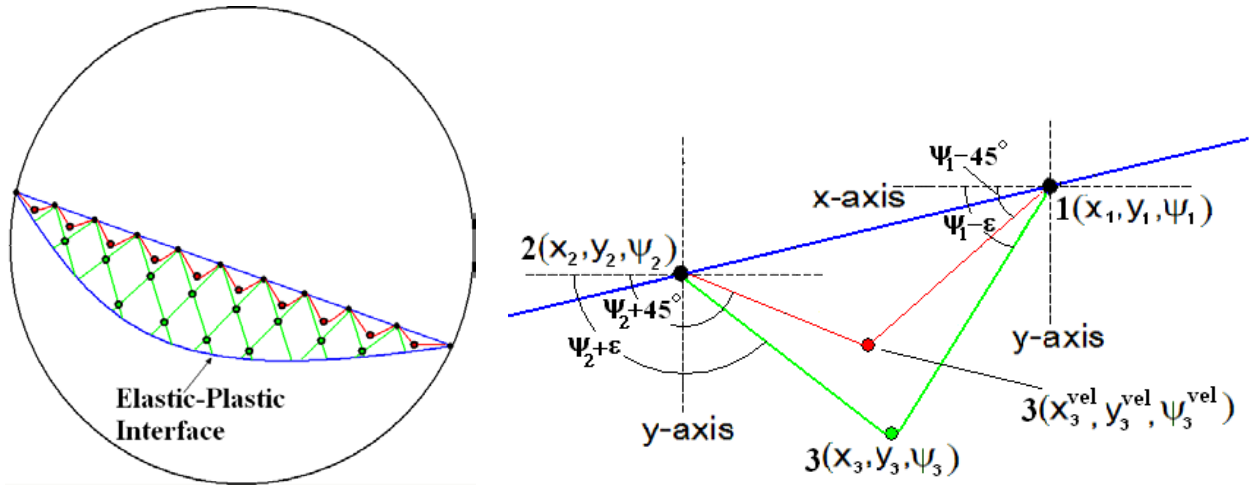


Figure 2-20. Stress and velocity mesh

The diagram on the right in figure 2-20 is a depiction of a single crossing of characteristic lines for both stress and velocity meshes that originate from two adjacent nodes labeled 1 and 2 that intersect to form a third. The positions of the third nodes is determined from the simultaneous solution of the characteristic equations, written in finite difference form in equations 2-67 and 2-68 where the subscripts 1 and 2 denote the two adjacent nodes in which the characteristic lines alpha and beta originate.

$$y - y_1 = (x - x_1) \tan(\bar{\psi}_1 - 45^\circ) \quad (2-67)$$

$$y - y_2 = (x - x_2) \tan(\bar{\psi}_2 + 45^\circ) \quad (2-68)$$

Once again Cramer's rule can be applied to evaluate the above expressions since the equations are linear with respect to their unknowns x and y. However, prior to solving these expressions ψ must be known as a function of position. Since ψ varies with position $\bar{\psi}_1$ and $\bar{\psi}_2$ are the average ψ value that the two adjacent nodes make with the ψ value of the unknown third node.

Since the ψ value at the unknown node (x,y) can not possibly be known prior to performing the

calculation an iterative procedure is required in which ψ at the unknown node (x,y) is progressively updated with every iteration until an acceptable level of tolerance is obtained. However, prior to executing these iterations an approximation or initial guess is required for $\bar{\psi}_1$ and $\bar{\psi}_2$. Provided that a significant number of nodes are used the mesh should be tight enough that $\bar{\psi}_1 = \psi_1$ and $\bar{\psi}_2 = \psi_2$ serve as an accurate initial guess.

Upon completion of the first iteration the actual value of ψ at the current calculated coordinate of the third node can be obtained by referencing the stress mesh. Through the previous calculations of the stress equations the precise values of ψ 's are known at the various nodes that comprise the stress mesh. Unfortunately other than the initial row of nodes along the free surface the nodes of the velocity mesh do not align themselves with those of the stress mesh. Refer back to figure 2-20. However, the ψ value for those nodes that do not correspond with known values are determined by interpolation.

A least square approach was used in which coefficients were fitted to the known ψ values at the various nodes of the stress mesh. The technique works by selecting coefficients that minimize the sum of the squares of the residual between the actual ψ values at the nodes to those calculated from the model. The least square approach is shown in algebraic form in equation 2-69 where the actual ψ values taken from the nodes of the stress mesh are labeled as $\psi_{i,reference}$ and those calculated from the model as $\psi_{i,model}$.

$$\sum_{i=1}^n e_i^2 = \sum_{i=1}^n (\psi_{i,reference} - \psi_{i,model})^2 \quad (2-69)$$

A multiple linear model was proposed in which ψ varies linearly with both x and y coordinates. Although ψ in reality does not vary linearly with either x nor y a linear model of the form

expressed in equation 2-70 is employed. Given that the position of the third node will not deviate significantly from the proximity of the nodes of the stress mesh the error within the model should bear little affect on the outcome.

$$\psi_{i,model} = a_0 + a_1 x_{i,reference} + a_2 y_{i,reference} \quad (2-70)$$

Selection of the coefficients which will produce the best results is attained by combining equations 2-69 and 2-70 and differentiating it with respect to each of the three unknown coefficients a_0 , a_1 and a_2 .

$$\frac{\partial Sr}{\partial a_0} = -2 \sum (\psi_{i,reference} - a_0 - a_1 x_{i,reference} - a_2 y_{i,reference}) \quad (2-71)$$

$$\frac{\partial Sr}{\partial a_1} = -2 \sum x_{i,reference} (\psi_{i,reference} - a_0 - a_1 x_{i,reference} - a_2 y_{i,reference}) \quad (2-72)$$

$$\frac{\partial Sr}{\partial a_2} = -2 \sum y_{i,ref} (\psi_{i,reference} - a_0 - a_1 x_{i,reference} - a_2 y_{i,reference}) \quad (2-73)$$

The combination of coefficients that yields the minimum sum of the squares is obtained by setting the partial derivatives of equations 2-71 through 2-73 equal to zero. These coefficients can be seen in matrix form in equation 2-74 where n is the number of reference points

$$\begin{bmatrix} n & \sum x_{i,reference} & \sum y_{i,reference} \\ \sum x_{i,reference} & \sum x_{i,reference}^2 & \sum x_{i,reference} y_{i,reference} \\ \sum y_{i,reference} & \sum x_{i,reference} y_{i,reference} & \sum x_{i,reference}^2 \end{bmatrix} \begin{bmatrix} a_0 \\ a_1 \\ a_2 \end{bmatrix} = \begin{bmatrix} \sum \psi_{i,reference} \\ \sum x_{i,reference} \psi_{i,reference} \\ \sum y_{i,reference} \psi_{i,reference} \end{bmatrix} \quad (2-74)$$

The reference points in the above equations are defined immediately after an iteration in which the coordinate of the third node is determined. The three closest nodes in proximity to the calculated third node are selected from the multiple number of nodes that comprise the stress mesh. This procedure is repeated for every iteration until the (x,y) coordinate of the third node is located that is within the specified tolerance limits.

Upon establishment of the position of the third node attention is then focus on determining its velocity. This is done by the simultaneous solution of the ordinary differential equations of equation of 2-64 and 2-65 which are shown in finite difference form below.

$$u - u_1 + (v - v_1) \tan(\bar{\psi}_1 - 45^\circ) = 0 \quad (2-75)$$

$$u - u_2 + (v - v_2) \tan(\bar{\psi}_2 + 45^\circ) = 0 \quad (2-76)$$

Similar to the characteristic equations that were linear with respect to their unknowns so are equation 2-75 and 2-76 allowing for Cramer's rule to be applied once more in their solution. However, unlike the characteristic equations no iterations are required since $\bar{\psi}_1$ and $\bar{\psi}_2$ have already been established.

The velocity distribution predicted through these equations are fundamentally dependent upon the initially velocities specified along the free surface. A series of velocity nodes are evenly spaced throughout the free surface in which the velocity, v , in the y-direction perpendicular to the free surface are set to zero while the velocity, u , in the x-direction parallel with the free surface are assumed to gradually decrease as we make our way down the pile with the maximum velocity, u_o , occurring at the top of the pile. The velocity at the free surface is given by equation 2-77 where N is the total number of nodes along the free surface.

$$u_n = u_o \left(\frac{N - 1 - n}{N - 1} \right) \quad (2-77)$$

The velocity of the particles in the x-direction is assumed to decrease as the particles makes their way down the free surface as a result of particle-particle friction. Mindful that the particles' velocity at the bottom of the pile is zero the velocity parallel to the free surface was assume to decrease evenly throughout the nodes.

Slope Stability

For the parabolic model we see from equation 2-2 that the thickness of the plastic region is inversely proportional to $\sin(\varepsilon)$, where ε , is the incline of the free surface from the horizontal, resulting in a thinner plastic region with increasing ε . Although it can not be seen explicitly through its equations, we also attain thinner plastic region with larger ε values for the method of characteristic model. The same method is used to determine the inclination of the free surface for both models. Initially, a low value is chosen for ε , well below the angle of repose, so that the free surface is effectively flat and parallel with the horizontal. ε is slowly increased until the point of instability, at which point the free surface and the elastic-plastic interface are fixed in their present position. The point of instability is determined by using the *ordinary method of slices* [7].

This method entails dividing the body of the assumed failure zone into vertical slices and applying a force balance to the slices individually (see figure 2-21). The widths of the slices are arbitrarily chosen and are not required to be of equal length. The base of each slice is approximated by a straight line, an approximation that is valid provided the assumed failure region is divided into a sufficient number of thin slices. Resolving forces perpendicular and tangential to the base of each slice, the normal and shear force along the base are defined as:

$$N = W \cos \alpha_1 \quad (2-78)$$

$$S = W \sin \alpha_1 \quad (2-79)$$

Where W is the weight of the slice and α_1 is the inclination of the base of the slice with the horizontal. Computing the static equilibrium of avalanching bodies, regardless which method is used is statically indeterminate, there are simply more unknowns (forces, location of forces, factor of safety, etc.) than equilibrium equations. Different methods require different

assumptions in order to balance the number of unknowns with the number of equations. What to do with the forces along the sides of the slices is a concern for all methods. The *ordinary method of slices* neglects these forces altogether. Provided that the slices are sufficiently thin, forces along the sides are assumed to be equal and opposite, canceling one another.

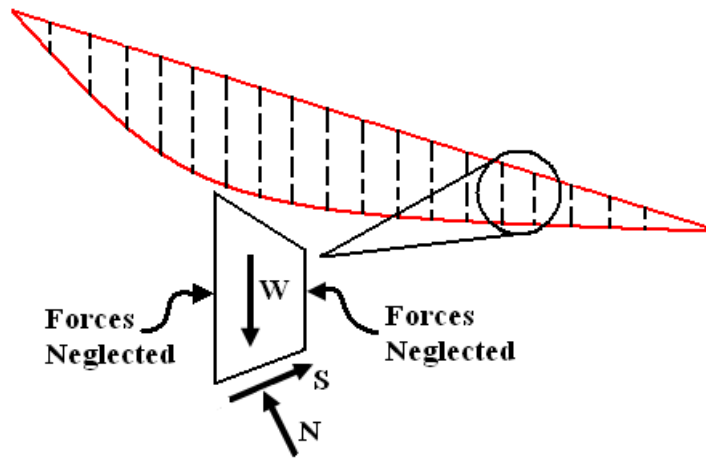


Figure 2-21. Ordinary method of slices

The material will fail if the forces imposed on the material are greater than those of the resisting forces of the material. The factor of safety, F , is used to establish precisely when this occurs. The factor of safety is defined as the ratio of the available shear strength, s , of the material to the equilibrium shear stress, τ .

$$F = \frac{s}{\tau} \quad (2-80)$$

If the factor of safety falls below a value of one, the equilibrium shear stress exceeds the material's ability to resist shear and failure ensues. The shear strength of the material is expressed in terms of the Mohr-Coulomb equation:

$$s = c + \sigma \tan(\phi) \quad (2-81)$$

In actuality the factor of safety varies along the slip surface; only during failure are the shear forces equal to the shear strength of the material, at which point the factor of safety would be a constant throughout the slip surface. Summing the forces for each slice, the factor of safety is assumed to be the same throughout. Its value represents an overall average and is given by equation 2-82

$$F = \frac{\sum c\Delta l + W \cos \alpha_1 \tan(\phi)}{\sum W \sin \alpha_1} \quad (2-82)$$

Placement of Tracers

Once the plastic and elastic regions and their velocities are defined, tracers are introduced into the system. Three sets of simulations were done. In the first set tracers were placed in the upper right hand corner of the bed in order to mimic the placement of tracers in the experimental setup (see figure 2-22). The second set of simulations were done in which the markers were mapped from images from the experiments and positioned in the simulation using a density distribution. The third and final set of simulations were done with a single vertical strip of tracer placed in the center of the drum.

For the first set of simulations, tracers are initially placed in the upper right hand corner of the bed in a rectangular area that starts at the center of the free surface and stretches a length of an to the bottom of the pile, extending into the bed a depth that constitutes a total area for the rectangle that is 5% of the total area of the material in the drum. The tracers were random distributed within this rectangular box by using a random number generator predefined in C++. The tracers are assumed to be of equal area. The total area of the rectangular area is divided by the total number of tracers to determine the area of a single tracer.

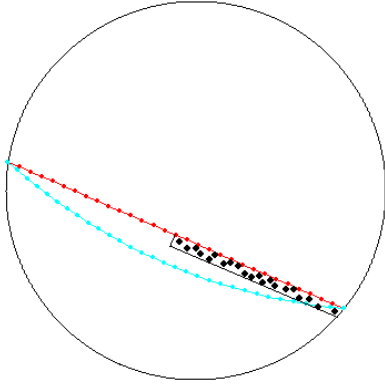


Figure 2-22. Horizontal placement of markers

The purpose of the second set of simulations was to augment the attempts of the first set, to adhere as closely as possible to all parameters of the experiments, by obtaining a more accurate starting position of the markers. Although, the markers are initially placed in the upper right hand corner of the bed they do not remain so for long. Upon initiation of rotation the markers are abruptly scattered throughout the elastic region in a complicated amorphous pattern. This pattern can be duplicated by mapping the image taken from the digital camcorder the moment the markers enter the elastic region. The markers are then randomly distributed throughout the area based on particles density.

The third set of simulations was done using single strip of tracer particles placed initially at the center of the bed, beginning a short distance from the interface of the plastic-elastic region and extending downward the entire length of the drum. The tracer particles were not spaced equally, but varied depending on the radial distance from the center of the drum. Ensuring that a tracer particle placed closer to the plastic-elastic interface is representative of the same number of particles that are placed closer to the drum's perimeter. Particles nearer to the plastic-elastic interface have a considerably shorter distance to travel before entering the plastic region than do particles near the perimeter of the drum and, therefore, would complete multiple passes before a particle at the drum's periphery would finish a single pass.

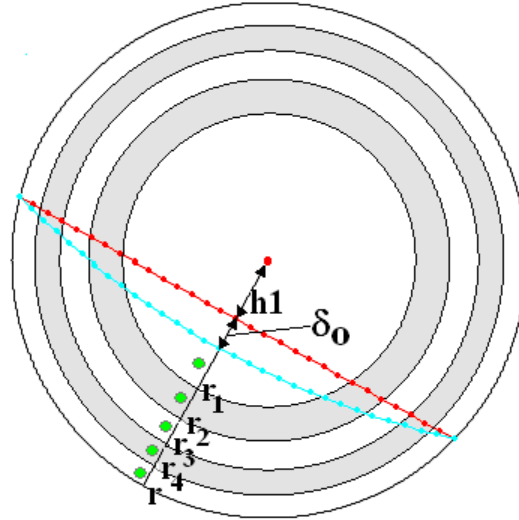


Figure 2-23. Vertical tracer placement

The drum was divided into circular rings of equal volume (see figure 2-23). The volume of each ring is expressed by equation 2-83 below where r_i 's are the outer radii of the rings, h_1 is the distance from the center of the drum to the center of the free surface, and δ_o is the thickness of plastic region at the center.

$$\left(\pi r^2 - \pi r_{\text{num_of_tracers}-1}^2\right) = \dots = \left(\pi r_{i+1}^2 - \pi r_i^2\right) = \left(\pi r_i^2 - \pi \{h_1 + \delta_o\}^2\right) \quad (2-83)$$

The above expression possesses as many unknowns as equations. Being cyclical in nature the unknowns r_i 's in the above expression can be solved for as follows

$$r_i = \sqrt{\frac{i+1}{N} \left[r^2 - (h_1 + \delta_o)^2 \right] + (h_1 + \delta_o)^2} \quad (2-84)$$

where N is the desired number of tracers. Once the outer radii of the rings are acquired, tracers are placed in the center of each ring with a slight deviation to the left of the finish line that runs from the center of the plastic-elastic interface to the edge of the drum, dividing the bed of the material into two equal halves.

Once the initial positions of the tracers have been established, tracers are incrementally allowed to move about the drum. Except for the first set of simulations, all the tracers are initially in the elastic region and travel in a circular path with a velocity of w^r . Upon entry into the plastic region the particles are no longer subjected to the rotary motion of the drum, but undergo a velocity specified by the plastic region for that particular model. The velocity experienced by a tracer particle at any particular time increment while in the plastic region is dependent on its position within the region.

Transfer Function for a Single Blending Increment

A continuous blender is one in which flows a continuous stream of material of fluctuating composition. Material enters the blender and is allowed to blend within the blender for a period of time before exiting. Particles that enter the blender at the same time are not confined to exit at the same time; each particle takes its own stochastic path. The duration of time a particle stays within the blender is its residence time. The collection of residence times of all the particles that enter and exit the blender is the residence time distribution. As the particles revolve within the blender, fluctuation in the bulk concentration are diminished before exiting the system. The variance of the concentration is used to measure the magnitude of the fluctuation, where the ratio



Figure 2.24. Continuous blender schematic

of the variance of the output stream over the variance of the input stream provides a measure of the blender's overall performance.

A continuous blender is a control system in which the input C_{in} and the output C_{out} are described by real-valued functions of time [9]. The relationship between the input function and

the output function which describe the dynamic behavior of the blending process is represented by an n^{th} -order linear or linearized non-linear ordinary differential equation that can be written in a general form as.

$$a_n \frac{d^n C_{out}(t)}{dt^n} + a_{n-1} \frac{d^{n-1} C_{out}(t)}{dt^{n-1}} + \dots + a_0 C_{out} = b_m \frac{d^m C_{in}(t)}{dt^m} + b_{m-1} \frac{d^{m-1} C_{in}(t)}{dt^{m-1}} + \dots + b_0 C_{in} \quad (2-85)$$

The coefficients of the above equation, a_i & b_i , are constant real-value numbers. The above ordinary differential equation can be reduced to a simple algebraic equation utilizing the Laplace transform.

$$C_{out}(z) = G(z)C_{in}(z) \quad (2-86)$$

Where $G(z)$ is the transfer function and is represented by the Laplace transform of the output function divided by the Laplace transform of the input function, assuming zero initial conditions [9].

$$G(z) = \frac{C_{out}(z)}{C_{in}(z)} = \frac{b_m z^m + b_{m-1} z^{m-1} + \dots + b_0}{a_n z^n + a_{n-1} z^{n-1} + \dots + a_1 z + a_0} \quad (2-87)$$

The coefficients of the polynomials of the numerator and denominator are essentially the input and output values in t space. If a unit impulse is applied to the system, the transfer function is equivalent to the output concentration in Laplace space and the transfer function in equation 2-86 can be replaced with the residence time distribution function.

$$G(z) = \frac{C_{out}(z)}{C_{in}(z)} = \frac{C_{out}(z)}{1}$$

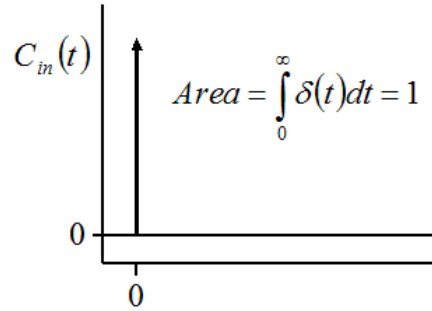


Figure 2-25. Unit impulse

Batch blenders have neither input nor output streams, but can be assessed in a similar manner. By defining a blending cycle a batch blender can be modeled as if it were a continuous blender with a recycle stream, where the output from the blender is recycled back into the blender.

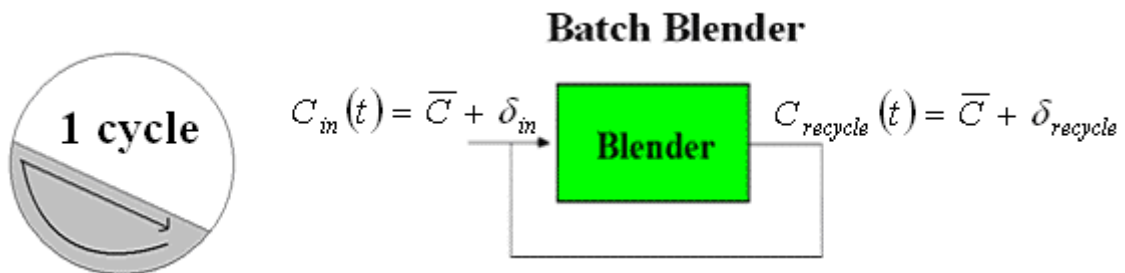


Figure 2-26. Recycle

Care must be given when defining a blending cycle. A blending cycle is defined by dividing the blending into individual blending increments. A blending increment must encompass the entire velocity profile within the blender and must include all blending mechanisms. For example for a screw blender that is made up of multiple pitches, one blending increment would constitute one pitch as it completes one full revolution. As material passes from one pitch to another pitch it experiences the same blending mechanisms. For a rotary shell blender one blending increment is one full revolution of the material and not one full revolution of the drum. The concentration within the batch blender after every cycle is given by equation 2-88.

$$C_{out}(z) = \sum_{n=1}^{\#cycles} C_{in}(z)E^n \quad (2-88)$$

Figure 2-27 is a schematic of the blending process for an idealized input after two cycles. The area under the curves represent the initial concentration of the input of a given component of a mixture. The spacing between the apexes of the peaks represents the time necessary to complete a cycle. Upon completion of every cycle the spacing between peaks diminishes as the various components of the mixture distribute through the material, widening the bases of the peaks.

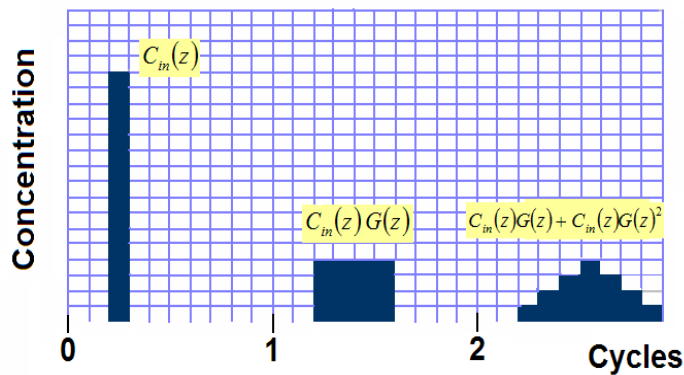


Figure 2-27. Recycle peaks

By injecting a stream of tracer particles into the blender and monitoring the time to exit from the blender, the residence time distribution is easily obtained. Since a cycle for a rotary shell blender is defined as one full revolution of the material, a line is drawn from the elastic-plastic interface

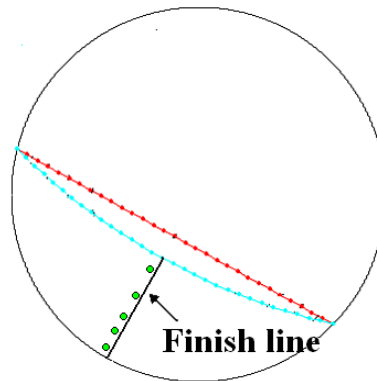


Figure 2-28. Finish line placement

that is perpendicular with the free surface that extends to the base of the drum in which the tracers are tallied each time a tracer passes.

Figure 2-28 shows the placement of the line used for tallying the tracers for all sets of simulations: As the tracers pass this finish line, which defines the hypothetical entrance and exit of tracers in a continuous blender, the volume fraction of tracers that have passed the finish line, $F(t)$, is calculated and a cumulative graph construction. The shape of the cumulative graph gives a great deal of information about the flow rates within the blender. The shape of the cumulative graph is dependent upon the time it takes tracers at various locations within the blender to flow through the blender, in other words on the residence time distribution [9].

$$F(t) = \int_0^t E(t') dt' \quad (2-89)$$

The integral of the residence time distribution function from zero to t is the fraction of tracers that took a time t or less to complete a full cycle and pass the finish line. As the tracers pass the finish line they were normalized by the total volume of the tracers so that the integral of equation 2-90 from zero to infinite is one. Once the last tracer has passed the finish line, the residence time distribution is obtained by differentiating $F(t)$ with respect to t .

$$E(t) = \frac{dF(t)}{dt} \quad (2-90)$$

Since there is a finite number of tracers that pass the finish line at various times the cumulative graph is not continuous, but is made up of discrete points. Differentiating these discrete points allows for the determination of points along the residence time distribution. In order to ensure that the residence time distribution function is continuous, values of $E(t)$ between those acquired from differentiation of the discrete cumulative points were obtained by fitting a linear line between known $E(t)$ values.

CHAPTER 3 EXPERIMENTAL

A variety of different blenders are used in industry, some are batch blenders while others are continuous blenders some utilize extremities such as paddles and ribbons while others rely solely on naturally forming shear zones to disperse the mixture. For non-cohesive or material with low to moderate cohesion values low shear blenders such as rotary shell blenders, v-blenders or double cone blenders are among the most commonly used blenders in industry. For highly cohesive materials and pastes the high shear blenders such as ribbon and paddle blenders are favored. With such a large and diverse selection of blenders to choose from we opted for the rotary shell blender for verification of our models for two primary reasons. Due to the rotary shell blenders heavy use in the pharmaceutical industry where blending is not only an important operation it's a critical one, choosing the rotary shell blender was the prudent choice. In addition its simple and symmetric geometry removes unneeded difficulties that has no bearing and sheds no insight on blending.

Experimental Procedure

A rotary shell blender was constructed out of a plastic pipe one foot in length with an inner diameter of 7.75" and outer diameter of 8.5". A plastic circular disk with the same diameter as that of the plastic pipe was secured to one end of the drum. The circular disk had a slit cut horizontally along its center dividing the circular disk into two pieces. The two pieces of the circular disk were attached to one another with a hinge allowing the top piece of the circular disk to act like a door permitting access to the interior of the drum in order to fill the drum with material. The other end of the plastic pipe was covered with a single piece of transparent plexiglas allowing for optical measurement to be made. The inner walls of the drum were lined

with coarse sand paper to provide additional friction to prevent slipping of material along the wall.

The drum is a third filled with a binary mixture of identical black and white sand with a mean particle size of 623.3 microns. The black sand, constituting 5% by weight of the total mixture, was placed in the upper right hand corner of the bulk, starting at the center extending to the periphery for the entire length of the drum. Refer to figure 3-1. Four sets of experiments were performed at various cohesion levels. In order to vary the particles cohesion regular 3-in-1 lubricating oil was applied to the sand. To ensure that the particles were uniformly coated the sand along with the 3-in-1 lubricating oil was mixed with a traditional household mixer. Mixtures were prepared with no oil, 0.10% wt. oil, 0.15% wt. oil and 0.27% wt. oil. Once filled the drum was carefully placed on rollers as can be seen in figure 3-1.

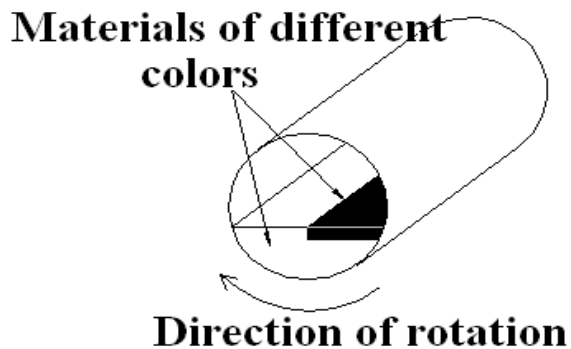
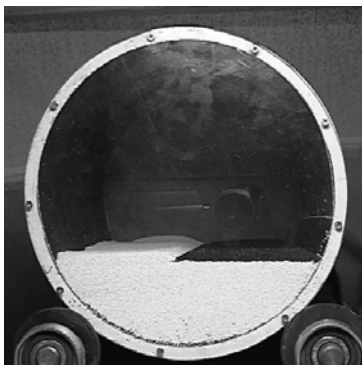


Figure 3-1. Placement of markers

Directly in front of the transparent plexiglas side of the drum a digital camcorder, with resolution of 720 X 480, was placed to capture images of the mixture within the drum as it rotates. The camcorder only focused on the lower right corner of the drum in order to improve resolution, doing so provide approximately 12 pixels per particle. A tarp is placed over the entire experimental setup in order to prevent any fluctuation in ambient light condition to interfere with the experiments. The rollers upon which the drum sits are turned on at a fairly low speed

producing a rotational speed of 4.6 RPM for the drum. The rotational speed was kept constant and did not vary from experiment to experiment.

Analyzing Procedure

After allowing the rotary shell blender to rotate for a period of time sufficient to produce a homogeneous mixture the video clip (avi format) is analyzed using Matlab. The avi file is broken up into individual frames, 30 of which occur in a second, and analyzed separately. The frames are then converted to an image made up of 345,600 pixels. The color of each pixel can be characterized by a RGB value. All colors can be described by the three primary base colors red, green and blue which when in the appropriate proportions can form any color. The RGB value of a color is actually a three element vector containing three threshold numbers which specify the intensities of the amount of red, green and blue components that compose the color. The intensity of the primary colors range in threshold value from 0 to 255. A RGB value of [0, 0, 0] would correspond to pure black while a RGB value of [255, 255, 255] corresponds to pure white.

Since neither the black nor white sand are pure in color, but possess a distribution of threshold value an image was taken of the black and white sand and the number of pixels corresponding to a given threshold value was plotted versus threshold value to determine the threshold range that corresponds to the black particles to those of the white particles. Refer to figure 3-2. From figure 3-2 we see that the black particles have threshold values, for all three RGB components, ranging from approximately 10 to 55 whereas the white particles have threshold values ranging from approximately 120 to 240. Black and white sand were chosen for the primary reason that they lie on opposite ends of the spectrum, ensuring no overlapping of the two peaks.

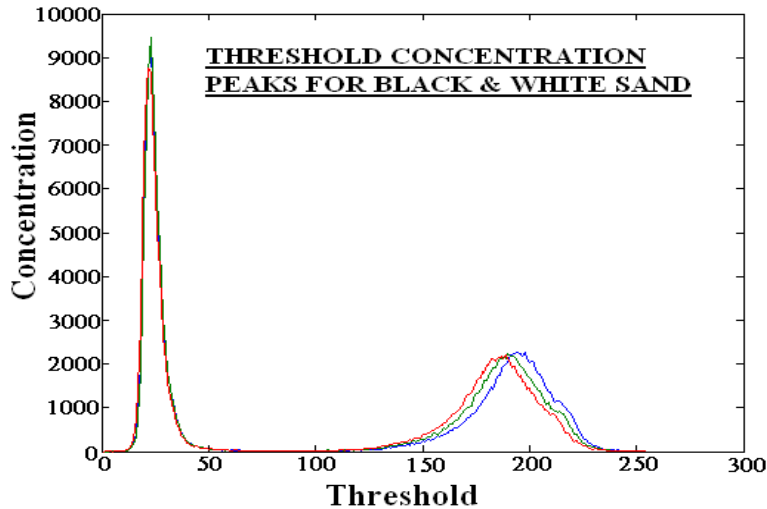


Figure 3-2. Threshold peaks of black & white particles

Since our primary objective is to be able to distinguish the black particles from the white particles there is no need for RGB thresholding which requires 3 threshold components and describes the full spectrum of colors within the particles. By converting the image to grayscale by eliminating the hue and saturation information while retaining the luminance we simplify matters by only having one threshold value ranging from 0 to 255 that measure varying degrees of black and white.

From the images the concentration of the black particles are measured not for the entire section of the drum displayed in the image, but only a small section, shown in red in the schematic of the drum in figure 3-3. Initially the free surface starts horizontal and slowly begins to rotate until the point of instability at which point the material fails and an avalanche is formed. The inclination of the free surface fluctuates from avalanche to avalanche, but for all practical purposes reaches a state of quasi-equilibrium in which point the inclination of the free surface from the horizontal is relatively constant. From this quasi-equilibrium point the analyzing window is drawn that runs parallel and slightly below the free surface to avoid the fast moving

particles in the plastic region that appear as a blur due to the camcorder's inability to capture objects traveling at high speeds.

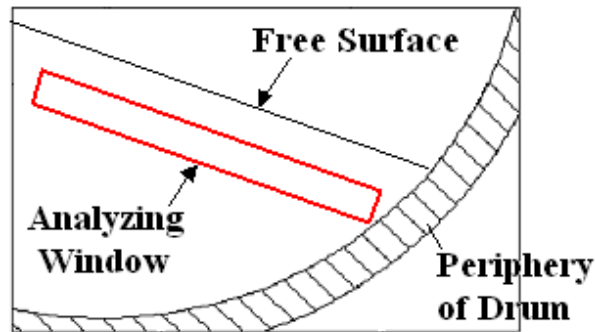


Figure 3-3. Analyzing window

The concentration within the analyzing window is then determined not by counting markers (black particles), but by counting the number of pixels that fall within a given threshold value. All pixels in the image that lie within the analyzing window with a threshold value of 70 or less were counted as black and all pixels greater than 70 were counted as white. Knowing the dimension of the analyzing window the number of pixels contained within it can be easily ascertained. Dividing the number of black pixels by the total number of pixels in the analyzing window the concentration is determined. As stated earlier a pixel does not represent a particle, approximately 12 pixels are used to compose a particle. It's inevitable that not all of the particles will lie entire within the boundary of the analyzing window that a portion will fall outside. The area of the analyzing window is large enough to dissipate any erroneous counting of pixels which might occur due to a particle partially appearing inside the analyzing window.

Although the camcorder is incapable of peering beyond the first layer of particles directly behind the plexiglas it is assumed that the blending that occurs in the front layer behind the plexiglas is representative of all the other layers. Since our particles only differ in color there is little danger of segregation ensuing, however if the mixture were compose of particles of varying

properties that were to cause segregation the most likely segregation pattern would be radially and not axially. Axial segregation in rotary shell blenders do occur however only after prolonged periods of rotation. All experiments performed achieved a homogeneous mixture in a short period of time, well before axial segregation would be a concern. Since our particles are the same in all aspects except color and homogeneous mixture was achieved in a short period of time we are comfortable that the concentration within the analyzing window is representative of the entire drum.

Schulze Measurements

Experiments were performed for mixtures that had been covered in varying amounts of lubricating oil. In order to give quantifiable meaning to the mixtures the strengths were determined using a Schulze cell. A Schulze cell is a ring shear tester that was developed to measure flow properties of bulk solids. Ring shear testers have been used in soil mechanics since the 1930's. The concept was then borrowed and modified by powder technologists to be used on bulk solids which typically possess lower stress levels than that of soil. Shear testers work by measuring the yield limits, also known as a yield locus, of a consolidated bulk solid. A diagram of a Schulze cell is shown in figure 3-4.

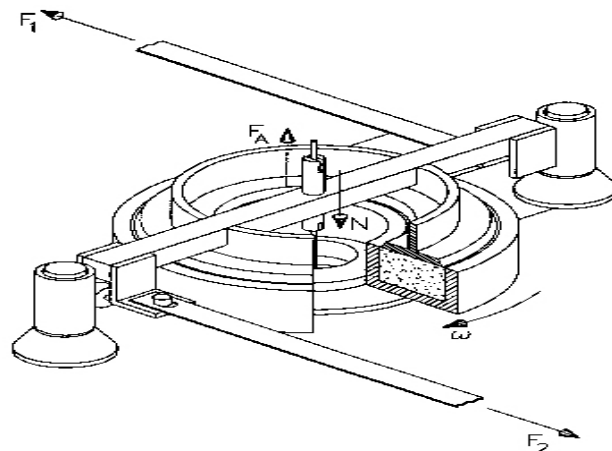


Figure 3-4. Cross-sectional schematic of the Schulze shear cell

The bulk solid is placed in the annular shape bottom ring of the shear cell. A lid is placed on top of the bulk solid and fixed in position through two tie-rods unable to rotate. A normal force is applied to the bulk solid through a load which is hung perpendicular to the lid. The bottom ring slowly rotates while the lid remains immobile exerting a shear force within the bulk. Initially the shear stress will continue to increase as show to the left of figure 3-5 and eventually reaches a steady state in which its porosity remains constant.

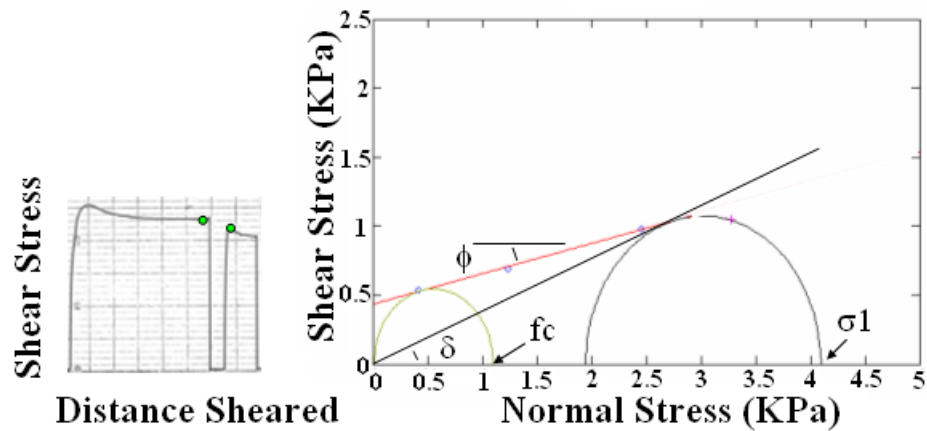


Figure 3-5. Yield locus

This step is known as the pre-shear and establishes the history, if you will, of the bulk solid tested. This point is identified on the consolidation Mohr circle shown on figure 3-5. Points along the yield locus are then determined by reducing the load to one less than that of the consolidation load and failing the sample. After failing the sample at a lighter load the consolidation load must once again be placed upon the sample and sheared in order to return the sample to the same consolidation state. A second point along the yield locus is obtained by once again choosing a load less than the consolidation less, but different from the load previously chosen and failing the sample. This procedure is repeated several more time at various loads to generate an accurate yield locus.

The cohesion of the bulk solid is determined from the intersection of the yield locus with the y-axis from plots generated with the shear stress required to initiate failure within the bulk plotted versus the normal stress imposed upon it. Once the cohesion is attained the unconfined yield strength, f_c is easily calculated via equation 3-2

$$f_c = \frac{2c \cos \phi}{1 - \sin \phi} \quad (3-2)$$

The cohesion values and unconfined yield strength for the various mixtures used in the experiments are listed in table 3-1.

Table 3-1. Cohesion & unconfined yield strength for mixtures used in experiments

% wt. Oil	cohesion (kg_f/m²)	f_c (kg_f/m²)
0.00	0.00	0.00
0.10	3.08	10.85
0.15	3.76	13.27
0.27	10.64	37.75

Results

Being that the frames are taken sequentially one every thirtieth of a second the concentration of markers can be readily plotted versus time. Figure 3-6 plots the concentration of markers for the various cohesion values tested. The markers are initially placed above the analyzing window which explains the initial concentration of zero. As the markers are set in motion they begin to rotate and enter the analyzing window forming the first of many peaks. The start of one peak to another corresponds to the duration of time it takes the markers to complete one cycle. Recall that one cycle for a rotary shell blender is one full revolution of the material in the drum and not one full revolution of the drum. After every subsequent cycle the peaks broaden as the distance between them is shortened. Eventually the peaks begin to overlap

until equilibrium is attained and a constant value is reached. Once the concentration ceases to fluctuate and steady state is achieved blending is complete.

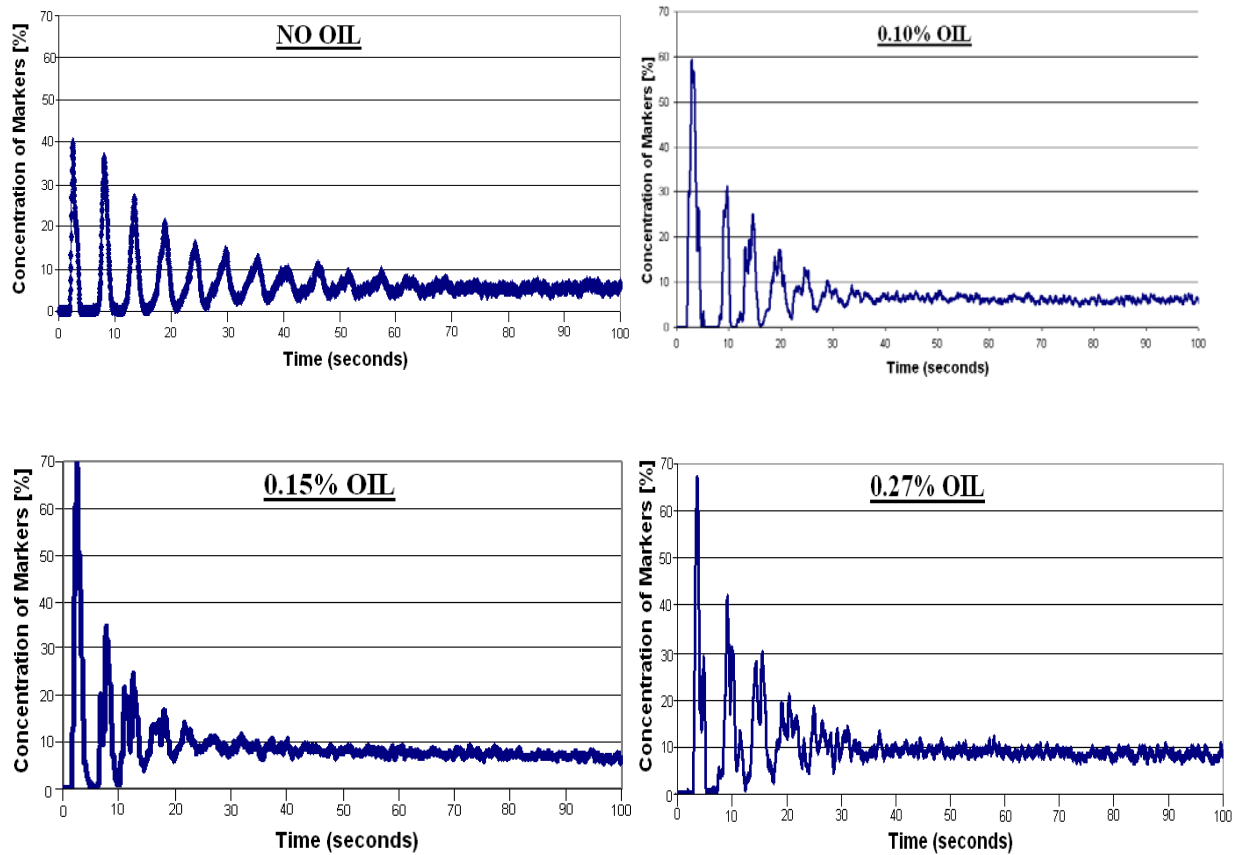


Figure 3-6. Concentration peaks of markers

As the markers slowly begin to distribute themselves throughout the mixture the spatic fluctuation from high to low concentration of markers within the analyzing window, along with other parts of the mixture, will slowly begin to dissipate leveling off to a constant value equivalent to the initial concentration of markers placed in the drum. The blenders ability to dampen these fluctuations are most conveniently assessed through calculation of its variance, σ^2 .

$$\sigma^2 = \frac{1}{n-1} \sum_{i=1}^n \left(c_i - \frac{1}{n} \sum_{i=1}^n c_i \right)^2 \quad (3-1)$$

Variance is a means of quantifying the spread of data. The larger the spread of the individual measurements from the mean the greater the variance. As the variance approaches zero the drastic fluctuation of the individual measurements diminishes. The variance of the various runs were determined by applying a running average in which the variance was calculated for time increment t for every time increment starting at time increment 300, by averaging the concentration 300 time increment before time t and 300 increment after time t . Figure 3-5 shows the variance of the marker concentration within the analyzing window for the various experiments performed at varying cohesion levels.

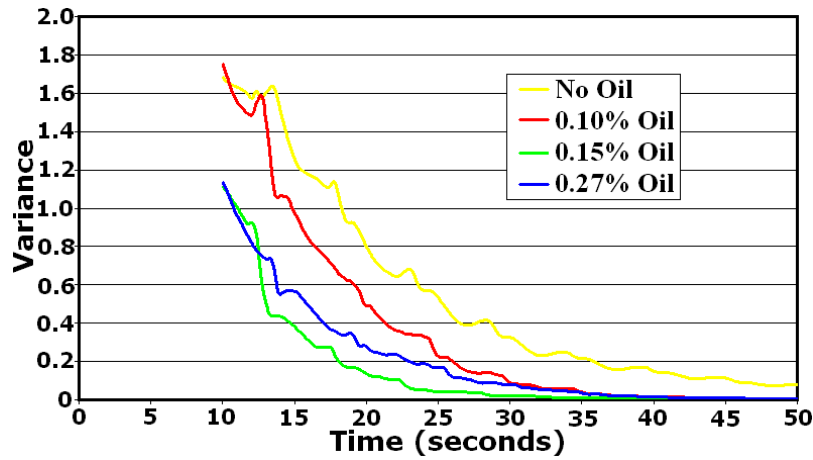


Figure 3-7. Variance of markers

From the plots in figure 3-7 we observed that the time required to achieve adequate mixing improves with the addition of oil until a certain critical point is reached. Upon reaching this critical point the adverse affect is noted in which the blending time decreases with the addition of oil. This phenomenon can be explained by taking note of some key observations. In a rotary shell blender mixing occurs entire in the plastic region. The plastic region governs the blender's overall performance. With the addition of oil an increase in the mixture's cohesion occurs, which as a direct affect on the shape, size and velocity profile within the plastic region. As we apply more oil to the mixture, increasing its cohesion, the size of the plastic region enlarges expanding

the area in which blending occurs. By enlarging the plastic region the addition of oil promotes blending while simultaneously inhibiting it by decreasing the velocity profile within the plastic region affecting the velocity gradients between particles that allow them to separate. Blending therefore has two counter acting mechanism affected by cohesion, one that is beneficial to blending and one that is detrimental. The two mechanisms are continually competing with one another, with one mechanism constantly overshadowing the other. There exists an optimal cohesion level, a critical value, in which we see a switch in favoritism from one of the two competing mechanism for the other. Mixtures with cohesion levels that fall below this critical value will tend to favor the mechanism that promotes blending and will continue to do so until reaching and surpassing the critical value in which case blending is then over taken by the mechanism which impedes it.

CHAPTER 4 MODEL VALIDATION

To validate our models of a rotary shell blender an in house code was written in both C++ and Matlab. All major aspects such as attaining marker position, velocity, etc. of the two models were implemented entirely in the code written in C++. Matlab was used solely for graphical purposes, due to its superior graphing capabilities. Upon completion essential data executed in C++ are exported to text files which are then imported to Matlab. Key parameters from the experiments were measured and implement in the codes. They include blender geometry and operational parameters such as the radius of the drum and angular velocity, material properties such as angle of internal friction and material weight density are also included. A number of simulations where performed, simulations were done where every possible aspect was replicated to correspond identically with those from the experiments as well as additional simulations we felt provided further insight into blending. In the subsequent sections the logic for the various simulations will be discussed while comparing their results to those of the actual experiments, however prior to this the means of assessing the validity of the models will be addressed.

The primary objective of a blender is to combine several components to produce a mixture that is as homogeneous as possible by neutralizing random fluctuations in the concentration. Unfortunately random fluctuation and inconsistency will always be present, a blender's ability and rate of minimizing these fluctuations defines its effectiveness. Validation of the models can be accomplished by evaluating their ability to deal with these fluctuations in comparison to those of the experiments.

In practice blenders are assessed by measuring the uniformity of the mixture by taking random samples at various time increments. The uniformity of our experiments, as discussed in chapter 3, were measured optically. The concentration was measured continuously at a fixed

location referred to as the analyzing window. An illustration of the analyzing window is shown in figure 3-3. Since the concentration was monitored in a single fixed location the concentration will increase and decrease accordingly, adjusting to the flux of markers entering and exiting the analyzing window at any given moment. An idealized version of the blending process is depicted in figure 4-1 in which the concentration of markers is plotted versus cycles, where a cycle is composed of 10 individual time increments. The first set of 16 blocks numbered 1-16 represents the initial pass of markers through the analyzing window. Upon exit of the last marker a period of inactivity ensues within the analyzing window dropping the concentration to zero as the markers make their way through the blender. Moving about the blender the markers begin to separate from one another dispersing themselves amongst the other particles of the mixture.

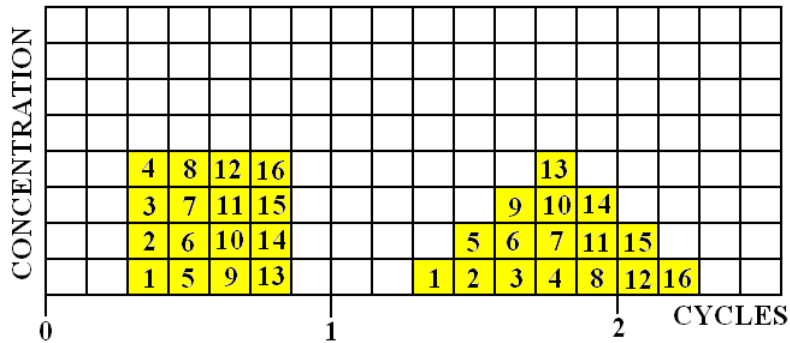


Figure 4-1. Schematic of concentration peaks

As the markers resume their given path they inevitably reenter the analyzing window where the concentration once again resumes increasing. Being that the markers are now a little more disperse, after completion of one full cycle, the duration of time between entry of the first marker and departure of the last maker from the analyzing window will increase, consequentially widening the base of the second peak. Refer to figure 4-1. With every succeeding cycle the makers progressively disperse from one another widening the base of the subsequent peaks while

simultaneously shortening the distance between them. Inevitably the peaks will start to overlap where they eventually coalesce to a relatively constant value at which point the flux of markers into the analyzing window is balanced by the outward flux.

The first criteria that is used to validate the models with the experiments is the duration of time it takes the markers to complete a blending increment or cycle. The simplest and most effective method of determining this is by measuring the distances between the apexes of the concentration peaks. Even though there is a distribution of residence times within the blender and each particle takes its own stochastic path, on average the distance between the apexes of the peaks is the average time it takes a particle to complete one cycle. The distance between sequential peaks should be equivalent. Discrepancies in cycle times between simulations and experiments would result in erroneous forecasting of blending times. A cycle time shorter than that of reality would unquestionably predict a premature blending time as would a lengthier cycle time be expected to overestimate the blending time. The sensitivity of the error is dependent upon the actual number of cycles implemented prior to achieving a uniform distribution as the error would compound with every progressing cycle.

As the first criteria offers insight to the average speed of the markers as a whole as they make their way through the blender, the width of the concentration peaks divulges more of the blender's tendencies to disperse particles. As the particles travel through the elastic region of the bed their positions relative to each other remain unchanged. Upon entry into the plastic region they experience a multitude of velocities that enable the markers to travel past one another at various speeds dispersing them. The velocity within the plastic region is dependent upon a number of factors such as cohesion and stress, both of which were incorporated into the models along with other factors. The magnitude of the velocities do not aid in the promotion of

blending, what is significant however is the distribution of the velocities. The more considerable the distribution the greater the dispersion of the particles. The dispersion of the markers are directly reflected by the width of the concentration peaks. Wider peaks signifies greater dispersion as the period between entry of the first marker to the exit of the last marker in the analyzing window is broader. Since blending takes place solely in the plastic region any discrepancies in the width of the concentration peaks for the simulations with those of reality can be traced back to the velocity profiles. Too narrow of a peak suggests a lack in the differential of the velocities amongst the particles as too broad of a peak would suggest the contrary. If the width of subsequent peaks do not change this indicates that the particles are indeed in motion, but engaged in plug flow in which the particles are not capable of separating from one another.

Although the first two criteria provided crucial insight and understanding of the blending mechanisms they fail to answer the primary question that all proficient blender operations desire to know, when to terminate the blending process. One could ideally determine when to terminate blending upon inspection of the concentration versus cycle plots. Once the concentration reached a relatively constant value the process could be terminated. The problem however lies in the standardization. Determining the precise moment in which the fluctuations are at their lowest is extremely difficult and entirely dependent upon the scrutiny of the operator. The simplest and most effective method is to determine its variance in terms of concentration. Upon reaching a predefined value in which the variance is allowed to deviate from zero the blending process would be terminated. By setting the increments upon which the concentrations are measured results in unvarying, consistent, repeatable results that do not vary with operator. Initially the variance will start off high as concentration within the analyzing window drastically fluctuates from periods of high concentration to periods of low concentrations. As the markers

start to disperse the drastic fluctuations will gradually begin to subside. Too rapid of a drop in the variance is indicative of a model that prematurely predicts blending whereas too subtle of a decline results in predictions that surpasses reality. If deviations from actuality are present within the model in all likelihood they are caused by either an error of some form or another that affect the velocity profile of the particles or the lack of inclusion of an essential blending mechanism in its entirety.

In the subsequent sections the various simulations performed will be discussed in detail as well as their results. The validation techniques just formerly mentioned will be implemented. There were two primary simulations written, one for the parabolic model and another for the model that incorporated the method of characteristics. Aside from the two primary simulations additional simulations were written in which minor modification were made to the parabolic model that repositioned the initial placement of the markers. The rationale for these additional simulations will be discussed below.

Placement of Markers on Top Surface

The first set of simulations performed were meant to duplicate those of the experiments. Initially the free surface starts perfectly aligned with the horizontal, upon initiation of the drum's rotation the *simple method of slices* is employed to determine the stability of the plastic region. Once the plastic region has reached the point of instability, 150 markers are placed in a fictitious rectangular area situated in the upper right hand corner of the bulk. Refer to figure 4-2. Being that the markers constituted 5% by weight of the total mixture and that the bulk density of markers are identical to that of the other particles the rectangular area, in an attempt to replicate the experiments, occupied an area comprising 5% of the bed.

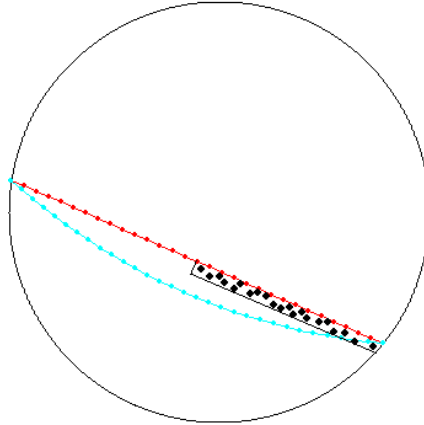


Figure 4-2. Horizontal placement of markers

Originally the markers were evenly distributed throughout the rectangular area in perfectly aligned columns and rows, but in an effort to improve legitimacy the markers were randomly scattered throughout the area using a random number generator predefined in C++. Being that particles are of narrow size distribution I set a uniform number distribution. Equal weight was given to the markers. The area represented by a single marker was determined by dividing the area of the fictitious rectangular region that the markers initially occupy by the total number of markers.

Prior to completion of even a single cycle the simulation was destined for failure. A fatal flaw was made from the very beginning in the initial positioning of the markers. Replicating the experiments the markers in the simulations were placed in the upper right hand corner of the bed. The reasoning behind the placement of the markers in such a manner was fear that markers scattered elsewhere throughout the plastic region would not experience the full blending increment as described in chapter 2. It was assumed that markers placed in the upper right hand corner of the bed would enter the elastic region relatively instantaneous without much blending occurring. The markers were then to travel through the elastic region as a rigid body where they

were to enter the plastic region at various locations ensuring that they spent the entire duration within the plastic region in order to experience the entire blending increment.

The simulations were performed as if the transition from slope stability to failure is instantaneous. The moment the free surface reached the point of stability the markers are introduced into the system. Although transition is achieved relatively quickly the placement of the markers are tremendously affected. In the experiments prior to the formation of a steady continuous plastic region there is an initial slough of material down the free surface displacing the markers in a random unstructured pattern within the elastic region. In the simulation, which does not account for the initial slough of material, a considerable portion of the markers are situated in the plastic region resulting not in a quick unaltered induction into the elastic region, but a clustering of the markers along the periphery of the drum. This clustering of the markers resulted in the markers entering the plastic region exclusively from the periphery, limiting the possible paths available within the plastic region, therefore only accounting for a portion of the blending increment.

Although this particular simulation was unsuccessful for a number of reasons we felt it warranted mention due to the tremendous insight that it provides. The indispensable realization acquired was that marker placement is crucial; it must be positioned appropriately in order to ensure that the entire blending increment is encompassed.

Placement of Markers via Scanning

From the previous section arose the awareness of the sensitivity of the system to the initial positioning of the markers. Along with this awareness came a number of concerns. In order to alleviate these concerns a number of steps were taken. Although initially positioned in an organized structured manner the markers are abruptly thrown in the elastic region forming an amorphous intricate pattern. Due to the elaborate nature that the form of the markers now

exhibit, instigated by the initial slough of the material, the markers can no longer be simply arranged within the bed. However by mapping the image from the video of the rotary shell blender the instant the markers enter the elastic region, upon the conclusion of the initial slough, the positioning of the markers within the code can be placed to match exceptionally well with the position of the markers from the video image.

Once imported into Matlab the video of the rotary shell blender can be view frame by frame. Recall images from the digital camcorder are not of the entire drum, but only of the lower right corner which allowed for an increase in resolution. Complicating matters the images were inverted. Figure 4-3 is an image taken the moment the markers enter the elastic region for the experiment done with 0.27% wt. oil. The initial slough occurs relatively quickly allowing for the precise moment that the markers enter the elastic region to be determined without much difficulty.

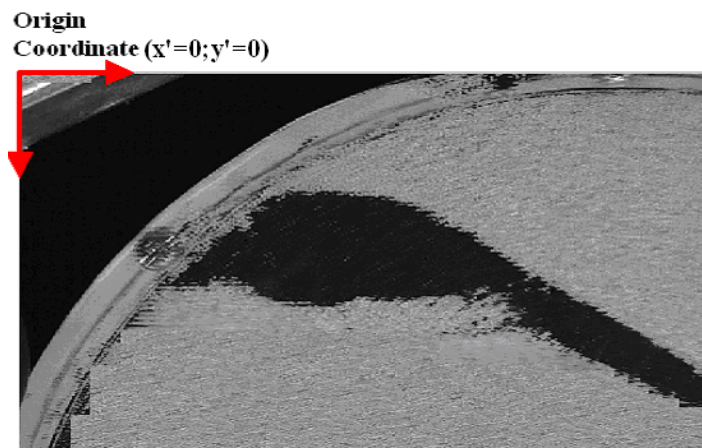


Figure 4-3. Image from camcorder immediately following initial slough of material

The images are partitioned into individual pixels, being that the resolution of the camcorder was 720 X 480 there were 345,000 pixels in total. The threshold value of each pixel was stored in a 720 X 480 matrix. A coordinate system (x',y') was assigned to the image, with its origin located in the top left corner, through which the position of the pixels can be obtained.

Refer to figure 4-3. The dimension of a pixel constituted a unit length for the coordinate system. For instance a pixel located in row 135 and column 435 of the matrix would have a coordinate value of $(x' = 435, y' = 135)$.

In order to accurately map the position of the markers from the video image to the simulation, key reference points must be defined relating the two. Since the video image only captures a portion of the drum we are limited in our selections. Cognizant of the quantity of material placed within the drum the location that the upper right hand corner of the material comes to rests along the periphery can be used in conjunction with the bottom of the drum as reference points. A schematic of the drum used for the simulation along with the drum from the video image, shown in its entirety, are illustrated in figure 4-4. The dashed green lines shown in the diagram to the right in figure 4-4 outlines the area depicting the focus area of the camcorder.

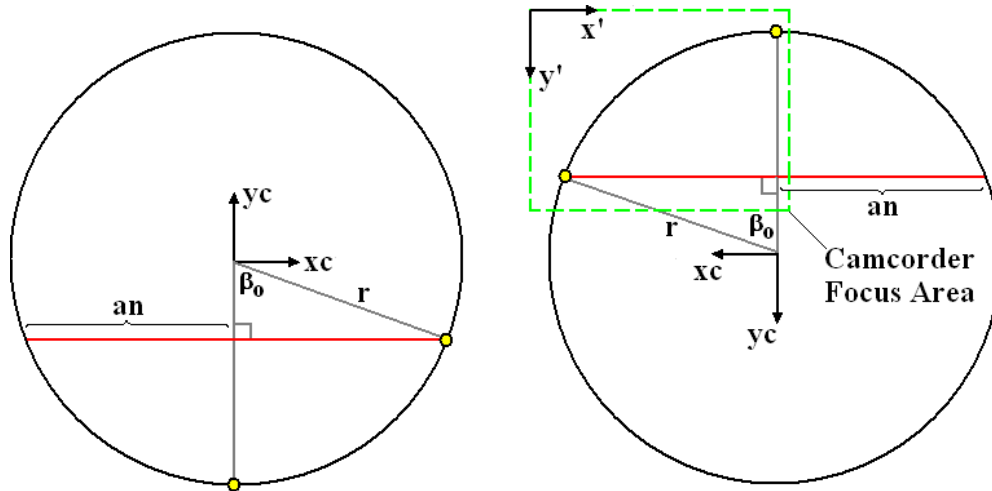


Figure 4-4. Mapping of markers

Using the radius of the drum along with β_0 , angle the center of drum makes with the corner of the bed, as scaling factors the two coordinates systems (x', y') and (x_c, y_c) can be used interchangeably in the mapping of the markers. β_0 is the same for both system, the radius however is determined by equation 4-1 where an is half the distance of the free surface.

$$r = \frac{an}{\sin(\beta_0)} \quad (4-1)$$

Subtracting from the video image the x' coordinates of the two reference points the length of an is attained, which is then used in equation 4-1 to obtain the length of the radius in accordance with the length scale of the (x',y') coordinate system. The length of the radius is then used to obtain the y' coordinate of the center of the drum, providing a third reference point. To be fully capable of interchanging from one coordinate system to the other a minimum of two sets of points are required in order to observe the change that the points undergo in the (x',y') coordinates system compared to those in the (x_c,y_c) coordinates system.

Table 4-1. Reference points & coordinate transformation equation from x' to x_c
Horizontal Change

	Simulation	Video Image	Coordinate Transformation Equ.
0.27% Oil	$x_c=0$ $x_c=an$	$x'=640$ $x'=40$	$-4000x_c + 640 = x'$
0.15% Oil	$x_c=0$ $x_c=an$	$x'=621$ $x'=48$	$-3820x_c + 621 = x'$
0.10% Oil	$x_c=0$ $x_c=an$	$x'=648$ $x'=46$	$-4013x_c + 648 = x'$

Table 4-2. Reference points & coordinate transformation equation from y' to y_c
Vertical Change

	Simulation	Video Image	Coordinate Transformation Equ.
0.27% Oil	$y_c=0$ $y_c=-r$	$y'=642$ $y'=31$	$4000y_c + 642 = y'$
0.15% Oil	$y_c=0$ $y_c=-r$	$y'=639$ $y'=46$	$3819y_c + 639 = y'$
0.10% Oil	$y_c=0$ $y_c=-r$	$y'=647$ $y'=24$	$4013y_c + 647 = y'$

Table 4-1 lists the x_c coordinates of the reference points in the simulations along with their corresponding x' coordinates from the video image. These points are then use to derive a transformation equation which allows one to freely interchange from one coordinate system to the other. Similarly the y_c and y' coordinates of the reference points and the corresponding transformation equation are listed in table 4-2.

Initially the first few images are visually inspected awaiting the imminent initial slough of material. Upon identifying the precise frame in which the markers enter the elastic region the image is analyzed and mapping is initiated. Refer to chapter 3 for analyzing procedure. The coordinates of all pixels with a threshold value of 70 or less are altered using the coordinate transformation equation in table 4-1 and 4-2 to enable positioning of the markers in the simulations which are plotted in (x_c, y_c) coordinates.

Unable to distinguish the black particles from the blackness of empty space all pixels that were counted with a threshold of 70 or less that lie outside the periphery of the drum are ignored. A single particle is represented by approximately 12 pixels, being that there are thousands of pixels that have a threshold value of 70 or less it is impractical to incorporate all into the simulation due to limited computation capabilities of the computer. To achieve a reasonable computation time 150 tracer particles will be employed in the simulations. All altered pixels from the video image are however imported into the simulation. The bed of the material is divided into a grid in which the altered pixels are contained (see figure 4-5). The number of pixels contained in each grid box is tallied and assigned to each box is a number density in which the boxes are then ordered from highest to lowest density. Based on the density of each grid box the number of markers allocated to each grid box is distributed accordingly.

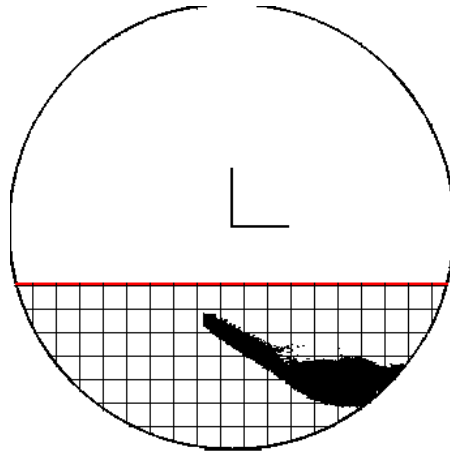


Figure 4-5. Imported scanner markers

Similar to the preceding program where the markers are placed in the upper right hand corner of the bed the simulation begins with the free surface aligned with the horizontal. The drum begins to rotate until inevitably reaching the point of instability at which point the markers are introduced to the system were they are assigned to their appropriate location within the grid boxes as previously stated. Once introduced to the system the markers begin to travel through the blender at velocities dictated by its position within the blender. As the markers make their way through the blender completing a full cycle they pass the finish line, refer back to figure 2-28 for finish line placement, where the markers are tallied and its residence time distribution function is determined. From the residence time distribution function the concentration of the markers versus time is obtain via equation 2-60.

The most effective means of assessing the simulations predictive capabilities is to compare the concentration variance of the markers from the simulations side-by-side with those of the experiments. Figure 4-6 contain the side-by-side comparison for the various cohesion values. From inspection of the variance graphs in becomes immediate clear that the simulations are unsatisfactory in there predictive capabilities. Upon examination of the governing equations it became apparent to us that the positioning of the markers is in direct violation of a principal

criteria of the governing equations. The effectiveness of the predictive capabilities of equation 2-88 is based on the criteria that the transfer function $G(z)$ that relates the concentration exiting a blender to the input concentration is equal to the residence distribution function for a single cycle of the blender for a unit impulse. To be considered a unit impulse the particles of the markers must encompass the entire velocity profile within the blender without the particles duplicating the path of another. With the current positioning of the markers it is impossible for a single marker to enter the plastic region without a subsequent markers directly following behind it, rendering equation 2-88 incapable of predicting blending.

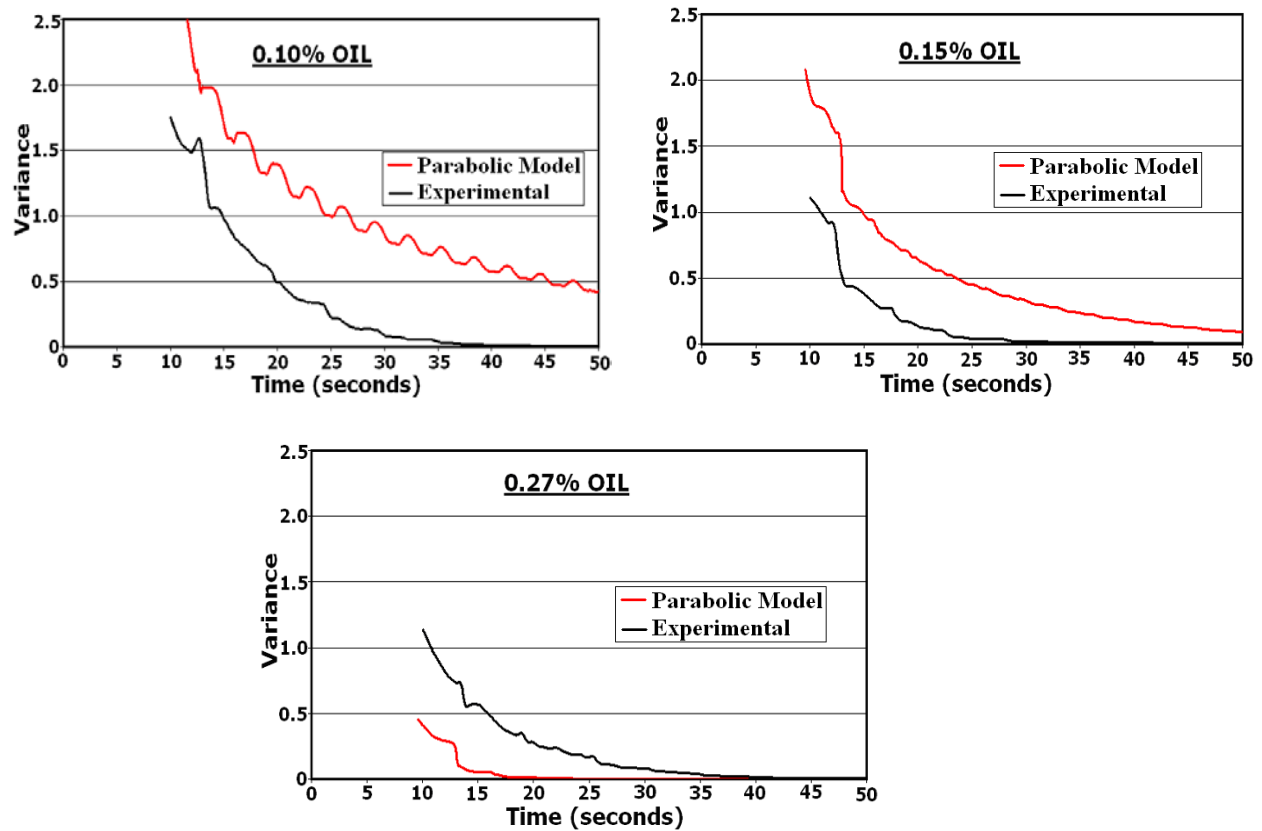


Figure 4-6. Variance of simulations of the parabolic model vs. experimental variance

Placement of Markers in Single Vertical Strip

In the previous sections attempts were made in order to produce simulations that were as authentic and genuine to the experiments as possible. Parameters were prudently selected and

set to conform as closely as possible with every aspect of the experiments. Unbeknownst to us at the time these attempts to duplicate the experiments, although successful, are incapable of being used in implementation of our model to predict blending. When the experiments were initially performed we were unaware of the tremendous influence that the placement of markers, what we then believed at the time to be a trivial issue, would have upon the blending process. We were cognizant of the fact that a unit impulse was needed, but unaware that by placing the markers along the free surface in upper right hand corner of the drum that they would bunch up rearrange themselves in a pattern that prevents them from operating as a unit impulse.

To function as a unit impulse the markers must be positioned in such a manner so that each individual marker only travels a single path, from the multitude of possible paths within the blending increment, never to duplicate the path of another. The markers as a whole however must encompass the entire spectrum of the velocity profile contained in the blending increment. In order to accomplish this the most logical placement of the markers is a single vertical strip that runs down the center of the bed perpendicular with the free surface. Refer to figure 4-7.

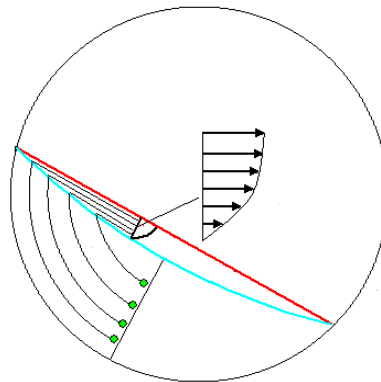


Figure 4-7. Vertical placement of tracers

In this configuration the markers are initially in the elastic region where they begin to rotate as a rigid body. As they rotate, remaining in perfectly parallel paths adjacent to one another, the marker closest in proximity to the center of the drum will be the first to arrive at the elastic-plastic

interface. Upon arriving at the interface the marker will commence travel through the plastic region at a velocity specified by its position within the plastic region. Shortly thereafter the marker directly below the first marker will reach the elastic-plastic interface at a position slightly higher than that of the first marker. Starting at a higher position the second marker will travel at a greater speed. One by one the markers will enter the plastic region with every succeeding marker slightly higher than the one preceding it. This slight change in position is what enables us to capture the velocity profile in its entirety.

As the markers make their way through the blender the residence time distribution function is determined by measuring the duration of time it takes the markers to complete one full cycle. Recall a blending increment of a rotary shell blender is one full revolution of the material. Being that the markers originated at the center of the bulk, a line which we termed the finish line was placed to the right directly adjacent to the initial strip of markers which represents the hypothetical entrance and exits of a continuous blender. Refer to figure 4-7 for placement of the finish line. As the markers make their initial pass through the finish line they are tallied and the residence time distribution function is obtained. From the residence time distribution function the concentration of the blender after subsequent cycles are determined by means of equation 2-60. The results of these calculations for the parabolic model are shown in figure 4-8 for three varying cohesion values. The cohesion values used in the simulations correspond to those of the lubricated sands used in the experiments.

For the graphs in figure 4-8 the criteria that most interests us is the moment in which the concentration reaches an acceptable degree of fluctuation, indicating the components of the mixture are fairly homogeneously distributed throughout the bulk signaling the completion of the

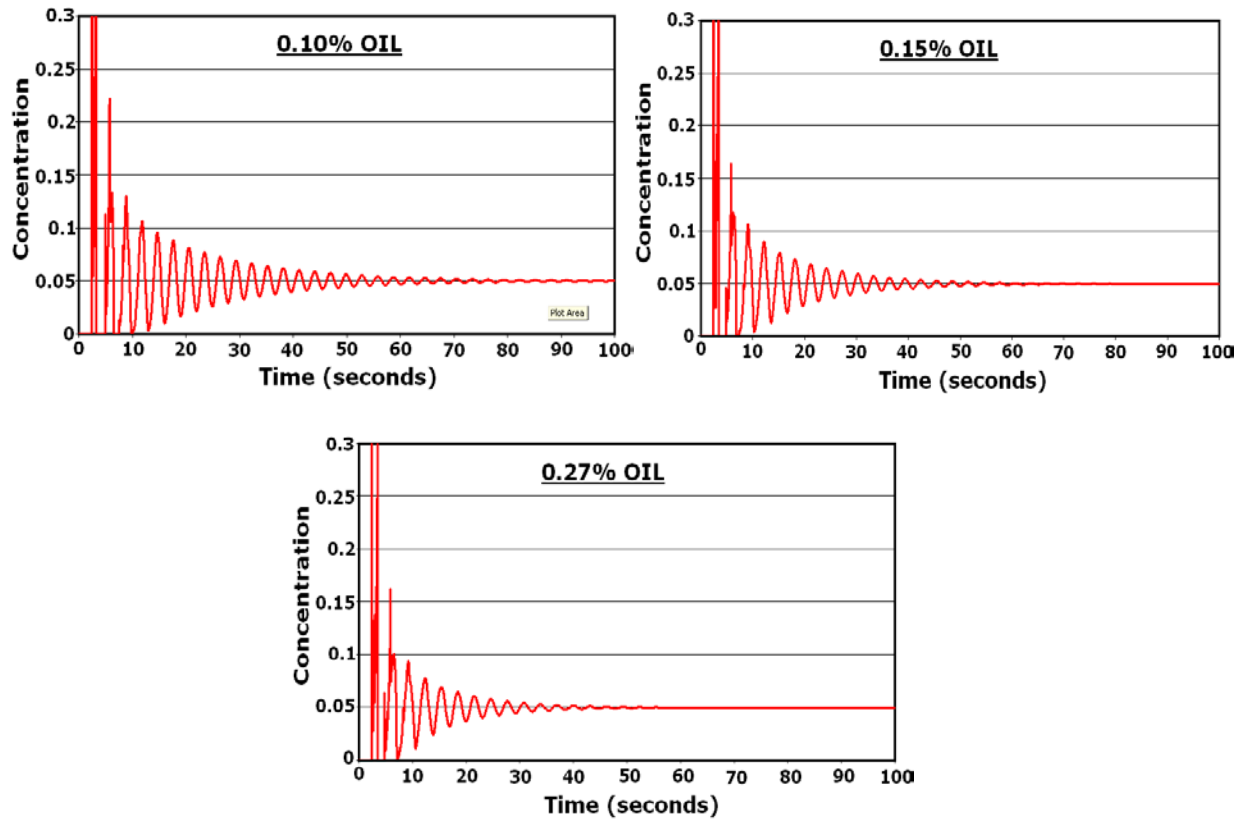


Figure 4-8. Concentration peaks of markers for parabolic model blending process. Comparing the graphs in figure 4-8 we observe a quicker arrive of homogeneity for those graphs of simulations performed at higher cohesion values. The simulations performed at higher cohesion values produced thicker avalanches then those at lower values. Figure 4-8 contains images of the actual avalanches taken from the various simulations while at the greatest point of inclination. The thickness of the avalanches varied according to Sokolovskii's model, equation 2-2. The increase in the thickness of the avalanche at higher cohesion values yielded a greater area in which the components of the mixture can blend allowing for a shorter blending time. This is indicated in the concentration graphs in figure 4-7 through the widening of the peaks.

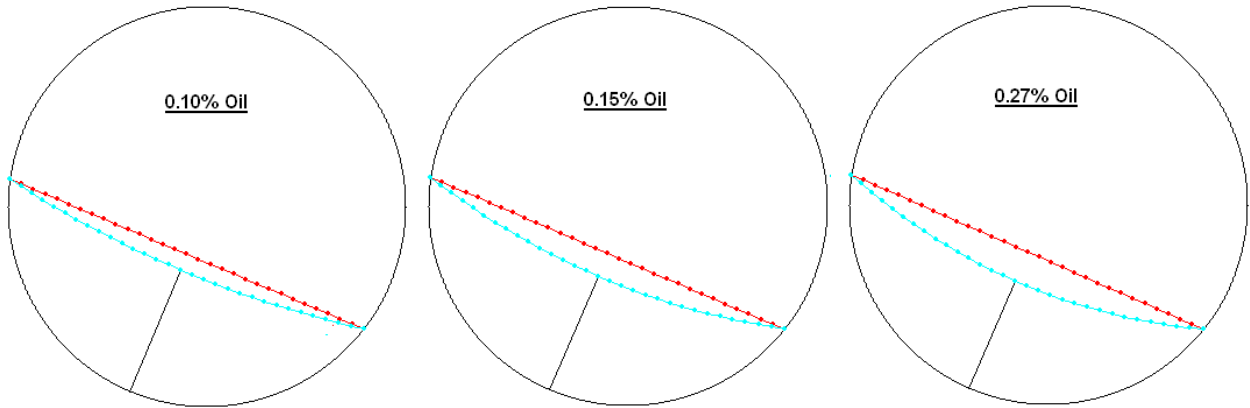


Figure 4-9. Thickness of avalanches from simulations of parabolic model

Although it is clear from the graphs in figure 4-8 that cohesion helps facilitates the blending process it is difficult for one to determine the precise moment in which the fluctuation are at their lowest, allowing for discrepancies to exist between operators. Plotting the variance of the concentration according to equation 3-1 allows for considerably easier analysis of the dispersion of the components of the mixture not only upon completion but throughout the blending process. Figure 4-10 is a graph of the variance of the concentration for the simulations of the parabolic model for the various cohesion values. From the graph it is clearly evident that cohesion immediately as a favorable effect on blending and continues to do so throughout the blending process. Although it seems that the simulation is capable of predicting the trend of

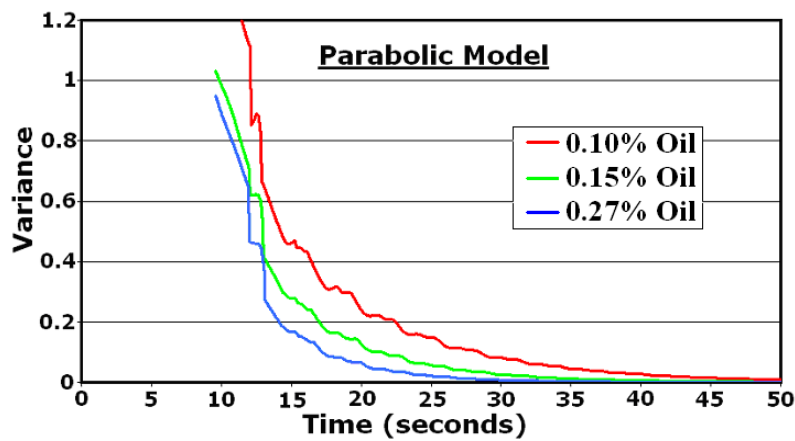


Figure 4-10. Variance of simulations of the parabolic model at various cohesion values

greater proficiency in blending with higher cohesion values for materials that are below the critical value, as specified by the experimental section of chapter 3, it appears inadequate in predicting the reverse trend for cohesion values larger than that of the critical value.

When the cohesion of the material exceeds that of the critical values a new mechanism of blending is introduced to the system. The plastic region, which was assumed to be a smooth continuous curve no longer applies, the plastic region is transfigured into an ever changing series of erratic cascades. These cascades that were experimentally observed solely for the case of the highest cohesion values are initially formed in the upper portion of the plastic region. Possessing more strength the particles within the avalanche cling to one another with greater intensity than in the previous cases. The particles unwilling to rupture their bond with one another remain intact until inevitably they are no longer capable of supporting the weight of the constant accumulation of particles flowing from the elastic region resulting in the formation of a shear plane in which the material is then forced to slide down with little or no blending occurring from within the cascades.

These cascades that take place at higher cohesion values rapidly become the primary blending mechanism as they transfer large groups of material throughout the blender, overshadowing the blending that takes place as a result of the shear that develops between the particles as they traverse pass one another in the plastic region. This cascading mechanism that is responsible for a substantial portion of the blending process at high cohesion values is missing in its entirety from our model. This is undoubtedly the rationale behind the model's inability to predict the reverse trend that occurs in blending when at cohesion values larger than that of the critical value. Surely incorporating the cascading mechanism into the current model will remedy any discrepancies that exist in the results for these higher cohesion values allowing for accurate

prediction to be made not only for cohesion values below the critical value but for an entire array of values.

The graphs in figure 4-8 enables us to note the impact of cohesion on blending as a whole, however to ascertain the accuracy of the model the variance at the various cohesion values for the simulation must be compared side-by-side with those of the experiments. The side-by-side comparisons are shown in Figure 4-11. For the case of the lowest and intermediate cohesion values both of which are below the critical value necessary to possess sufficient strength to temporarily support an avalanche that would initiate into a cascade, the model is capable of predicting with accuracy the appropriate amount of time essential for blending. The actual blending time varies as it depends on the acceptable tolerance of the application in which it is being applied, but from the graphs in 4-10 we see that for the lowest cohesion case of 0.10% wt. oil we obtain a blending time of 35 seconds at a variance of less than 3% for both simulation and experiment while for the intermediate case of 0.15% wt. oil we obtain a blending time of approximately 29 seconds at a variance of less than 3% for both simulation and experiments. Although in both cases the blending time of the simulations correspond with those of the experiments the variance of the intermediate cohesion of 0.15% wt. oil is in greater agreement throughout the blending process than that of the lowest cohesion value of 0.10% wt. oil which tends to deviate from the experiments in the initial stages. For these cases in which the cohesion is below that of the critical value blending is controlled by two counteracting mechanism, both the area of the plastic region as well as the velocity within the plastic region play a pivotal role in influencing the blending process. The area of the plastic region is governed by Sokolovskii's equation, equation 2-2 in which the area is indirectly influence by cohesion through the use of the *simple method of slices* in which the angle of inclination, ε , is dependent upon cohesion.

The magnitude of the velocity of the particles within the plastic region is determined by a volumetric mass balance in which cohesion comes into play through the thickness of the delta lines in which the volumetric flow rate is determined. Although cohesion has an effect on the magnitude of the velocity it does not have any influence upon the velocity gradient. The velocity gradient is defined through the coefficient k_1 which is arbitrarily chosen. From table 1-1 we see that with lower k_1 values the velocity gradient is more pronounced distributing the particles more readily as opposed to larger values of k_1 in which the velocity profile start to resemble that of plug flow where all the particles travel relatively at the same velocity. All three simulations were performed with the same k_1 value. A value of three was chosen simply because of the fact that it provides the most evenly distributed velocities. Refer back to table 1-1. Even with using a constant k_1 value we are able to arrive at the correct blending time, leaning toward the fact that

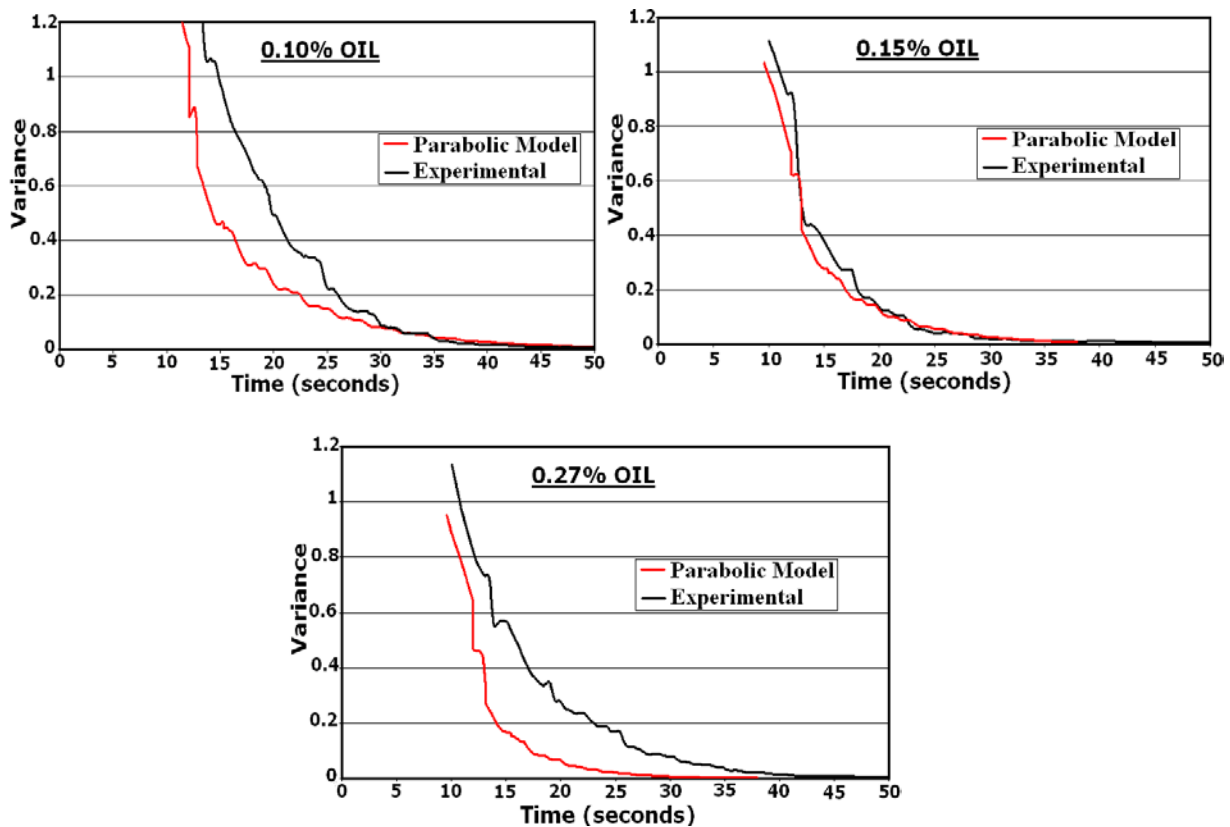


Figure 4-11. Variance of simulations of the parabolic model vs. experimental variance

the primary mechanism for blending is the acquirement of an accurate plastic region. It is only natural to assume that particles of a mixture of various cohesion values would possess varying degree of affinity towards one another diversifying its ability to dispersion and that by allowing k_1 to vary with cohesion along with other attributes of blending such as stresses from within the bulk that are induced either from powder boundary interaction or due to the self induced weight of the plastic region, we would be able to improve the predictive capabilities of the model.

The last graph in figure 4-11 is for the case of the highest cohesion of 0.27% wt. oil. The model fails as a result of the fact that it prematurely predicts the appropriate amount of time that should be allocated for blending. From the graph is it apparent that there is not a moment in which the simulation curve is compatible with that of the experimental. Referring back to figure 4-9 we see that the trend of the model is to continue with the forward progress of improvement in blending with higher and higher cohesion values while in reality a secondary blending mechanism is initiated driving blending in the reverse direction. The discrepancy in the third and final graph in figure 4-11 can be accounted for by the lack of the current model to incorporate for the cascading mechanism that occurs at higher cohesion values.

A set of simulations identical to those performed for the parabolic model were performed for the model that incorporates the method of characteristic. All parameters such as material propertied, rotational speed, placement of markers, etc were kept consistent with those of the parabolic model only the method in which the plastic region was determined along with the velocity profile within it varied. The concentration versus time at the various cohesion values are shown in figure 4-12.

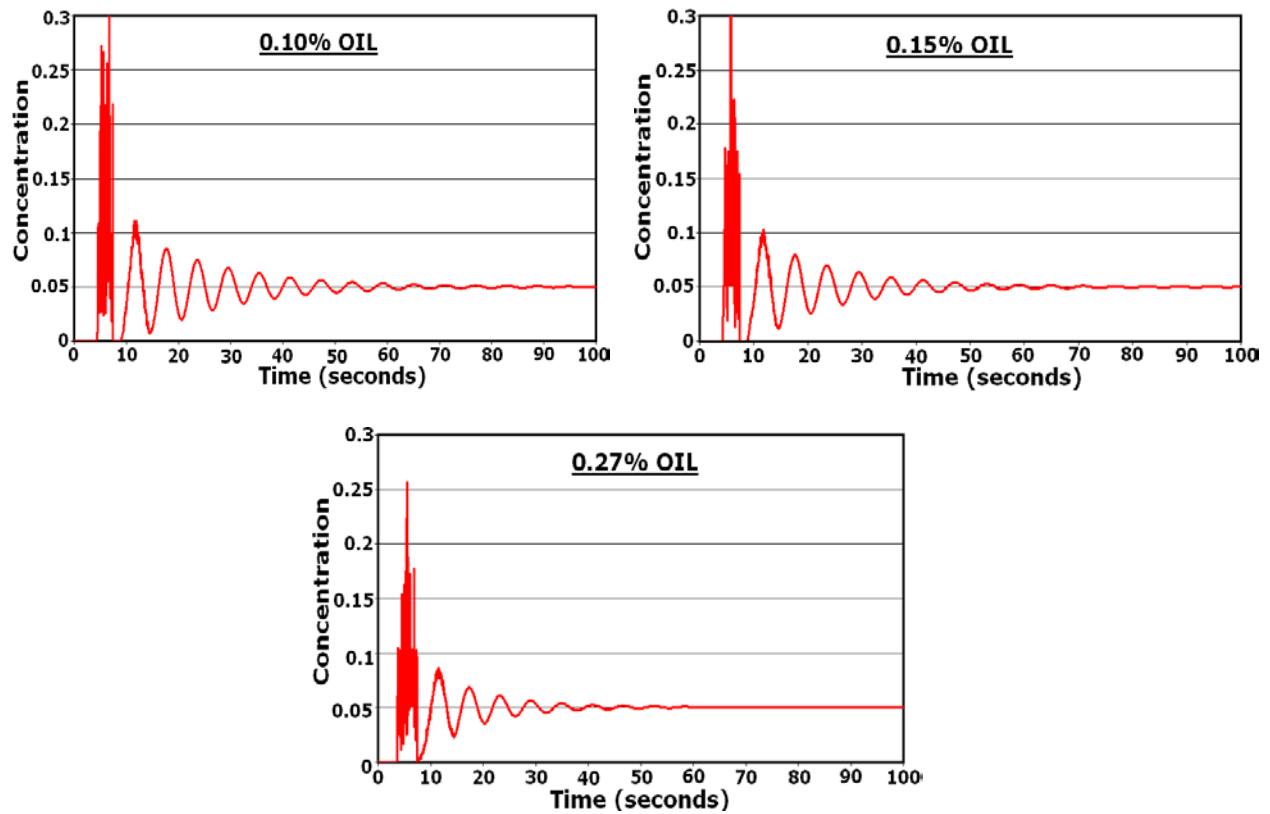


Figure 4-12. Concentration peaks of markers for method of characteristic model

Similar to the graphs of the parabolic model the graphs for the method of characteristic model yield quicker blend time for those simulations performed at higher cohesion value.

Comparing the thickness of the plastic region generated from the simulations, shown in figure 4-12, we see a clear increase with cohesion. Other than a slight flattening along the base of the

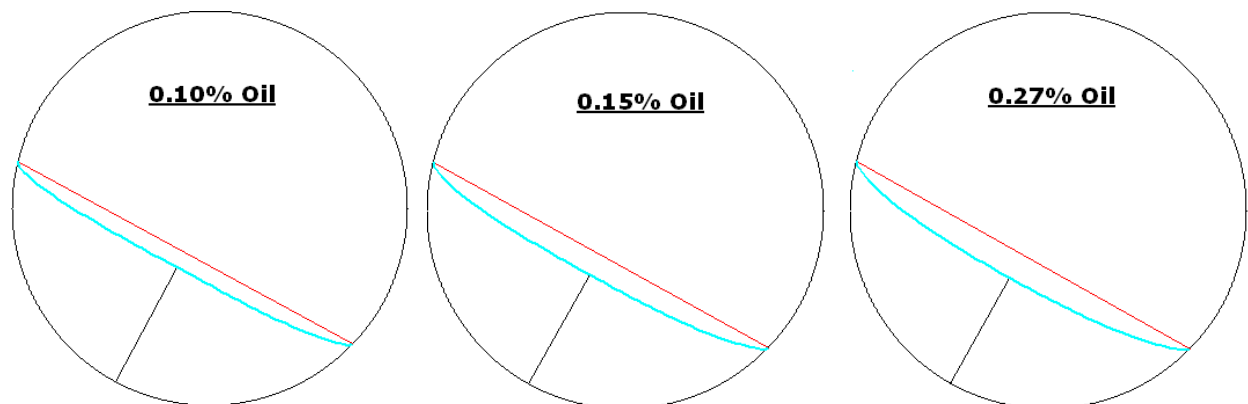


Figure 4-13. Thickness of avalanches from simulations of moc model

plastic region for the plastic region generated by the method of characteristic model the two models produce very similar plastic regions in both size and shape. Comparing the concentration peaks of the previous model in figure 4-8 with those of figure 4-12 we notice one primary difference, the width of the peaks for the method of characteristic are wider. Indicating a more disperse velocity gradient for the method of characteristic model then that of the parabolic model. Although possessing wider velocity gradients the blend times are in agreement with those of the experiments for the lowest and intermediate cohesion values, as can be seen in the first two graphs of Figure 4-14, alluding to the fact that the principal mechanism for blending for cohesion values below that of the critical value is the morphology of the plastic region. If one is

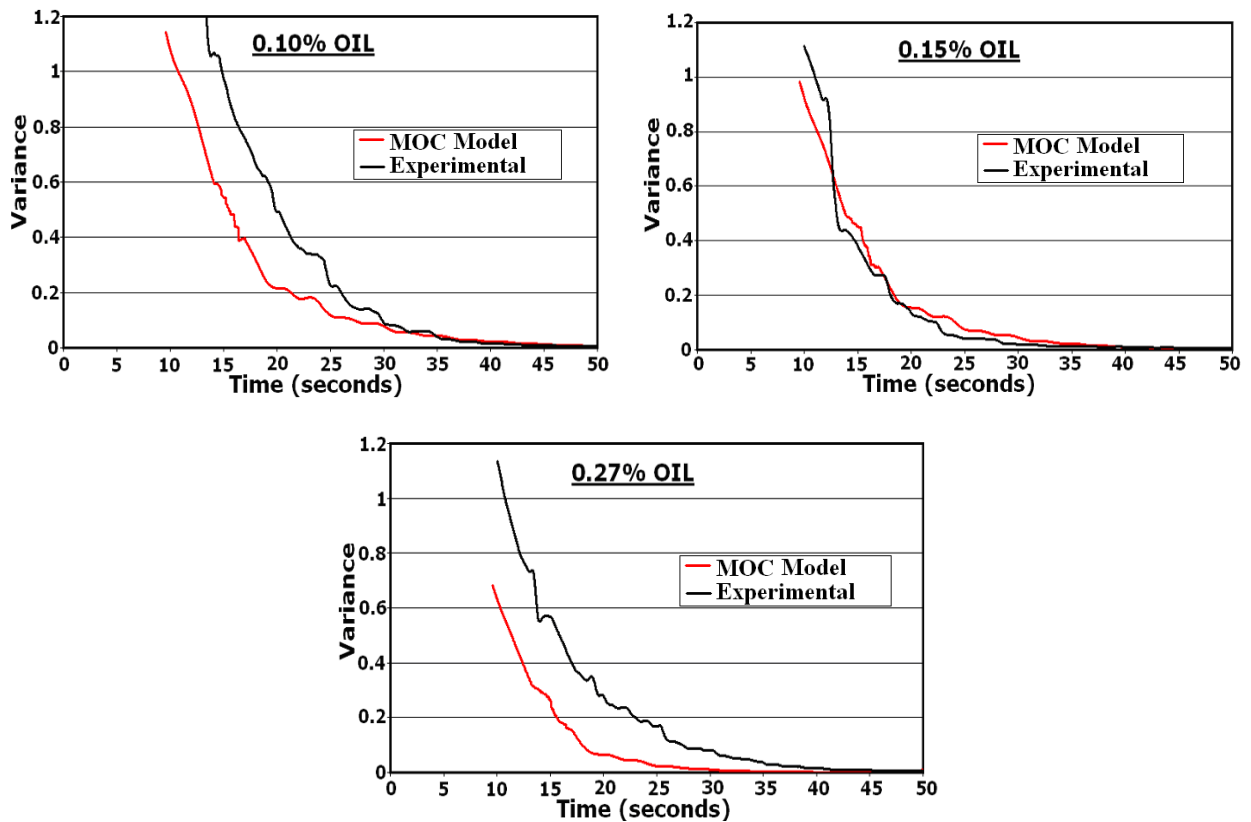


Figure 4-14. Variance of simulations of the moc model vs. experimental variance

able to accurately obtain the size and shape of the plastic region along with a velocity profile that is in relatively reasonable agreement with reality one is able to attain a truthful blend time that is in accord with reality.

For the case of the highest cohesion value of 0.27% wt. oil we were not capable of acquiring a reasonable blend time as was to be expected being that the method of characteristic model like the parabolic model did not include the phenomenon of cascading. Without the inclusion of the cascading mechanism, which occurs at higher cohesion values, the method of characteristic model exhibits the same trend that was observed in the parabolic model. As can be seen in figure 4-14 with higher cohesion values the model predicts an increase in the blender's performance allowing for an earlier blend time.

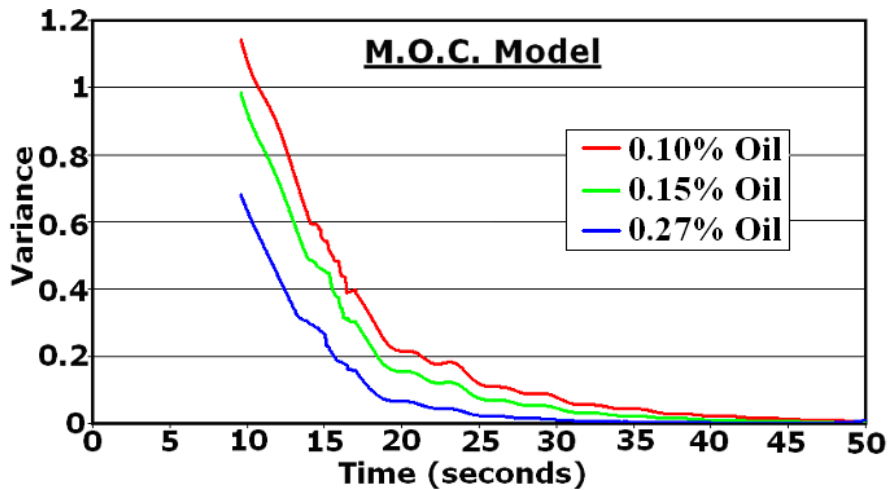


Figure 4-15. Variance of simulations of the moc model at various cohesion values

CHAPTER 4 CONCLUSION

Blending of particulate solids is a random and chaotic phenomenon, one that is of great importance that we understand. Blending is critical to all industries as it has a direct effect on desirable attributes of the final product such as chemical composition, color and texture. Despite its importance it is still one of the least understood unit operations. Within a blender there exists a series of possible trajectory in which the particles can travel. These trajectories cause the particles to have a distributed residence time allowing the blender to function. These trajectories are dependent on the flow properties of the components of the mixture and therefore are influenced by material properties such as cohesion and internal angle of friction. Blending is a convoluted process and therefore does not depend solely on material properties, blender geometry and operation parameters also have fundamental roles. The significant influence imposed by the material properties along with the blender geometry and operation parameters on the blending process is attributed to the difficulty in understanding and therefore predicting blending. Without a clear and comprehensive understanding of the relationship between these three parameters upon each other and the blending process we were forced in the past to utilize evasive sampling procedures that are time consuming and laborious. We proposed two continuum models, the parabolic and the method of characteristic model, that describes the blending phenomenon that takes place in a rotary shell blender from a macroscopic point of view. Both models de-convolute the material properties from those of the blender geometry and operational parameters, allowing us to predict the appropriate blend times regardless of the type of blender used the operation parameters it is operated at or the physical properties of its content.

For the case of the parabolic model the principal assumption was that the plastic region is described by a parabolic function in which its thickness is based on material properties using

Sokolovskii's equation. The plastic region was fixed in position upon reaching the point of instability assuming a smooth continuous curve. The thickness of the plastic region generated by the model correlated well with those of the experiments for the three cohesion values. Although the thicknesses of the plastic regions were in agreement there is still room for greater accuracy by incorporating a more demanding slope stability analysis. However, it is believed that marginal improvement of the plastic region will not have a profound effect on the overall performance of the model. The principal criteria used for assessing the merit of the model, is its ability to accurately predict the required blend times. The blend times were determined by establishing the moment the fluctuation in the markers concentration subsided to a reasonable level. Calculation of the concentration variance of the markers served as the simplest and most effective means of acquiring the blend times. Comparison of the blend times calculated by the model with those of the experiments showed comparable results for the lowest and intermediate cohesion levels. The model, however, predicted a blend time that was premature for the highest cohesion value. The variance plots generated by the model indicate a trend of greater efficiency occurring in blending at higher cohesion values in which we observe earlier blend times for the higher cohesion values. The same trend is observed experimentally where we see an improvement in blending with cohesion until a critical value is attained. Upon reaching this critical value we observed the reverse trend in which the efficiency of the blender decreases producing lengthier blend times. The discrepancy at higher cohesion value is attributed to a blending mechanism that is not present at lower cohesion values. The assumption of a smooth continuous curve for the plastic region no longer applies as the material of the mixture begins to gain strength. Capable of temporarily sustaining a load the plastic region develops into a series of random chaotic avalanches. During the intervals in which the avalanches are developing blending momentarily

ceases. These brief lapses in blending are not the only factors responsible for the reverse trend observed at higher cohesion values; the velocity profile is also affected. At these higher cohesion values the particles of the mixture cling to one another with greater intensity that the velocity profile starts to resemble plug flow, preventing the particles from dispersing as readily. Incorporating the cascading mechanism into the model for cohesion values larger than the critical value will remedy the current inconsistencies in the graphs.

When the bulk material of the mixture is of a cohesion value below that of the critical value it possesses insufficient strength for cascading to occur and is therefore a function of other mechanism of blending. For values below the critical value there are two primary factors crucial for blending, the shape and size of the plastic region as well as the velocity profile. The shape and size of the plastic region serves a fundamental purpose in the blending process as it governs the quantity of material that is to be blended. With higher cohesion values there is an increase in the area of the plastic region permitting a greater number of particles into the region resulting in quicker blend times. These quicker blend times are reflected in the variance graphs. The effects of cohesion upon the thickness of the plastic region was incorporated into the model through Sokolovskii's equation, however, the gradient of the velocity profile remained the same throughout. An exponential velocity profile was assumed with the maximum velocity occurring at the free surface and decaying to a minimum velocity at the elastic-plastic interface. The exponential decay coefficient k_1 was held constant for all runs of the simulations. Varying the k_1 coefficient alters the magnitude the gradient in which the particles travels pass one another. Despite not incorporating the freedom of k_1 to vary with cohesion we were able to accurately predict the appropriate blend times, indicating a greater significance being placed on accurate prediction of the size of the plastic region versus the velocity profile. Improvements could be

made into the model by allowing k_1 the flexibility to vary with cohesion. Although this will not significantly alter the blend times, which is the primary objective of the model, it will allow for a better correlation with experimental data for the initial stages of blender at all cohesion levels.

Results from the method of characteristic model were comparable with those of the parabolic model in almost every aspect. Similarities between the two models were foreseeable upon review of the plastic region generated by the method of characteristic model. Other than a slight flattening of the base of the plastic region for the method of characteristic model the regions were nearly identical in both size and shape. From the parabolic model we learned that the size and shape of the plastic region is of greater significance in the blending process than the actual velocity profile. Since the plastic region of the method of characteristic model did not differ greatly from the parabolic model we did not anticipate the results to either, despite having a distinct velocity profile. As with the parabolic model the method of characteristic model predicts progressively improved blending with greater and greater cohesion. Lacking the cascading mechanism the reverse blending trend observed experimentally at higher cohesion values is beyond the current capability of this model as well. Incorporating the cascading phenomenon into the model will inhibit the blending process, setting the course of blending in the correct direction by at moments throughout the blending process temporarily stopping the continuous flow of the plastic region and simultaneously restrict the easy at which the particles flow. Although not capable of predicting the blend times for the highest cohesion value, accurate blend times for the lowest and intermediate cohesions values were achieved. Similar to the parabolic model, discrepancy exist for the initial stages for the lowest cohesion values in which the predicted variance deviates from the experiments. Once again this discrepancy is attributed to the velocity gradient. The method of characteristic naturally varies the velocity

gradient within the plastic region depending on the size of the region, however, this change is minuscule. It was determined that the velocity gradient that is projected into the plastic region is heavily dependent upon the velocity assigned along the free surface. A maximum velocity was assigned to the uppermost section of the free surface and gradually decreased to a velocity of zero at the bottom of the pile. The rate of this decrease was the same for all simulation at all cohesion values. The rate of this decrease functions in a similar fashion as the k_1 coefficient of the parabolic model. Selecting a rate that would be appropriate for the lower cohesion values should allow for greater accuracy in the variance graphs.

Over the years a number of models have emerged to predict blending. Each model provided its own unique take on the blending process and offered new insight that preceding models have not; however, although these models are distinct from one another they each fall into one of two primary categories. Some address the blending issue from a macroscopic point of view in which continuity equations are used to describe the blending phenomenon, while other tend to confront the issue from a microscopic point of view using the forces imposed on individual particles to describe the blending tendency of the bulk. Within these two primary categories used in the modeling of blenders, segregation is a subcategory that exists in each. The distribution of particles of similar mechanical properties only accounts for a portion of blending there is a vast number of mixtures that consists of components of varying mechanical properties. Whether these variations are due to differences in size, shape, density, etc. segregation is the inevitable result. Both methods continuous and discrete although distinct are striving to arrive at the same conclusions. They each have their advantages and disadvantages. The advantages of the discrete method of modeling that attracted Nase and McCarthy along with many others are the comprehensive understanding of the workings of the inter-particle interactions along with the

easy of which particle boundary interactions can be implemented. The disadvantages, however, are that these inter-particles interactions which are being utilized are for smooth, perfectly spherical particles and only a hand full of particles can be implemented in simulations. Currently the computation capabilities of computers do not permit a realistic number of particles to be employed using a discrete approach. Continuous models center on the understanding of the flow of granular material, although not as comprehensive as our knowledge of inter-particle forces it can be applied to particles of irregular non-spherical shapes. Interactions with the boundary for continuous models are more difficult and cumbersome, however, if the boundary are well defined a continual approach can provide a realistic description of the overall flow behavior of the bulk where as the discrete models are limited to a few thousand particle and therefore incapable of accurately describing the flow behavior for reasonable sized blenders.

Blending is a convoluted process that involves material properties, blender geometry and operational parameters. An accurate model must include all three. The difficult that ensues with doing this discretely is why we choose to use a continuous model. In a discrete model the entire gamut of parameters whether it be a material property or a blender operational or geometric parameter are interlinked. The flow ability of the material is not only affected by the cohesion of the material caused by material parameters such as particle size and surface roughness, but also dependent upon blender parameters such as the fill height and rotational speed via contact mechanical forces through particle-particle collisions and particle-boundary collisions. Although feasible a valid discrete approach requires the inclusion of all the blender parameters and individual forces. Our continuous model does not require specific details of the inter-workings which are responsible for the attractive forces of the particles. Whether the attractive forces are initiated by Van der Waals forces, surface roughness or liquid bridges is relevant. The individual

material properties and forces responsible for the attractive force the particle have for one another are linked together through two measurable properties cohesion and the internal angle of friction. The incorporation of material properties through the cohesion and internal angle of friction is what separates our continuous model from continuous models of others. Others have incorporated similar parabolic shapes for the plastic region, but have failed to tie in the importance of cohesion in the development of its size which is a pivotal factor in the blending process. In addition to incorporating cohesion into our model our model has the means of determining the uniformity of mixture throughout the blending process and determining the appropriate blend times for cohesion values below that of a critical value. The continuous models proposed by Ottino and Khakhar along with others do not provide a means of predicting blend uniformity of the mixture based on knowledge of flow properties, they visually compare the uniformity of their simulation with those of experiments and for cases in which particles of varying size were used they compared pattern formations that developed.

Two continuous models were proposed both of which are capable of accurately predicting blend times for cohesive values lower than that of the critical values for particles of the same mechanical properties in which segregation is not a concern. Although, not currently incorporated into the model, a cascading mechanism was observed at higher cohesion values that when included into the model will allow for accurate predictions of the blend times at higher cohesion values.

LIST OF REFERENCES

- [1] D.V. Kwacha, Ashish V. Orpe, J. M. Ottino, Continuum model of mixing and size segregation in a rotating cylinder: concentration-flow coupling and streak formation, *Powder Technology* 116 (2001) 232-245
- [2] G. Metcalfe, T. Shinbrot, J. J. McCarthy, J. M. Ottino, Avalanche mixing of granular solids, *Nature* 374 (1995) 39-41
- [3] S. T. Nase, W. L. Vargas, A. A. Abatan, J.J. McCarthy, Discrete characterization tools for cohesive granular material, *Powder Technology* 116 (2001) 214-223
- [4] J. J. McCarthy, Micro-modeling of cohesive mixing processes, *Powder Technology* 138 (2003) 63-67
- [5] P. V. Danckwerts, Continuous flow system Distribution of Residence Times, *Chemical Engineering Science GENIE CHIMIQUE* 2 (1953)
- [6] Sokolovskii, V.V. (1965). *Statics of Granular Media*. New York: Pergamon
- [7] Duncan, J. M. & Wright, S. G. (2005). *Soil Strength and slope Stability* Hoboken, N.J.: John Wiley & Sons
- [8] David F. McCarthy, *Essentials of Soil Mechanics and Foundations Basic Geotechnics*
- [10] Alexandrou, A. N. (2001). *Principal of Fluid Mechanics* Upper Saddle River, N.J.: Prentice Hall
- [11] K. Rietema, Powders, What are they?, *Powder Technology* 37 (1984) 5-23
- [12] Davis, R.O, Selvadurni A.P.S., (2002). *Plasticity and Geomechanics*. Cambridge, Cambridge university Press
- [13] *Introduction to the Mechanics of a Continuous Medium* Lawrence E. Malvern
- [14] Nedderman, R. M. (1992). *Static and Kinematics of Granular Material*. Cambridge, Cambridge university Press
- [15] Gray, J. M. N. T., Granular Flow in Partially Filled Slowly Rotating Drums, *Journal of Fluid Mechanics*, vol. 441, pp. 1-29 2001
- [16] Elperin, T. and Vikhansky, A., Granular Flow in a Rotating Cylindrical Drum, *EurophysicsLetters*, 42 (6), pp. 619-623 1998
- [17] Metcalfe, G., Graham, L., Zhou, J. and Liffman, K., Measurement of Particle Motions within Tumbling Granular Flows, *Chaos*, vol. 9 (3), pp. 581-593 1999

- [18] Shinbrot, T., Alexander, A., Moakher, M. and Muzzio, F., Chaotic Granular Mixing, *Chaos*, vol. 9 (3), pp. 611-620 1999
- [19] Moakher, M., Shinbrot, T. and Muzzio, F., Experimentally Validated Computations of Flow, Mixing and Segregation of Non-Cohesive Grains in 3D Tumbling Blenders, *Powder Technology* 109, pp. 58-71 2000
- [20] McCarthy, J., Khakhar, D. and Ottino J., Computational Studies of Granular Mixing, *Powder Technology*, 109, pp. 72-82 2000
- [21] Chapra, S.C. (1988). *Numerical methods for engineers* New York: McGraw-Hill
- [22] Sharrna, P., Brown, S., Walter, G., Santra, S., & Moudgil, B. Nanoparticles for bioimaging. *Adv Colloid Interf Sci* **123**, 471-485 (2006)
- [25] Sigmund, W. & El-Shall H. (2009). *Particulate Systems in Nano- and Biotechnologies* Boca Raton, FL CRC Press
- [26] R.M. Horne, R.M. Nedderman, Stress Distribution in Hoppers, *Powder Technology* 19 (1978) 234-254
- [27] R.M. Horne, R.M. Nedderman, Analysis of the Stress Distribution in Two-Dimensional Bins by the Method of Characteristics, *Powder Technology* 14 (1976) 93-102
- [28] R.M. Horne, R.M. Nedderman, An Analysis of Switch Stresses in Two-Dimensional Bunkers, *Powder Technology* 19 (1978) 235-241
- [29] E.B. Nauman, Residence Time Distribution in Systems Governed by the Dispersion Equation, *Chemical Engineering Science* 36 (1981) 957-966
- [30] T. Shinbrot, A. Alexander, F.J. Muzzio, Spontaneous Chaotic Granular Mixing, *Nature* 397 (1999) 675-678
- [31] A.E. Scheidegger, On the Prediction of the Reach and Velocity of Catastrophic Landslides, *Rock Mechanics* 5 (1973) 231-236
- [32] Weinekötter, R., Gericke H. (2000). *Mixing of Solid*. Netherlands: Kluwer Academic Publishers
- [33] Klose W., Schinkel A., Energy and Mass Transport Processes in The Granular Bed of an Indirectly Heated Rotary Kiln, *China Particuology* 2 (2004) 107-112
- [34] Khakhar D. V., McCarthy J. J., Gilchrist J. F., Ottino J. M., Chaotic Mixing of Granular Materials in Two-Dimensional Tumbling Mixers, *American Institute of Physics* 9 (1998) 195-205

- [35] Khakhar D. V., McCarthy J. J., Shinbrot T., Ottino J. M., Transverse Flow and Mixing of Granular Materials in a Rotating Cylinder, *Phys. Fluids* 9 (1997) 31-43
- [36] Bridgwater J., Fundamental Powder Mixing Mechanisms, *Powder Technology* 15 (1976) 215-231
- [37] Muzzio F.J., Robinson P., Wightman C., Brone D., Sampling Practices in Powder Blending, *Int. J. Pharm.* 155 (1997) 153-178

BIOGRAPHICAL SKETCH

I attended the University of Illinois at Chicago (UIC) where I received my bachelor degree in chemical engineering in May 2001. Right after completing my degree at UIC I moved to Gainesville Florida where I continued my education in chemical engineering at the University of Florida. Once accepted into the PhD program I began my studies of bulk solids specializing in the blending aspect of powder flow.